A STUDY OF GALACTIC OUTFLOWS

by

Mahavir Sharma

A Thesis submitted to the

Jawaharlal Nehru University, New Delhi

for the degree of

Doctor of Philosophy

Raman Research Institute
Bangalore 560080
INDIA

2013

Certificate

This is to certify that the thesis entitled ‘A Study of Galactic Outflows’ submitted by Mahavir Sharma for the award of the degree of Doctor of Philosophy of Jawaharlal Nehru University is his original work. This has not been published or submitted to any other University for any other Degree or Diploma.

Prof. Ravi Subrahmanyan	**Prof. Biman B. Nath**
Director	Thesis Supervisor

Raman Research Institute,
Bangalore 560 080
INDIA

Declaration of Authorship

I, Mahavir Sharma, declare that the work reported in this thesis titled ‘A Study of Galactic Outflows’, is entirely original. This thesis is composed independently by me at the Raman Research Institute under the supervision of Prof. Biman B. Nath. I further declare that the subject matter presented in this thesis has not previously formed the basis for the award of any degree, diploma, membership, associateship, fellowship or any other similar title of any university or institution.

Prof. Biman B. Nath **Mahavir Sharma**

Astronomy and Astrophysics Group,
Raman Research Institute,
Bangalore 560 080
INDIA

Acknowledgements

It has been quite an experience in past few years, and here I am at the first stage of my journey into the field of scientific research. I am grateful to my supervisor Biman for his advice and support and it has been a leisurely and immensely educative experience to work with him. I thank Yuri Shchekinov for his insightful comments at various stages of the work. I thank Indranil Chattopadhyay for introducing me to the numerical simulations, and Hum Chand for teaching me the basics of absorption lines in quasar spectra. I enjoyed working with Max Uhlig and Christoph Pfrommer on cosmic ray streaming and I thank them for fruitful discussions. I thank Torsten Ensslin for discussions on cosmic rays and insightful comments on my work. I am grateful to the scientific and administrative staff at RRI for their help in all the academic and non-academic matters.

I am grateful to our director Ravi for his advice during initial days at RRI. I am grateful to our group secretary Vidya for her disciplined conduct of formalities, and for guiding me through the office matters. I thank Radha and Marisa in main building for their excellent conduct of the administrative work. I thank the library staff at RRI for maintaining all the important books and journals, as well as a state of the art search engine. I thank all the academic staff on the Astro-floor for being an experienced critic during various occasions when I was presenting my work.

I thank all my friends here at RRI whose company I have enjoyed through discussions, sports, movies or travels in past few years. I enjoyed the company of my batch-mates Jagdish, Chaitra, Anjon, Jyothi, Prasad and Samim during first year when I was in RMV hostel and specially Arnab who created my interest in the sport of Tennis, when we were watching 2009 US open final. Nishant has been a friend with absolute clarity in views; Naveen, a source of spiritual and recreational energy; and Jagdish, an interesting person with simple ideas. I enjoyed discussions with Yogesh, Harsha, Wasim, Mamta, Madhukar, Santosh and Kanhaiya at various occasions. I thank my friend Chaitra for lively discussions and his advice during first year. I thoroughly enjoyed playing Cricket, Volley-ball, Table-tennis and Badminton with people in RRI and I thank them all for creating the necessary extra-curricular environment.

Finally, I am grateful to my parents, for their immense support and encouragement in pursuit of my interests. My family has always been with me in whatever choice I have made and I hope to live up to their expectations in the future.

Synopsis

Galactic outflows are multiphase hydrodynamic phenomena observed in various wavelengths, and are thought to be driven by supernovae (SNe), radiation pressure and AGN activity. They are important as a feedback process for galaxy evolution, as they are believed to shape the galaxy luminosity function, enrich the intergalactic medium (IGM) with metals and drive the universal mass-metallicity relation in galaxies. These large scale outflows are observed in X-rays, Hα, in the neutral lines such as Na D and Mg II , as well as in molecular lines e.g. CO and H_2. In this thesis, we study the outflows analytically and using simulations. We obtain interesting results which explain a variety of observations such as (I) the correlation between the outflow speed and the galaxy circular speed, (II) the relative importance of ram and radiation pressure and the importance of cosmic rays (III) observed threshold of star formation surface density ($\Sigma_{\rm SFR} \sim 0.1$ M$_\odot$ yr^{-1} kpc^{-2}), for galaxies to show signatures of outflows, (IV) high velocity ($> 10^3$ km s^{-1}) outflows due to the presence of an AGN, (V) gas reservoirs in the halos of galaxies (VI) ratio of the stellar to halo masses in galaxies. We also carry out an observational study in which we search for a correlation between the quasar luminosity and the velocity offset of strong Mg II absorbers in quasar spectra, and explore the possibility that a significant fraction of strong Mg II absorbers may arise in outflows driven by quasar radiation. We describe below the work conceived in this thesis and our findings.

Radiation driven outflows from disc galaxy

Observational studies of cold phase outflows ($T \sim 10^4$ K) show that the maximum speed of outflowing gas is correlated with the circular speed of the galaxy (Martin, 2005). Similar correlations, when used in simulations of galaxy formation as a feedback recipe, can explain the galaxy luminosity function as well as the enrichment of IGM (Oppenheimer & Davé, 2006). Such a correlation between the wind speed and circular speed is better explained by radiation driving as compared to the standard SNe driving (Martin, 2005; Murray et al., 2005). We study gaseous outflows along the pole of a galaxy, driven by radiation pressure on dust grains. We consider the gravitational and radiation forces due to a disc with surface brightness (I) and surface mass density (Σ). We also include the gravitational effect of bulge and dark matter halo and show that the existence of such an outflow implies a maximum value of $\sim 10^{-2}$ for disc mass-to-light ratio. We show that the terminal wind speed is proportional to the disc rotation speed in the limit of a cold gaseous outflow. Using the mean opacity of dust grains and the evolution of the luminosity of a simple stellar population, we then show that the ratio of the wind terminal speed (v_∞) to the galaxy rotation speed (v_c) is roughly

$v_\infty/v_c \sim 3$. We find that these outflows can be sustained for a period of ~ 10 Myr after a burst of star formation, and further evolution of these winds depends on the rate of occurrence of starbursts.

Furthermore, we carry out a 2-D hydrodynamic simulation of radiation driven galactic wind from a disc with exponentially varying surface brightness and mass density, and total mass of the galaxy similar to that of the Milky Way. We use the TVD hydrodynamic code developed by Ryu et al. (1993); Kang et al. (1994). We simulate in cylindrical coordinates and study the structure and dynamics of cool and/or warm ($T \simeq 10^4$ K) outflows. We have taken into account the total gravity of a galactic system that consists of a disc, a bulge and a dark matter halo. We find that the combined effect of gravity and radiation pressure from a realistic disc drives the gas away to a distance of ~ 5 kpc in ~ 37 Myr for typical galactic parameters. The outflow speed increases rapidly with the disc Eddington parameter $\Gamma_0(= \kappa I/(2cG\Sigma))$ for $\Gamma_0 \geq 1.5$. We find that the rotation speed of the outflowing gas is $\lesssim 100$ km s^{-1}. The wind is confined in a cone which mostly consists of low angular momentum gas lifted from the central region.

Outflows driven by combined action of radiation and ram pressure

In the standard SNe/starburst driven wind scenario, the cold clouds are thought to be entrained in the hot phase of flow via ram pressure (e.g. Heckman et al., 2000). However, recent models based on radiation pressure neglect the ram pressure as a driving mechanism. If one carefully compares the ram pressure driving and radiation pressure driving, both mechanisms have limitations. In the case of ram pressure, although the hot gas provides the momentum to cold clouds, it can also disrupt the clouds via shocks and instabilities and, as a result, the clouds may not survive long enough (e.g. Marcolini et al., 2005), which is quite contrary to observations in which the cold clumps are seen upto heights of ~ 10 kpc. On the other hand, in case of radiation driving, as we mentioned above, the luminosities required are quite large, which may be available only for short periods (~ 10 Myr). In the face of two processes (ram pressure and radiation pressure) leading to outflows, one wonders if both processes contribute equally, or if there are regimes in which one of these two processes dominate over the other.

To explore these issues, we study gaseous clumpy outflows from disc galaxies driven by the combined effects of ram pressure and radiation pressure. Taking into account the gravity due to disc, bulge and dark matter halo, and assuming continuous star formation in the disc, we show that radiation or ram pressure alone is not sufficient to drive escaping outflows, and both processes contribute. We show that, in the parameter space of SFR and circular speed

(v_c) of galaxies, the criteria for the outflows can be written as, $\mathrm{SFR}^{3/4}_{10\ \mathrm{M}_\odot/\mathrm{yr}}\, v^{-2}_{c,140\ \mathrm{km/s}} > 1$. We find that the above criteria implies that the winds should occur in galaxies with star formation surface density roughly $\Sigma_{\mathrm{SFR}} \gtrsim 10^{-1}$ $\mathrm{M}_\odot$ yr^{-1} kpc^{-2}, and thus explains the observational threshold for winds. We note that the wind speed in galaxies with rotation speed $v_c \leq 200\,\mathrm{km\,s^{-1}}$ and SFR ≤ 100 $\mathrm{M}_\odot$ yr^{-1}, has a larger contribution from ram pressure, and that in high mass galaxies with large SFR, radiation from the disc has a greater role in driving galactic winds. For galaxies satisfying our outflow criteria, the ratio of wind speed to circular speed can be approximated as, $v_w/v_c \sim 10^{0.7}\ \mathrm{SFR}^{0.4}_{50\,\mathrm{M}_\odot/\mathrm{yr}}\, v^{-1.25}_{c,120\,\mathrm{km/s}}$. This conclusion is borne out by observations of galactic winds at low and high redshift and also of the circumgalactic gas. We also estimate the mass loading factors under the combined effect of ram and radiation pressure, and show that the ratio of mass loss rate to SFR scales roughly as $v_c^{-1}\Sigma_g^{-1}$, where Σ_g is the gas column density in the disc.

Hydrodynamic study of SNe and AGN driven outflows

SNe driven winds are important for low mass galaxies and the inclusion of this process in galaxy formation models can account for observed stellar content of galaxies at low mass end. For high mass galaxies, it is believed that AGN feedback shapes the galaxy luminosity function. In semi-analytic modelling the SNe and AGN feedback are used as free parameters which are tuned to explain the observed galaxy properties (e.g. Baugh, 2006). The literature lacks an analytical treatment which quantifies the effect of gravity on SNe driven superwinds. Also recently, there have been observational indications that outflows with speeds greater than 1000 km/s in many Ultra Luminous Infra Red Galaxies (ULIRGs), are driven by AGN (Tremonti et al., 2007; Sturm et al., 2011).

To address these issues, we conduct a hydrodynamic study and work out the steady state analytical solutions for winds from galaxies with NFW dark matter halo. We consider winds driven by energy and mass injection from multiple supernovae (SNe), as well as momentum injection due to radiation from a central black hole. We find that the wind dynamics depends on three velocity scales: (a) $v_\star \sim (\dot{E}/2\dot{M})^{1/2}$ describes the effect of starburst activity, with $\dot{E}, \dot{M}$ as energy and mass injection rate in a central region of radius R; (b) $v_\bullet \sim (GM_\bullet/2R)^{1/2}$ for the effect of a central black hole of mass $M_\bullet$ on gas at distance R and (c) $v_s = (GM_h/2\mathcal{C}r_s)^{1/2}$ which is closely related to the circular speed (v_c) for NFW halo, with r_s as the halo scale radius and $\mathcal{C}$ is a function of halo concentration parameter. Our generalized formalism, in which we treat both energy and momentum injection from starbursts and radiation from AGN, allows us to estimate the wind terminal speed as, $v_\infty = (4v_\star^2 + 6(\Gamma - 1)v_\bullet^2 - 4v_s^2)^{1/2}$, where Γ is the ratio of force due to radiation pressure to gravity of the central black hole. Our dynamical model also predicts the following: (a) winds from quiescent star forming galaxies cannot escape from $10^{11.5} \le M_h \le 10^{12.5}$ M$_\odot$ galaxies, (b) circumgalactic gas at large distances from galaxies should be present for galaxies in this mass range, (c) for an escaping wind, the wind speed in low to intermediate mass galaxies is ~ 400–1000 km/s, consistent with observed X-ray temperatures; (d) winds from massive galaxies with AGN at Eddington limit have speeds $\gtrsim 1000$ km/s. We also determine the stellar to halo mass ratio of galaxies, following the scheme suggested in Granato et al. (2004). In this scenario, the ratio $[2v_\star^2 - (1-\Gamma)v_\bullet^2]/v_c^2$ dictates the amount of gas lost through winds. Used in conjunction with an appropriate relation between $M_\bullet$ and M_h, and an appropriate opacity of dust grains in infrared (K band), this ratio has the attractive property of being minimum at a certain halo mass scale ($M_h \sim 10^{12-12.5}$ M$_\odot$) that signifies the cross-over of AGN domination in outflow properties from starburst activity at lower masses. We find that stellar mass for massive galaxies scales as $M_\star \propto M_h^{0.26}$, and for low mass galaxies, $M_\star \propto M_h^{5/3}$.

Signatures of outflows in strong Mg II absorbers in quasar sightlines.

We have carried out an observational study to explore the possibility that Mg II absorbers in quasar sightlines are associated with quasar radiation driven outflows. For this we consider the quasar spectra in SDSS Data Release-7. We divide the data in the bins of luminosity of quasars and study the correlation between velocity offset ($\beta = v/c$) of strong (equivalent width > 1 Å) Mg II absorption systems and the bolometric luminosity ($L_{\rm bol}$) of quasars in SDSS-DR7. We find that β shows a power law increase with $L_{\rm bol}$, with a slope of 1/4, and such a scaling of β with $L_{\rm bol}$ is expected for outflows driven by scattering of black hole radiation by dust grains, launched from the innermost dust survival radius. Our results indicate that a significant fraction of the strong Mg II absorbers, in the range of $\beta = 0.0$–0.4 may be associated with the quasars themselves.

List of Figures

List of Tables

Contents

Chapter 1

Introduction

In the standard cosmological model, where galaxies are the building blocks of the Universe, galactic outflows play a significant role in shaping the properties of galaxies. They control the star formation rate (SFR) and metal content in galaxies and enrich the intergalactic medium (IGM) with metals. The word feedback has a general meaning which describes a loop in which the outcome of a process influences the inputs as well. Galactic outflows indeed act as a feedback process for galactic systems, because they remove gas and metals and quench the star formation, which is required at the first place for driving the outflows. Research on the galactic outflows span the last five decades and it is one of the important baryonic processes which holds the key for a better understanding of galaxy evolution.

Galactic Outflows or *Galactic Winds*[*] span length-scales from a few to hundred kpc and originate from the disc or centre of galaxies. There are many different phenomenon which fall under the category of galactic outflows e.g. galactic fountain (with gas falling back on the disc of the galaxy), galactic supershells which have a compressed layer of gas, and galactic freewind or superwind, which is a steady and smooth flow of gas. In this chapter we introduce the field of outflows and provide a literature and technical review. We discuss outflow observations, theoretical models, and physics of driving outflows. This introductory chapter is organised as follows.

In §1.1 of this chapter, we give a general description of galactic winds and discuss a few early theoretical studies. In §1.2 we discuss the importance of outflows for galaxy formation, IGM enrichment and for maintaining mass-metallicity relation in galaxies. In §1.3 we survey the observational studies on outflows and introduce some milestone observational results. Among them we also discuss the classification of phases of the outflows. In §1.4, we discuss different mechanisms for driving outflows such as, the driving due to starburst or supernovae

---

[*] Throughout this thesis we use the words *wind* and *outflow* interchangeably to address the same phenomenon.

(SNe), due to radiation pressure on dust grains, due to the cosmic rays and the driving due to an active galactic nucleus (AGN). In §1.5, we discuss the absorption lines in quasar spectrum and their origin. In §1.6, we discuss the motivations for this study and in §1.7 we describe the structure of this thesis.

1.1 Early theoretical studies

The possibility that galaxies can harbour large scale winds was explored soon after the models of solar wind (e.g. Burke, 1968). It was further proposed that galactic winds may cause elliptical galaxies to lose all of their gas (Johnson & Axford, 1971; Mathews & Baker, 1971). These early models were hydrodynamical and were inspired by the trans-sonic solar wind model developed by Parker (1965). To elaborate, in these studies, galactic outflows are modelled using a set of fluid equations, representing mass, momentum and energy conservation, which are written in density (ρ), velocity (v) and temperature (T) variables. The $\rho, v, \text{ and } T$ are averaged over a fluid control volume or fluid element. These equations can be applied if the so called *fluid approximation* holds, i.e. if the mean free path of particles in a system is less than the size of the system. In Table 1.1, we have compared the ratio of mean free path to system size for various astrophysical situations. One can see that fluid approximation holds good for galactic outflows.

System	Size (L)	n (cm^{-3})	T (K)	$\lambda_{\rm mfp}$ (cm)	$\lambda_{\rm mfp}/L$
Centre of the Sun	$R_\odot$	10^{26}	10^7	2×10^{-8}	$\sim 10^{-19}$
ISM cloud	100 pc	1	10^4	9×10^{11}	$\sim 10^{-9}$
Galaxy Cluster	Mpc	10^{-3}	3×10^7	5×10^{21}	$\sim 10^{-3}$
Solar Wind	AU	5	10^6	2×10^{15}	$\sim 10^{2}$
Galactic Wind	10 kpc	10^{-2}	10^6	6×10^{17}	$\sim 10^{-5}$

Table 1.1: Mean free paths for various astrophysical systems are compared with the systems size. Mean free paths are calculated by using the relation $\lambda_{\rm mfp} \approx 2\times10^5\left(\frac{T^2}{n\ \ln\Lambda}\right)$ cm, based on the Coulomb collisions (Spitzer, 1962), where T is the temperature, n is the density and '$\ln\Lambda$' is the Gaunt factor.

The review by Holzer & Axford (1970) gives an elaborate account of the theoretical aspects of solar and galactic winds. In general an adiabatic flow can not have a critical point. Continuous energy injection is required in order to have a trans-sonic outflow. In galaxies the SNe and starbursts are the sources for energy and mass injection. Strength of the energy injection scales with the SFR and hence it is generally more in starburst galaxies.

A milestone work was done by Chevalier & Clegg (1985) in this regard. These authors proposed a model for the superwind in the starburst galaxy M82. They showed that energy injection in the central region can drive a high velocity outflow ($\sim 1000\ \mathrm{km\ s^{-1}}$), which passes through a sonic (critical) point. In this work the gravity of the galaxy was not considered, because the velocity of the wind was an order of magnitude higher then the escape velocity of the galaxy. Wang (1995) modelled the wind from a power-law gravitational potential and showed that the wind may escape the galaxy or settle in a galactic corona depending on the mass of the galaxy. Wang (1995) also determined the mass of galaxies from which winds can escape and in which galaxies they will be confined, thereby giving rise to reservoirs of gas in halos. Apart from these large scale winds arising from the nuclear regions of galaxies as envisaged in the above mentioned works, there have been models exploring the winds from individual star clusters. Silich et al. (2011) worked out the free wind dynamics from super star clusters with exponential stellar density distribution and, also studied the effects of cooling on these winds.

1.2 Importance of outflows

1.2.1 As a feedback process in galactic evolution

Galaxies are the building blocks of Universe. A large fraction of the matter in galaxies and, in general $\sim 80\%$ of the matter in our Universe, is in a state which we can not see directly and it is known as the dark matter. Thus one studies the formation of structures by the hypothetical dark matter. The state of the art N-body simulations track the evolution of perturbations as a function of redshift in an expanding Universe. The perturbations initially grow linearly but later turn nonlinear. At a stage when the overdensity is $\delta \approx 1.686$, the high density regions collapse and form viriallized dark matter halos with a range of masses. One can catalogue the halos and then derive the mass function for these halos. The analytical methodology devised by Press & Schechter (1974) and later extended by Sheth & Tormen (2002), also yield the same mass function and agree with the N-body simulations. The halo mass function generally has a power law form and an exponential tail and it is generally termed as a Press-Schechter halo mass function. The mass function serves as an interesting prediction of the cold dark matter scenario of the structure formation in Universe. In the left panel of Figure 1.1, we have shown a plot of the halo mass function (figure taken from Somerville & Primack 1999) . Various lines correspond to the theoretical models differing in the choice of cosmological parameters, with the prediction of ΛCDM shown by a long dashed line.

The next step is to compare this theoretically derived mass function with the observed one. In practice we observe the luminosity function for galaxies rather than the mass function. To convert the luminosity function to the mass function, we can assume a constant luminosity to baryonic mass ratio. Another step would then be to translate the baryonic mass obtained form luminosity to the dark matter mass. To achieve this, we may assume that all the dark matter halos contain a universal fraction ($\approx 1/6$) of baryons. Therefore, by using, $L \propto M_\star = M_h/6$ we arrive at the 'observed galaxy mass function', shown by dash-dotted line in left panel of Figure 1.1. The curves clearly show that there is some problem with this simple picture. Although the shape of the mass function can still be represented by a Press-Schechter form with power law and exponential tail, however, the slopes are not the same. The observed mass function is flatter and steeper at lower and higher mass ends respectively. Hence the theoretical models seem to over-predict the number of halos both at the lower and the higher mass end.

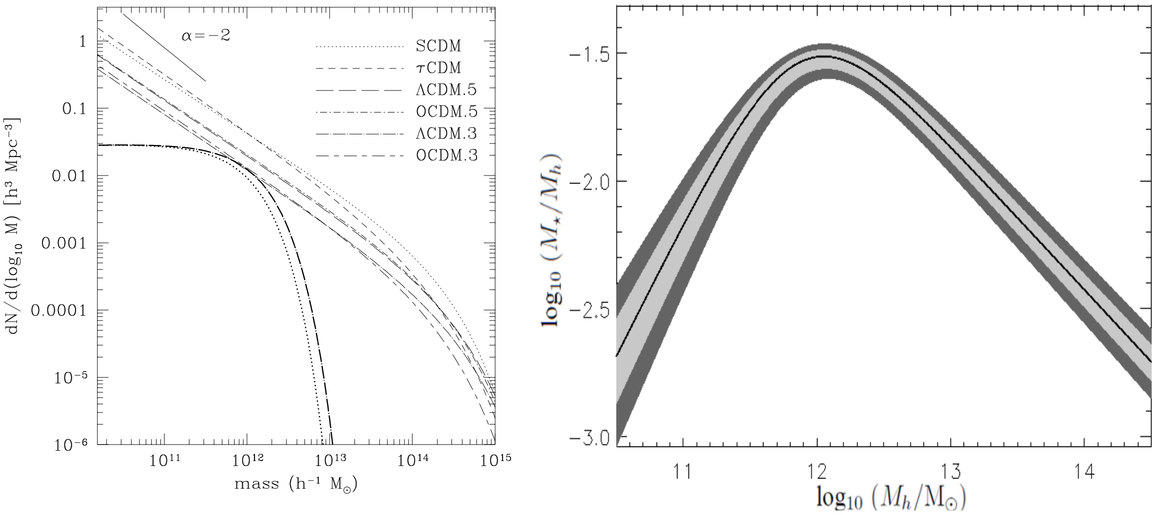

Figure 1.1: In left panel the halo mass function from cold dark matter theories is compared with the one obtained from the observed galaxy luminosity (figure is taken from Somerville & Primack 1999). In the right panel, the stellar to halo mass ratio is shown as a function of the halo mass (M_h), taken from Moster et al. (2010). The solid line is the best fit stellar to halo mass relation. The light and dark shaded regions extend upto the 1σ and 2σ uncertainty.

Recent authors have expressed this problem in a different way. If we drop the assumption that $M_\star \propto M_h$, then we can consider $M_\star = f(M_h)$, where $f(M_h)$ is a function of the halo mass whose form is chosen in such a way that the observed mass function matches with the theoretical one. The task is then to find a suitable $f(M_h)$ which is achieved by using the condition $n(< M_\star) = n(< M_h)$, where $n(< M)$ represent the cumulative number of halos upto a particular mass M. Using this technique of 'halo abundance matching', one can derive the shape of the stellar to halo mass function ($M_\star = f(M_h)$). We show this in the right panel of the Figure 1.1 from a recent study by Moster et al. (2010). One can see the peculiar shape of the ratio $M_\star/M_h$, which has a positive and negative slope with a peak roughly at

$M_h \sim 10^{12}$ $M_\odot$. From this figure we find that both the low and high mass galaxies do a poor job in maintaining a cosmological baryon fraction of $\approx 1/6$. Even the intermediate mass galaxies can not maintain this fraction, although they are the ones which show a maximum value of stellar mass to halo mass.

To reconcile with the problem of mismatch between the halo mass function and galaxy luminosity function, or in other words to explain the shape of the stellar to halo mass function (right panel of Fig. 1.1), it has been proposed that starbursts and SNe provide energy injection and cause large amount of mass to flow out of the galaxy as galactic superwinds (Larson, 1974; Dekel & Silk, 1986; Oppenheimer & Davé, 2006). Star formation is suppressed as the galaxies lose a significant portion of their baryons due to this negative feedback. Although this picture can provide an explanation for the low ratios of $M_\star/M_h$ for the low mass halos, for the high mass halos, gravity becomes strong and SNe are not sufficient to drive out the gas. In order to resolve the discrepancy at high mass end, it has been argued that AGN outflows may sweep away baryons and suppress the star formation in high mass galaxies (Silk & Rees, 1998; Wyithe & Loeb, 2003; Di Matteo et al., 2005; Springel et al., 2005; Croton et al., 2006; Bower et al., 2006). These two feedback processes, when considered together, are believed to explain the shape of galaxy stellar mass function at both low and high mass end (Binney, 2004; Cattaneo et al., 2006; Puchwein & Springel, 2013).

1.2.2 Enriching the IGM with metals

After the formation of galaxies, if there is no interaction between the galaxies and IGM, then the IGM should mostly consist primordial zero metallicity gas. However, an interesting finding is the detection of metal lines in the spectra of the high-z quasars (e.g. Songaila & Cowie, 1996; Cowie & Songaila, 1998; Songaila, 2001; Schaye et al., 2003). To be more specific, the low density IGM is partially enriched at all redshift as shown by the studies of Lyα forest; as suggested by lines such as C III , C IV , Si IV , O VI and so on. These results indicate that baryonic processes in the galaxies were responsible for transporting metals to such large distances. It has been suggested that galactic outflows resulting from the star formation process can drive metals into the IGM (e.g. Nath & Trentham, 1997; Ferrara et al., 2000). There are generally two approaches to address the problem of IGM enrichment. First one uses semi-analytic models, in which the effect of feedback from halos is studied using simple prescriptions, where the distribution of halos is obtained by using the Press-Schechter formalism (Aguirre et al., 2001; Madau et al., 2001; Bianchi & Ferrara, 2005; Bertone et al., 2005). The second approach uses large hydro and N-body simulations including complex baryonic processes, in which the galaxies and IGM are evolved with redshift (e.g. Cen &

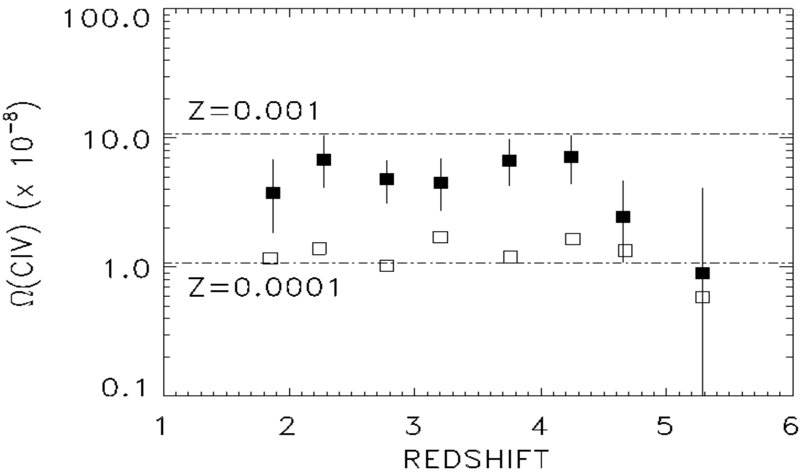

Figure 1.2: Metallicity of intergalactic medium as a function of redshift (figure taken from Songaila 2001).

Ostriker, 1999; Cen et al., 2005). In the aforementioned works the outflows which enrich the IGM are generally driven by the SNe explosions. Recently, using the smooth particle hydrodynamics (SPH) code GADGET, Oppenheimer & Davé (2006) considered the effect of radiation driven outflows and derived the metallicity of IGM at various redshifts. We would like to mention here that all these theoretical models can reproduce the values of observed metallicity in the IGM within an order of magnitude, which implies that some sort of outflows were indeed at work for redshift relevant for IGM enrichment.

This leads us to yet another interesting fact, which is the dependence of IGM metallicity on redshift, which tells us the epoch when the outflows were prevalent. In Figure 1.2, we have shown the metallicity of the IGM as a function of redshift from Songaila (2001). The metallicity of the IGM is $Z \sim 10^{-4}$–10^{-3} and it remains constant with redshift in the range, $z \sim 2$–5. This result indicates that the enrichment of the IGM was completed fairly early at high redshifts ($z > 5$) and for $z < 5$ the outflows have had little or no effect in altering the properties of IGM. Furthermore, it implies that the outflows at high redshifts should have been more prevalent and vigorous. This interesting prediction has now been verified with observations as well, where the fraction of galaxies showing outflows is found to be higher at high redshifts (Adelberger et al., 2003).

1.2.3 Mass-Metallicity relation in galaxies

McClure & van den Bergh (1968) reported a correlation between the luminosity and metallicity in elliptical galaxies. A decade later, Lequeux et al. (1979) reported a correlation between the mass and the metallicity in a sample consisting of irregular and blue compact galaxies. Tremonti et al. (2004) studied more than 50000 galaxies in SDSS for these correlations and found that the scatter in mass-metallicity relation is much lower than the luminosity-metallicity correlation thereby showing the importance of a mass-metallicity relation for galaxies. This fundamental relation have been extended by Lee et al. (2006) to include low mass systems thus making it valid for the entire mass range of galaxies. If galaxies are considered to evolve as closed boxes and keep forming stars continuously then the metallicity will keep on increasing indefinitely. Galactic outflows are thought to be the mechanism which can remove metals from galaxies and hence give rise to the observed Mass-Metallicity relation (e.g. Arimoto & Yoshii, 1987; Lehnert & Heckman, 1996; Garnett, 2002). Another explanation is via the continuous inflow of metal poor gas in the centre of galaxy (e.g. Finlator & Dave 2006) which continuously dilutes the metals and acts against the increase in the metallicity caused by star formation.

In a recent study by Mannucci et al. (2010), it has been shown that the mass-metallicity relation is actually a manifestation of a more fundamental relation between the stellar mass , SFR and the metallicity of galaxies. This work shows that the metallicity of the galaxies decrease with SFR and the gradient increases with decreasing stellar mass of galaxies. Galaxies with the highest stellar mass have nearly no variation in metallicity with SFR. Further, Mannucci et al. (2010) suggest that the origin of this 'fundamental metallicity relation' should be thought of, as a result of the interplay between the star formation activity, infall of metal poor gas, and the feedback or outflow processes which eject the metals. Recently, Dayal et al. (2013) have provided an analytic explanation for the fundamental metallicity relation as a result of star formation, inflow and outflows.

1.3 Observations of outflows

1.3.1 Some milestone results

Till late 90's the phenomena of galactic winds remained mostly confined to theoretical studies. There were a few early observations in Hα, which reported explosions in the starburst galaxy M82 (Lynds & Sandage, 1963; Burbidge et al., 1964). Evidence for non-circular motions was also presented in the galaxy NGC 253 (Demoulin & Burbidge, 1970). The general observational picture for many years was that of outflows being simple explosions which can break-out of the plane of the galaxies. However, theoretical studies developed a picture of large scale outflows which are widespread in many galaxies and more ubiquitous at high redshift, which possibly have shaped the baryonic and stellar content in galaxies (e.g. Dekel & Silk, 1986).

Conclusive evidence for the prevalence of outflows came in a study by Heckman et al.

(1990). These authors presented the emission line studies of 14 Luminous Infra Red Galaxies (LIRGs). There were clear signatures of outflows in the double peaked emission lines, which originate when the cone of a bipolar outflow cut through the line of sight. This work supported a scenario in which outflows are driven by energy injection due to SNe in the nuclear starburst region (e.g. Larson, 1974; Chevalier & Clegg, 1985).

X-ray studies of the outflows were boosted by the launch of space telescopes. These observations brought out vertically extended diffuse gas visible in soft X-ray emission (see Figure 1.3, left panel). One cannot infer the velocity of the gas emitting X-rays directly. However one can use the temperature of the gas to estimate the velocity. The temperature of the X-ray emitting gas is found to be roughly ~ 0.1 keV in nearly all the galaxies having superwinds (Martin, 1999; Strickland et al., 2004). If we assume the X-ray emitting gas to be a steady outflow passing through a sonic point, then its velocity would be a few times the sound speed. Recent works consider a speed of roughly $400\text{–}600 \mathrm{~km~s^{-1}}$ for the X-ray emitting hot wind (Martin, 2005; Murray et al., 2005). Another interesting fact is the spatial correlation of soft X-ray emission with the $\mathrm{H}\alpha$ emission (Lehnert et al., 1999; Strickland et al., 2004). Recently, Cooper et al. (2009) compared various situations related to cloud–wind interaction in which the soft X-ray – $\mathrm{H}\alpha$ spatial correlation may arise.

Absorption lines provide yet another window to probe the galactic outflows. Heckman et al. (2000) studied the outflow from LIRGs and starburst galaxies using absorption lines in galaxy spectra. The basis for absorption line studies lie in the fact that for face on galaxies the light passes through the gas ejected perpendicular to the galactic plane, hence it gets blueshifted in the rest frame of the galaxy. The lines typical chosen for such studies are Na D and Mg II , which probe the neutral component of the galactic outflows. The advantage of absorption lines over X-ray studies is the accurate determination of the velocity of outflowing gas. In the study by Heckman et al. (2000), the velocity of outflows were typically in the range $400\text{–}700 \mathrm{~km~s^{-1}}$. However, no correlation was found between the outflow speed with the galaxy mass or the circular speed. Subsequent absorption line studies by various groups have explored many local and high redshift galaxies for outflows (Schwartz & Martin, 2004; Martin, 2005; Rupke et al., 2005b; Weiner et al., 2009; Kornei et al., 2012). These studies have yielded interesting correlations like the scaling of outflow speed with SFR and circular speed of the galaxy for morphologically distinct galaxies.

Outflows are also detected using UV spectroscopy of distant Lyman break galaxies (e.g. Shapley et al., 2003). Also the spectra of background quasar show the signatures of outflowing gas from galaxies situated in line of sight. Recently Tumlinson et al. (2011) reported extended O VI absorption features in halos of galaxies, detected in the spectra of background quasars. These authors concluded that many galaxies may have had confined outflows which created circumgalactic gas reservoirs. In general there are many absorption line features are found in quasar spectra in SDSS such as C IV , Mg II and so on. The general consensus is that the strongest (EW> 1 Å) arise when the line of sight passes through the disc of the galaxy, and the week lines may originate when the line of sight passes through the extraplanar material. The width of the lines suggest a speed ~ 100 km s^{-1} for this extraplanar gas. This gas may be outflowing with this speed and may constitute a week galactic wind in these galaxies (Prochter et al., 2006a).

Morphologically the winds have many different shapes. In galaxies with very high SFR, outflows are more or less isotropic with respect to the galactic centre. Outflows in disc galaxies with moderately high SFR, are bipolar in nature and they have a conical geometry. The cone opening angles are observed to be in the range of $10°$–$100°$. Outflows with large cone opening angle typically have large mass loss rates. The review by Veilleux et al. (2005) provide detailed information on the aforementioned facts.

We would like to mention here a few limitations of the observations. To start with, although the X-ray observation give vital information on the spatial extent of the outflow and the temperature, it doesn't provide any information of the velocity. Absorption line studies provide accurate information for the dynamics of the outflowing gas, however the position of the outflowing gas is poorly constrained and for face on galaxies can not be determined at all.

1.3.2 Different phases of galactic outflows

Different observation probe the gas differing in thermal and physical properties. For example, X-rays probe the diffuse hot gas while spectral lines probe the cold/warm clumpy gas. Therefore, galactic winds are a multiphase phenomena. We would like to categorise the outflows depending on various phases we observe. We can identify following three different phases of the galactic winds.

1.3.2.1 Hot (ionized) phase

The gas in the hot phase is termed 'hot wind fluid' or simply 'hot wind' in literature. This phase of the wind is detected in X-rays. The soft X-ray emission extending to distances of ~ 10 kpc has been found in many galaxies (e.g. Strickland et al., 2004). The temperature of this hot component is of the order of ~ 0.1 keV (Martin, 1999). This hot phase is theoretically modelled as a continuously expanding steady wind passing through a critical point, located in the central regions of galaxy where SNe mass and energy injection is thermallized. There are generally two views about the origin of soft X-ray emitting gas. In many galaxies such as the Sombrero galaxy this hot gas is assumed to be in hydrostatic equilibrium with the halo and thus it is called the extended corona. This interpretation may be correct for quiescent galaxies such as our Milky Way, but for vigorously star forming galaxies such as M82 this emission is more prominent and a strong outflow may be inferred, which is supported by spectral line studies as well. Therefore the X-ray emitting extraplanar gas in starburst galaxies is most likely the hot phase of strong galactic wind.

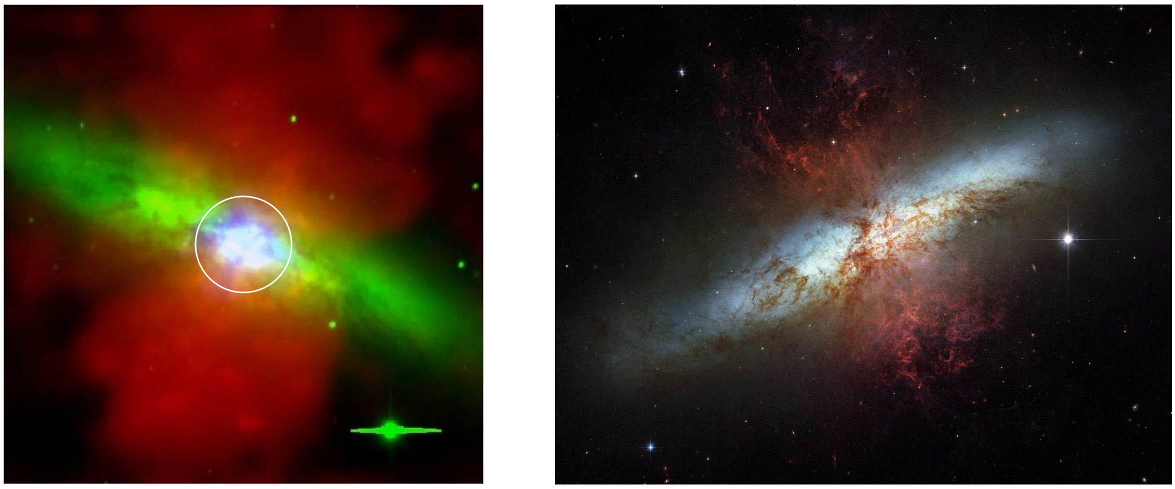

Figure 1.3: Galactic Wind in M82. *Left panel* : Soft X-ray emission in the 0.3-2.8 keV energy band from the starburst galaxy M82 is shown in red. Also shown is the optical R-band emission (starlight) in green, and diffuse hard X-ray emission in the 3-7 keV energy band in blue. The image is ∼5 kpc on a side. The white circle encloses a spherical region with radius 500 pc. Image is taken from Strickland & Heckman (2009). *Right panel* : In this HST image, Hα emission from the filamentary and clumpy superwind of M82 is shown in red. Hα emission probes the gas roughly at a temperature of 10^4 K. Image credits to NASA, ESA, Hubble Heritage Team STScI/AURA and J. Gallagher (University of Wisconsin), M. Mountain (STScI) and P. Puxley (NSF).

1.3.2.2 Cold/Warm phase

The colder phase of the wind which typically has a temperature $\sim 10^4$ K is detected through the Hα, Na D and Mg II lines. The Hα line probes the ionized gas and Na D and Mg II lines probe the neutral gas. This neutral to partially ionized phase of the wind is clumpy in nature. For example one can see in the right panel of Figure 1.3, that the cold/warm phase is filamentary and clumpy in contrast to the smooth distribution of the hot phase shown in the left panel. The cold phase of winds has been studied extensively, mainly because of two reasons. Firstly, we can measure the velocity of this phase precisely due to the presence of Doppler shifted spectral lines, therefore firm conclusions can be drawn for its dynamics. Secondly, the origin and survival of cold clumps remains a puzzle from theoretical point of view. In the standard scenario of SNe/starburst driven winds, the origin of this phase has been

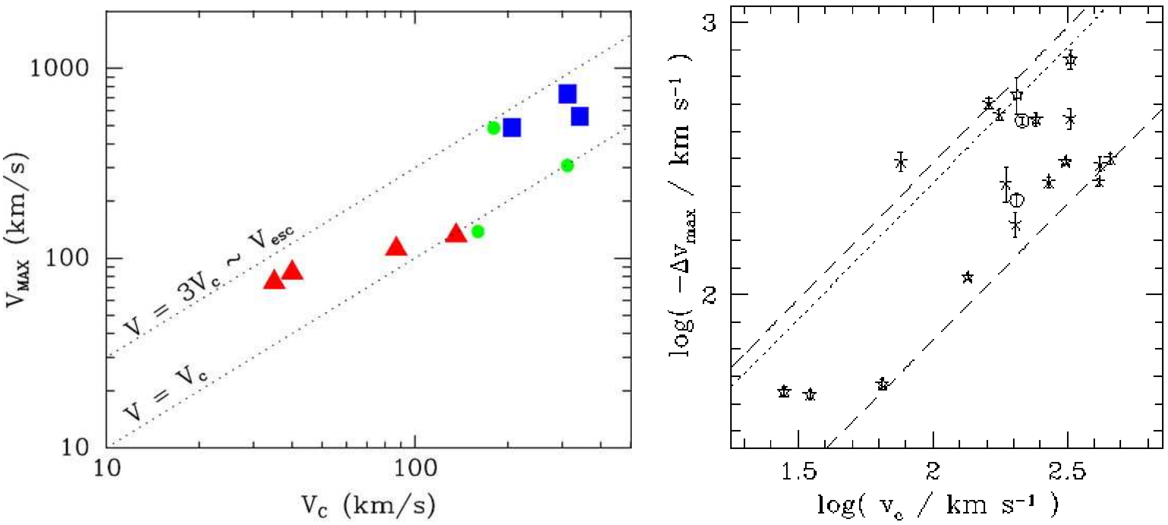

Figure 1.4: The correlation between the cold/warm wind speed and the circular speed of the galaxy. The *left panel* is from Martin (2005), where the three representative data sets are used to show the correlation of outflow velocity with the circular speed of galaxy. The triangles are for dwarf starbursts (Schwartz & Martin, 2004), circles are for luminous infra-red galaxies (Heckman et al., 2000) and the squares represent the outflows detected in ultra luminous infra-red galaxies (Martin, 2005). The results of another study by Rupke et al. (2005b) are shown in the *right panel*, in which similar correlation is reported. (Credit for the left panel to C. Martin and for the right panel to D. Rupke).

linked to thermal instability of the hot phase of the wind. Furthermore it is believed that the clumps formed from the main flow are dragged with it due to the ram pressure and thus the dynamics of the cold phase is controlled by the hot phase of the wind. Observations suggest a more or less constant velocity for the hot phase of wind as inferred from X-ray temperatures in many galaxies in a range of circular speeds (Martin, 1999). Therefore, one would expect the velocity of the cold phase to scale with the hot wind velocity and be independent of galactic circular speed as well. Earlier observations supported this scenario (Heckman et al., 2000). However, recent studies report a correlation between the cold wind velocity and the galaxy circular speed as shown in Figure 1.4 from Martin (2005); Rupke et al. (2005b). These results led to new theoretical developments as explored in chapters 2, 3 and 4 of this thesis.

1.3.2.3 Molecular phase

Several studies have been carried out, most of them focused on M82, to detect molecular lines in the galactic outflow. Taylor et al. (2001) reported extraplanar CO emission in M82 extended upto ~ 6 kpc, and moving with velocity $\sim 100\ \mathrm{km\,s^{-1}}$. Walter et al. (2001) presented another study based on CO line, and proposed a cone of molecular outflow with opening angle $\approx 55^\circ$. Recently, Veilleux et al. (2009) have reported the detection of molecular hydrogen which is extended and spread in patches in the superwind region of M82. These authors infer a temperature of the order ~ 100 K for the molecular gas. The existence of the molecular gas at such extended scales above the galactic plane poses questions. It is possible that the molecular phase forms due to the radiative cooling of other two hotter phases. In this case the cool molecular gas may reside in the cores of warm ($\sim 10^4$ K) clouds. Detection of molecular phase is anyway a remarkable fact. It is interesting to find all the three standard stable phases of the interstellar medium in the galactic outflows. The old and new observations together pose a vast range of problems for theoretical studies.

1.4 Outflow mechanisms

1.4.1 Starburst/SNe driven outflows

SNe explosions are the micro-engines of galaxies, which inject energy, gas and metals in the interstellar medium and thus provide fuel for further star formation. SNe explosions drive a shell of compressed material which slows down and finally fragments via cooling and Rayleigh-Taylor instabilities. A large SFR implies a large SNe rate as well. The energy injected by SNe should then depend on the SFR. For starburst galaxies the ISM is highly influenced by the SNe and as a combined effect of multiple SNe the shell of compressed material may break out of the galaxy, creating a hole in the disc where a steady free-wind can develop.

1.4.1.1 Condition for superwind

The condition which should be fulfilled in order that SNe can drive a large scale outflow was first discussed by (Larson, 1974). The argument was based on a comparison between the cooling time (t_c) of the SNe driven shell and the characteristic collision time ($t_{\rm snr}$), which is the time taken by a single SNe to cover half of the volume of the space which it will finally occupy. Thus at a time $t_{\rm snr}$, the SNe will have half of its volume heated again by another SNe. Clearly the characteristic cooling time depends on the frequency of SNe in a given volume. Using this Larson (1974) derived a critical value of star formation required for the medium to be kept hot so as to start a subsonic pressure expansion which can turn into a large scale supersonic outflow of matter.

The existence of a hot tenuous phase in the ISM as a result of high star formation and SN rate was studied by McKee & Ostriker (1977). Following this work, we can write the filling factor of the hot medium created by multiple SNe in any given volume as, $f = 1 - e^{-Q}$, where, $Q = SVt_{\rm max}$ is the porosity of the ISM. Here, S is the SN rate, and V is the volume of the nuclear region, $t_{\rm max}$ is the time when the SN remnant will stop expanding (i.e. when the inner pressure is roughly half of the outside pressure). Using the results of Chevalier (1974) for $t_{\rm max}$ and R_E, we can write $Q = 10^{0.7} E_{51}^{1.28} S_{-12} n_1^{-0.14} P_4^{-1.3}$. where E is the energy of SN in units of 10^{51} erg, n_1 is the ambient gas density in units of particle/cc, P_4 is the pressure in units of 10^4 k$_B$ K/cc, typical of the ISM in disc galaxies. According to Salpeter IMF, typically 10^{-2} SNe occur for a unit solar mass of star formation. Thus we can replace the SN rate S by the corresponding SFR per unit volume. Furthermore, for the disc galaxies we can multiply the SFR per unit volume with the disc thickness to obtain the star formation rate surface density ($\Sigma_{\rm SFR}$). Using an approximate value of a unit kpc for the disc thickness, we obtain the following relation for the quantity Q,

$$Q \approx \; 5 E_{51}^{1.28} \, n_0^{-0.14} \, P_4^{-1.3} \, \Sigma_{\rm SFR,0.1} \, H_{\rm kpc}^{-1} \tag{1.1}$$

which is larger than unity and hence implies a filling factor of $f \approx 1$, thus the nuclear region should be filled with hot gas shaken by repeated SNe. In the above equation, if we set the criteria for the outflow to be $Q \gg 1$, then it would translate to the criteria in star formation surface density, given by $\Sigma_{\rm SFR} \gg 10^{-1.7}$ M$_\odot$ kpc^{-2} yr^{-1}. Observations agree well with this criteria as the outflows are generally seen in galaxies with a global $\Sigma_{\rm SFR} \approx 0.1$ M$_\odot$ kpc^{-2} yr^{-1} (Heckman, 2002).

1.4.1.2 A broad picture

Once the nuclear region is filled with hot tenuous gas and a so called *hot cavity* is formed, it starts expanding due to its own pressure and drives a thick compressed shell of the gas through the stratified atmosphere of the galaxy. In Figure 1.5 we have shown a schematic diagram of the SN driven wind model from Heckman et al. (1990). In the left panel of the figure the shell driven by energy injection is shown expanding through the vertically stratified medium in a disc galaxy. The compressed shell is of high density and hence it is prone to radiative cooling and Rayleigh-Taylor instability. At some stage this shell fragments due to the instabilities, and facilitates the escape of freewind beneath it. This is when the transition from a *snow plough* to *blow out* phase is said to take place.

The free wind is discussed by many authors using the steady trans-sonic solutions (e.g. Chevalier & Clegg, 1985). We can estimate a few parameters for the free wind. The velocity of the free-wind can be obtained by equating the energy injection rate to the mechanical luminosity in the hot cavity, ($\frac{1}{2}\dot{M}v^2 \; = \; \dot{E}$). Thus one obtains a velocity $v \sim (2\dot{E}/\dot{M})^{1/2}$. Considering an extreme case with a high degree of energy injection we can use, $\dot{E} \sim \left(f_{\rm SN} 10^{51} \, \frac{\rm SFR}{\rm M_\odot/yr} \right)$ erg yr^{-1}, where $f_{\rm SN}(\approx 10^{-2})$, is the fraction of SNe per unit

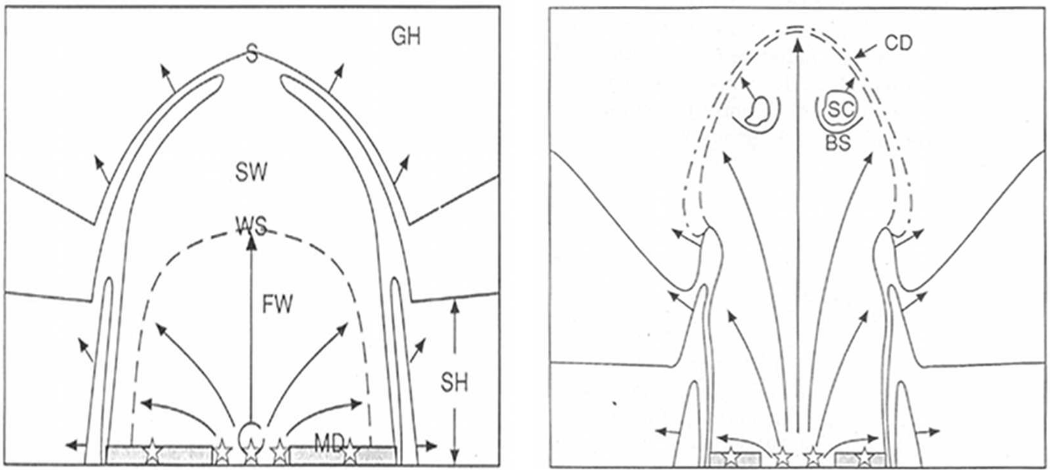

Figure 1.5: Schematic of starbusrt/supernovae driven outflow. The supernovae explosions and the stellar winds in star cluster drive a bubble of gas as shown in the *left panel*. If the mechanical luminosity of starburst is large enough the bubble breaks out of the plane of disk and fragments leaving a freewind behind as shown in the *right panel*. The fragments of supershell constitute the colder phase and these are entrained in the free hot wind. (Source of the figure is (Heckman et al., 1990). Credit for the figure to T. Heckman (JHU)

solar mass of star formation. Further by taking $\dot{M} \sim \mathrm{SFR}$, we get $v \sim 10^3\ \mathrm{km\ s^{-1}}$, which is greater than the escape velocity of galaxy and can escape easily into the IGM.

Hydrodynamic simulations to capture the essentials of SN driven winds have been carried out by several authors. Suchkov et al. (1994) simulated the effects of energy injection and wind evolution using Eulerial code and confirmed the ideas presented in Heckman et al. (2000). This calculation revealed features such as the initial blowout and the development of free wind in which cold clouds were embedded. The soft X-ray emission, the neutral emission were also reproduced (see also Strickland & Stevens (2000)). Mac Low & Ferrara (1999) set up the hydrostatic distribution of gas in accordance with NFW dark matter gravity and studied the conditions for blow out of gas from the galaxy, as a function of the mechanical luminosity. In a simulation of outflows driven by SNe from disc galaxies, Dubois & Teyssier (2008) found that the outflowing gas has to contend with infalling material from halo, which inhibits the outflow for a few Gyr. Fujita et al. (2004) also studied outflows from pre-formed disc galaxies in the presence of a cosmological infall of matter. In a recent simulation, Cooper et al. (2008) carried out a 3-D simulation of galactic outflows with radiative cooling. These authors implemented the mass and energy injection due to SNe, at discrete points in the galactic disc. They found that the outflow has conical structure with cold phase filaments present throughout the hot superwind.

Let us turn to the observations of the colder phase observed in neutral lines in starburst (see §1.3.2.2). To account for these observations, it is proposed that the cold clouds are formed as fragments of initial breakout of the free wind, due to a combined effect of breakout and radiative cooling. Dynamics of these clouds is governed subsequently by the ram pressure offered by the free wind in which these clouds are embedded. However this picture has met with difficulties in recent years. Absorption line studies of outflows suggest a strong correlation between the cold/neutral outflow speed and the galaxy circular speed thereby hinting at a driving mechanism which is more directly related to galaxy properties, compared to the ram pressure driving discussed above where the existence of a strong wind is essential. It has been shown that the models based on radiation pressure driving work better in explaining this correlation compared to the ram pressure driving.

1.4.2 Outflows driven by galactic radiation

Apart from providing thermal energy the starbursts and SNe are sources of photons as well. The radiation thus emerging from galaxy may cause the expulsion of material. The force exerted by the photons on the gas depends on the mechanism of absorption or scattering of photons. Photon to dust scattering opacity can be as large as $\sim 10^3$ cm^2 g^{-1}, hence the dust can easily be driven out of the galaxy as studied by Aguirre et al. (2001) in the context of metal enrichment of IGM (see also Bianchi & Ferrara 2005). For stellar winds from massive stars it is now generally expected that the mass loss occurs via a mechanism in which radiation acts on dust grain which in turn are coupled with the gas via physical or coulomb collisions. Scoville (2003) used this combined dust and gas mass loss by radiation driving in setting a maximum luminosity for star forming galaxies.

Murray et al. (2005) considered radiation driven dusty outflows from galaxies and proposed a critical luminosity of galaxies based on an Eddington-type argument. Interestingly their calculation showed that the observed correlation between the outflow speed and the galaxy circular speed shown in Fig. 1.4, comes out naturally in this case of radiation driven outflows. We would like to discuss some basics of radiation driven outflows. Murray et al. (2005) assumed an isothermal distribution of total mass in the galaxy, given by $M(r) = 2\sigma^2 r/G$, where $\sigma = \sqrt{\frac{GM_{\rm vir}}{2r_{\rm vir}}}$ is the velocity dispersion. The time independent dynamics of dust and gas mixture is governed by following equation,

$$v\frac{dv}{dr} = \frac{\kappa L}{4\pi r^2 c} - \frac{2\sigma^2}{r} \tag{1.2}$$

where L is the luminosity which may be due to SNe, stars and/or an AGN, κ is the opacity of a dust-gas mixture. This equation can be integrated to obtain the following asymptotic wind speed,

$$v_\infty \simeq 2\sigma \sqrt{\ln(r_{\rm vir}/r_b)}\sqrt{\frac{L}{L_c} - 1} \tag{1.3}$$

where r_b is the launching radius, and $L_c = [(8\pi\sigma^2 c\, r_b/\kappa)\ln(r_{\rm vir}/r_b)]$, is the critical (Eddington) luminosity required for driving the outflow. For a fixed value of the ratio L/L_c greater than unity, we obtain $v \propto \sigma$. Therefore, when the luminosity of the galaxy is greater than the critical value (L_c), then the radiation force exceeds the gravity and mass outflow occurs.

The above calculation assumes that the outflowing gas is optically thin. However, similar result is obtained for the optically thick case as well. For the dynamics of an optically thick envelope, we can write,

$$M_g(r) v \frac{dv}{dr} = \frac{L}{c} - M_g(r)\frac{2\sigma^2}{r} \tag{1.4}$$

where $M_g(r)$ is the mass distribution of the gas, which is related to the total mass distribution through, $M_g(r) = f_g M(r)$, where f_g is the gas fraction. The above equation can be integrated to yield once again the solution given in equation (1.3), with L_c in optically thick case defined as $L_c = (4 f_g c\, \sigma^4/G)$. Although the radiation driven model work well in accounting for the observed correlations such as the proportionality of the outflow speed to the velocity dispersion or the circular speed, however, it hinges upon the crucial parameter of opacity or the cross section of interaction between photons and dust grains. For large dust scattering opacity in UV, the radiation driving seems plausible. However, UV radiation may not survive upto large distances in the galaxies. The dust grains reprocess the UV in IR and this is also obvious in the spectral energy distribution of galaxies where the main part of starlight is in IR bands. Recent simulations and radiation transfer calculation also highlight this where the general outcome is that in normal galaxies UV luminosity is not enough for driving a large scale outflow (e.g. Novak et al., 2012). However, there are still IR photons and, although the cross section in IR is not as high as in UV, but a combination of IR to dust scattering and the enhanced IR luminosity due to the contribution from an AGN, may drive strong outflows. We wish to take the reader through these calculations in detail, starting from driving by UV photons in chapter 2 and then by IR photons in chapter 5 of this thesis.

1.4.3 Cosmic ray driven outflows

The physics of cosmic ray driven outflows is based on the scattering of cosmic rays by the Alfven waves, the so called ‘streaming instability’. Cosmic ray particles gyrate around the magnetic field lines and undergo change in their pitch angle as they move. Relativistic cosmic rays undergo a large reduction in velocities and finally end up drifting with the underlying Alfven waves. Therefore the bulk velocity of the cosmic rays becomes equal to the Alfven wave velocity. The theoretical basis for the above mechanism had been worked out long ago by (Wentzel, 1968; Kulsrud & Cesarsky, 1971; Skilling, 1975) . In the process the gas gain energy and momentum and thus the coupled two phase medium consisting of cosmic rays and the gas can flow out as a galactic scale outflow. Ipavich (1975) worked out the relevant fluid equations and discussed a steady large scale trans-sonic outflow from galaxies, where cosmic rays supply the necessary energy and momentum. More sophisticated models for cosmic rays driven winds were later worked out in which it was shown that gas flow may exist along the streamlines which are essentially the magnetic flux tubes emerging from galactic plane and extending to large distances. (e.g. Breitschwerdt et al., 1991; Zirakashvili et al., 1996). Recently, Samui et al. (2008) studied both hot and cool outflows from a realistic NFW dark matter halo. Recent work on cosmic ray streaming show that the drift speed of cosmic rays in case of high-β plasma, is proportional to the thermal or sound speed (Enßlin et al., 2011, and references therein). Uhlig et al. (2012) implemented the physics of cosmic ray streaming in SPH code GADGET and studied the outflows from galaxies (see also Jubelgas et al., 2008). This study concluded that cosmic rays can drive the outflows from the low mass $(M \leq 10^{12} \mathrm{M}_{\odot})$ halos.

1.4.4 AGN driven outflows

Observationally it has been hard to establish that outflows in galaxies would have been powered by AGN (Rupke et al., 2005a; Westmoquette et al., 2012). However, recent observations show compelling evidence for the AGN driving in galactic outflows (Sturm et al., 2011; Rupke & Veilleux, 2011; Alexander et al., 2010; Morganti et al., 2007; Dunn et al., 2010; Feruglio et al., 2010; Fu & Stockton, 2009; Villar-Martín et al., 2011).

AGN is a powerful source of radiation. The radiation from AGN can scatter off the electrons and can accelerate them to high velocities. The AGN can be considered a point source of radiation and gravity hence the force due to radiation and gravitation depend inversely on the square of distance from the centre. The ratio of two forces is a constant and can be written as $\Gamma = \kappa_T L/(4\pi G M_\bullet c)$, where κ_T is the Thomson scattering opacity, L is the AGN luminosity and $M_\bullet$ is the mass of the black hole. By setting $\Gamma = 1$, we can define a critical Eddington luminosity due to Thomson scattering ($L_{\mathrm{edd}} = 4\pi G M_\bullet c/\kappa$) required to drive the outflows. For a black hole of mass 10^8 $\mathrm{M}_\odot$, the Eddington luminosity is $L_{\mathrm{edd}} \sim 10^{46}$ erg s^{-1}. The AGN is situated deep inside a galaxy and its radius of gravitational influence is more than three orders of magnitude smaller than the scale height in a galaxy. Therefore the outflows due to Thomson scattering move freely on the scales of a few pc, after which, they encounter the dense ISM. These fast nuclear outflows plough through the ISM and drive compressed shells of gas. Apart from these fast nuclear winds the AGN can fuel the dust(radiation) driven outflows, through scattering of UV photons off the dust grains in surrounding ISM (Murray et al., 2005). The UV to dust scattering cross section is roughly thousand times greater than the Thomson scattering cross section (Li & Draine, 2001). Interestingly, at a distance of a kpc from the AGN, the gravitational force will mainly be due to bulge of the galaxy and therefore would be roughly a thousand times the gravity due to central black hole, because of the $M_\bullet$–σ relation. This reveals an interesting fact, that if the AGN is at the Eddington limit due to Thomson scattering then it would also be at the Eddington limit set by dust to UV scattering. Therefore an Eddington limited AGN may drive strong galactic scale outflows as well.

Many sophisticated models have been developed for AGN driven galactic outflows. Murray et al. (2005) proposed the existence of a critical luminosity for the AGN (or the galaxy) necessary for the blow-out of all the available gas. The value of this critical luminosity depends on the dust scattering opacity at UV. Everett & Murray (2007) studied Parker wind from AGN occurring at scales of ~ 100 pc. Debuhr et al. (2012) carried out simulations showing that the initial momentum injection and the fast outflow in the vicinity of hole may shock the surrounding ISM and can result in a galaxy scale outflow. Whether the outflows due to the AGN are energy or momentum conserving has been a topic of debate as well. Silk & Nusser (2010) argued that energy driven outflows are not possible in the galactic bulges. King et al. (2011) proposed that AGN outflows are momentum driven at small scales and energy driven on larger scales. Faucher-Giguère & Quataert (2012) showed that the cooling in the region, shocked by AGN radiation pressure, may not be effective and the outflows can be energy conserving. McQuillin & McLaughlin (2012) studied the large scale motion of momentum-conserving supershells from a dark matter halo. Recently, Novak et al. (2012) carried out a radiation transfer calculation assessing the efficiency of various components of AGN spectrum in driving outflows. This work showed that most of the UV flux is quickly absorbed and re-radiated in IR. The IR radiation can drive a dusty outflow and may result in mass loss much higher than the line driving mechanisms, on scales connecting the AGN and host galaxy as shown by radiation hydrodynamic simulations (Dorodnitsyn et al., 2011).

1.5 Quasar absorption lines and outflows

We discuss here the absorption lines in the spectra of quasars and the nuclear winds from the AGN, and thus provide the background for the work presented in chapter 6 of this thesis.

Absorption line systems in the quasar spectra come in a wide variety. There are ‘intrinsic’ systems which are classified as the broad absorption lines (BAL) with a large trough of absorption ($\Delta v \sim 10^3$–$10^4 \ \mathrm{km\ s^{-1}}$) which possibly arise due to an accretion disc continuous wind, and the narrow absorption lines (NAL) with line widths ($\sim 100 \ \mathrm{km\ s^{-1}}$). Apart from these, a vast majority of absorption systems such as C IV , Mg II and so on, are generally called the ‘intervening systems’ and these systems are seen blueward of the Lyα emission in quasar spectra.

Out of these absorption systems the BAL systems are generally thought to arise in outflows launched from the accretion disc around the black hole. The AGN is a strong source of radiation, and it likely produces radiation driven outflows, which may explain the BAL region. Scoville & Norman (1995) proposed a dust radiation riven outflow emerging from close quarters (~ 1 pc) of the AGN. Later Murray et al. (1995) worked out a model of line-driven wind emerging from the accretion disc around the black hole in order to explain the BAL regions. Recently, Dorodnitsyn et al. (2011) have shown that IR driving of dust and gas may cause the formation of outflowing dusty torus around the black hole.

The intervening Mg II systems are thought to be formed due to gas in galaxies situated in the line of sigh of a background quasar. In this scenario, the weak systems (equivalent width < 1 Å) are thought to arise, when the lines of sight pass through the halos of galaxies. These weak systems may be inflowing or outflowing with respect to the centre of the galaxy. On the other hand, the strong systems (EW $\gtrsim 1$ Å) may arise when the line of sight passes through the disc of the galaxy. This notion of Mg II arising in galaxies situated at cosmological distances from quasars has only been verified independently for less than 10 % of the cases. Also, recent studies have found signatures of the association of these absorption lines with the quasar itself (Bergeron et al., 2011). These facts indicate that, there may be an alternative (intrinsic) origin of these Mg II systems, where they may be outflows driven by quasar radiation and approaching towards us with high terminal velocities $\sim 0.1c$, which indeed is possible in dust-radiation driven wind scenario (e.g. Scoville & Norman, 1995). Mg II absorption lines, Doppler shifted by a huge margin from quasar redshifts can easily arise in these radiation driven outflows.

1.6 Open questions and motivations for this study

- *The correlation between the wind velocity and the galaxy circular speed :*
  Simulations of galaxy formation show that momentum driven wind with wind speed proportional to the circular speed of galaxy, reproduces the galaxy luminosity function and IGM metallicity. Similar correlation is also seen in the observations of cold neutral outflows (see Fig 1.4). Theoretically the outflows from a disc galaxy, driven by the radiation field of the luminous disc, are unexplored. This motivates us to study the radiation driven wind from the disc.

- *What drives the cold outflows : ram pressure or radiation pressure ?*

In the standard scenario of SNe/starburst driven outflow, it is generally thought that the clumps forming cold phase of outflow, are dragged due to the ram pressure of the hot phase. However, the observed correlation of cold wind speed and galaxy rotation speed is better explained by only radiation driven wind scenario. However, the ram pressure can not be neglected if the cold clumps are embedded in the hot flow. It therefore becomes important to study the combined ram pressure and radiation pressure driven outflows, which will determine the regime of galactic mass and SFR in which the ram pressure is important and, the regime in which radiation pressure prevails.

- *Observed high velocity outflows ($v > 1000\ \mathrm{km\ s^{-1}}$) in AGN host galaxies :*
  Detection of AGNs in outflow hosting ULIRGs have been an active area of research in recent years (e.g. Rupke et al., 2005a). Many of the ULIRGs host an AGN at their centres. However, we are not sure whether AGNs have any role in driving outflows in these galaxies. Recent studies reveal an interesting dividing line between AGN driving and pure starburst/SNe driving (Tremonti et al., 2007; Sturm et al., 2011). These studies indicate, if the galaxies hosting an AGN have outflows then the speed of the outflow exceeds $1000\ \mathrm{km\ s^{-1}}$. This interesting finding begs a theoretical explanation.

- *Effect of gravity due to dark matter halo in quenching the outflows :*
  The hydrodynamical steady wind model of Chevalier & Clegg (1985) ignores gravitational force, which is justified for M82 and other dwarf starbursts where outflow speeds are quite large than the galactic escape speeds. The effect of gravity have been studied for cosmic ray driven outflows recently (Samui et al., 2008). However, there have been no analytical extension of the steady hydrodynamic SNe driven wind model, which includes the proper gravitational force of a dark matter halo. This motivates us to construct analytic steady wind solution for a NFW dark matter halo, with energy and mass injection from the SNe.

- *Can reprocessed Infra Red (IR) radiation from AGN drive galaxy scale outflows ?*
  The UV radiation from galaxies can drive strong outflows in which photons are scattered off the dust grains and inject momentum. The gas in turn is coupled with the dust and can be propelled as an outflow (Murray et al., 2005; Sharma et al., 2011). However, this idea has been questioned recently on the argument that the UV light is heavily attenuated and reprocessed in IR and may not be available in amounts required for driving. As for the driving due to IR, the opacity in IR is two orders of magnitude smaller than in UV (Li & Draine, 2001), therefore, it is speculated that IR radiation is not capable of driving outflows (Socrates & Sironi, 2013). However, this conclusion

may change if one considers the enhanced IR luminosity due to the presence of an AGN. Quantitative estimates are needed to test these ideas.

- *Mismatch between halo mass function and the galaxy luminosity function 'aka' dependence of the stellar mass on halo mass :*
  This is the main cosmological motivation for studying galactic outflows. It is generally believed that feedback plays an essential role in shaping the galaxy luminosity function. However, the semi-analytic models asses the amount of feedback through few free parameters. How the galaxies produce this feedback (outflows), and the possible dependence of outflow velocity and mass loss rate on galactic mass, are some of the questions which are still under debate.

- *Are all the MgII absorbers in quasar sightlines intervening ?*
  Magnesium absorbers in quasar sightlines are thought to arise in galaxies falling in the line of sight. The reason for considering these systems as intervening is the large velocity offset (or equivalently the redshift difference) between the quasar emission line and Mg II absorption lines. However the dust radiation driven winds may accelerate to velocities as large as $\sim 0.1\ c$ (Scoville & Norman, 1995). Therefore, it is worth considering the possibility that, many of the absorbers might originate in radiation driven outflows from quasars. This idea can be explored by studying for correlation between the velocity offset and the quasar luminosities.

1.7 Plan of the Thesis

In **chapter 2**, we study the dynamics of dusty outflows driven by radiation from the galaxy. We consider the momentum injected by photons to dust grains which are coupled with the gas and study the wind along the pole (z–axis) of the galaxy. We consider the gravitational field due to bulge, disc and dark matter halo. We derive the conditions for escaping winds in terms of the disc Eddington factor at the base (Γ_0), which is the ratio of the force of radiation to that due to gravity for a uniform disc. We find that for a constant Γ_0, the outflow speed is proportional to the circular speed (v_c) of galaxies. We then calculate the expected value of Γ_0 for an instantaneous starburst and the calculate the corresponding outflow speed.

In **chapter 3**, we present 2-D numerical calculation in cylindrical co-ordinates to study radiation driven wind. We consider the radiation force from a uniform density disc and from a realistic exponential disc in this simulation. We explore the 2-D structure of the wind and rotation of the wind material.

In **chapter 4**, we construct a ballistic outflow model for the motion of neutral clouds above the plane of the galaxy. The dynamics of a cloud is studied as an interplay of the force due to radiation and the combined gravity of disc, bulge and dark matter halo. We consider the driving due to radiation from the disc (mediated by dust grains) and also ram pressure force due to a hot continuous wind. The ram pressure is directly proportional to the mass loss rate and hence to the SFR of the galaxy. We consider the radiation force due to a continuously star forming disc, therefore, it also depends on the SFR. The gravitational forces depend on the mass of the galaxy and hence on the circular speed (v_c). We then study the dynamics of clouds in the parameter space of SFR and v_c, which covers a wide range of galaxies in which outflows are observed. We derive the critical value of SFR and v_c, for producing outflows and also explain theoretically the observational threshold of star formation surface density required for galaxies to show outflows.

In **chapter 5**, we study hydrodynamic wind in which the energy and mass injection is supplied by SNe and the momentum injection from an AGN, are both included in the same framework. We then describe two modes of SNe energy injection which can be related to the two modes of star formation in galaxies, a *quiescent* mode and a *starburst* mode. We consider the momentum injection from IR radiation from the AGN. We derive an analytic solution for this problem and calculate the wind velocity, gas density and temperature as a function of distance from the centre. We find out the conditions for escape and calculate asymptotic terminal speed of the wind. We quantify the galactic mass for which AGN should be effective and the outflow speed in this case. We then derive the scaling between the stellar mass and the halo mass, based on an interplay between the infall, gas cooling, star formation and mass loss.

In **chapter 6**, we report a correlation of the velocity offset (β) of Mg II absorption line in the spectra of quasars and the bolometric luminosity of the quasar. It is believed that strong Mg II absorbers in the quasar spectra arise due to intervening galaxies. However, these Mg II lines can also arise if the absorbers are the material outflowing with high velocity ($\sim 0.1\ c$) with respect to the quasar and moving toward the observer, so that the origin of line shift will then be due to the Doppler effect. In this scenario, if outflows are driven by radiation then a correlation between the velocity offset of absorbers and the luminosity of quasar is expected. We search for this correlation in SDSS data release 7 and report our findings.

We conclude and summarize our results in the last **chapter 7** of this thesis. At the end we have included supplementary material as Appendices, including a calculation of cosmic ray driven winds in Appendix G.

Chapter 2

Radiation Driven Wind from Disc Galaxy

Based on :
Sharma, M., Nath, B. B. & Schekinov, Y. 2011, ApJ, 736, L27

Galactic outflows are important as a feedback process which shapes the observed properties of galaxies like the stellar mass and metallicity. In the face of competing theories for outflows, cosmological simulations of galaxy formation indicate that momentum driven winds in which the wind speed correlates with the circular speed of the galaxy, better reproduce the observed galaxy luminosity function as well as the IGM metallicity. Such a correlation is also reported in recent NaD and MgII line observations of outflows from a wide range of galaxies. We consider outflows composed of dust and gas, which are driven by radiation from a galactic disc and search for a theoretical answer to the question, as to why such a correlation should exist.

Main Results

- We calculate the force of radiation and gravity from a flat disc. We define the ratio of the force of radiation to that of gravity using a parameter Γ_0.
- Using the scattering opacity for B-band light for a dust-gas mixture, we derive that a minimum value of $\Gamma_0 \sim 3$ is required to drive out the mass from a galaxy consisting of disc, bulge and dark matter halo. We then solve for the speed of radiation driven outflow from a dark matter halo and find that it weakly depends on the redshift given that the dust content is maintained with redshift.
- We find that a maximum mass-to-light ratio of 10^{-2} is required in order to have radiation (dust) driven outflows from galaxy.
- Using the absolute B-band magnitude for instantaneous starburst model of STARBURST99, we find the time evolution of luminosity and hence Γ_0 and find that average value of Γ_0 over the typical lifetime of starburst is ~ 4. Using this we find that the terminal speed of outflow is roughly three times the galaxy circular speed ($v_\infty \approx 3v_c$).

2.1 Introduction

In the standard scenario of starburst/SNe driven outflows, the interstellar medium (ISM) of the starburst galaxy is heated by SNe and the thermal pressure of the hot gas drives the outflow of gas. Larson (1974) argued that SNe in a star forming galaxy can drive an outflow in excess of the escape speed from the galaxy (see also Dekel & Silk, 1986; Tomisaka & Ikeuchi, 1988; Suchkov et al., 1994; Mac Low & Ferrara, 1999). This scenario, however, has met with problems from new observations. Recent neutral line studies of cold outflows ($T \sim 10^4$ K) show that the maximum speed of outflowing gas is correlated with the star formation rate (Martin, 2005). Observations of Lyman break galaxies (LBG) at $z \sim 3$ have also found a correlation between the outflow speed and the SFR, as well as with the reddening due to dust. Also the SN explosions in disc galaxies may only produce a thickening of the disc gas because of the incoherent nature of these explosions (Fragile et al., 2004). The starbursts and SNe not only provide mechanical energy but they are also rich sources of radiation. Moreover, disc galaxies have a plenty of dust present in their ISM and the photon-to dust scattering opacity can be as high as 10^3 cm^2 g^{-1} (Draine, 2003). These facts indicate that radiation pressure on ISM of galaxies may lead to galaxy scale winds.

Wind driving due to to radiation or the so called 'momentum driving' is less explored compared to the standard SNe/starburst driving i.e. the energy driving. Murray et al. (2005) explored the radiation driven outflows from galaxies and showed the existence of critical luminosity of galaxy for driving shells and clouds of gas. Nath & Silk (2009) discussed a hybrid model of outflows with radiation and thermal pressure. Recently, Zhang & Thompson (2012) have calculated the dynamics of dust particles that are driven by radiation of disc galaxies.

In this chapter, we study dust driven gaseous winds from luminous disc galaxies. We calculate the force of radiation and gravity due to a flat (disc) system in §2.2. In §2.3, we estimate the terminal speed of the combined gas and dust flow, taking into account the gravity of the dark matter halo, apart from the disc forces . In §2.3.3 we calculate the disc mass-to-light ratio that is expected from stellar population synthesis models. We use this mass to light ratio to estimate the outflow speed and then compare our results with the observations and cosmological simulations.

2.2 Radiation driven wind from a flat disc

Let us consider a disc of radius R_d, constant surface mass density (Σ) and surface brightness (I). In cylindrical geometry, the force of gravitation, and that due to radiation, along the pole of disc, are given by,

$$f_{\rm grav}(z) = 2\pi G\Sigma \int \frac{zRdR}{(R^2+z^2)^{3/2}} \ , f_{\rm rad}(z) = \frac{2\pi\kappa I}{c} \int \frac{z^2RdR}{(R^2+z^2)^2} \ , \tag{2.1}$$

where κ is the average opacity of dust grains to absorption and scattering of photons, and the limit of integration is from 0 to R_d. The ratio of the radiation force to the gravitational force, which we call the Eddington ratio, increases with the height z, beginning with a value of $\Gamma_0 = \frac{\kappa I}{2cG\Sigma}$ at the disc centre at $z = 0$. From energy conservation, it can be found that the velocity at a height z is,

$$v_z^2 = 4\pi G\Sigma R_d \left(\Gamma_0 \tan^{-1}\left(\frac{z}{R_d}\right) - 1 - \frac{z}{R_d} + \sqrt{1+\frac{z^2}{R_d^2}} \right) \ . \tag{2.2}$$

This would imply a terminal velocity of $v_\infty \approx \sqrt{4\pi G\Sigma R_d(\pi\Gamma_0/2-1)}$, with a lower limit on $\Gamma_0 \sim 2/\pi$ for driving an outflow from the disc. Assuming a flat disc, with average rotation speed of $\langle v_{c,\rm disc}\rangle \sim \frac{1}{2}\sqrt{\pi G\Sigma R_d}$, the terminal velocity can be written as $v_\infty = 4(\sqrt{\frac{\pi\Gamma_0}{2}} - 1)\langle v_{c,\rm disc}\rangle$, which yields a value $v_\infty \simeq 3\langle v_{c,\rm disc}\rangle$, for $\Gamma_0 = 1$. The above estimate is based on the forces due to disc only. The galaxy, however contains a bulge and a dark matter halo which is more massive than the disc. We set out to explore the outflow dynamics by including all these components.

2.3 Gaseous outflows

We explore the dynamics of a steady wind in which dust is propelled outwards by radiation pressure and drags the gas with it. We do not consider the magnetic fields and we assume a perfect collisional coupling between the dust and the gas which is shown to hold in circumstances of cold wind (Murray et al., 2005). In the purview of dust-driven wind model, there is a maximum temperature of the gas in which dust grains can survive for the duration of the wind. We will show below that the characteristic time-scale of these winds is of order 10 Myr. The dust sputtering time-scale in a gas of temperature $T \sim 10^6$ K and density n is $\sim 10^{5.5}(n/1\,{\rm cm}^{-3})^{-1}$ yr for a grain of size $\sim 0.1\,\mu$m, and it is ~ 300 times larger for a 10^5 K gas (e.g. Tielens et al., 1994). For cold/warm winds considered here for which the typical temperature is $\sim 10^4$ K, we can simply ignore the disruption processes.

Another fact which we would like to mention here is that, the Eddington ratio in this problem is different from the one usually defined for a star or AGN. This is because of the cylindrical geometry of this problem, due to which, the Γ varies with z. We thus calibrate our results in terms of Eddington ratio at the base (Γ_0) which is defined as $\Gamma_0 = \kappa I/(2cG\Sigma)$.

Also we emphasize that Γ_0 refers only to disc parameters and $\Gamma_0 = 1$, does not signify Eddington criteria or threshold luminosity for a galactic system which contains a bulge and dark matter halo as well.

2.3.1 Disc, bulge and halo parameters

We consider a disc with constant surface density (Σ) and surface brightness (I), of radius R_d, which engulfs a bulge and has a surrounding halo of dark matter. We assume a spherical distribution of mass in the bulge and the halo. For the bulge, we assume a total mass of M_b inside a radius $r_b \ll R_d$.

We consider a Navarro-Frenk-White (NFW) dark matter halo (Navarro et al., 1996), with total mass M_h. The halo is characterised by a concentration parameter $c = r_{\rm vir}/r_s$. We fix the total halo mass for a given disc mass ($M_d = \pi R_d^2 \Sigma$), by using the ratio $M_h/M_d \sim 1/0.05$, as determined by Mo et al. (1998). We also use the disc exponential scale-length defined by these authors to represent the size of disc (R_d) in this work. The rotation speed implied by the NFW mass profile rises to a maximum value at a radius $R \approx 2r_s$, and it is given by,

$$v_c^2 = v_{\rm vir}^2 \, \frac{c}{2} \, \frac{\ln(3) - 2/3}{\ln(1+c) - c/1+c} \,, \tag{2.3}$$

where $v_{\rm vir}$ is the rotation speed at the virial radius. We choose this value of the maximum rotation speed to represent the v_c of the disc galaxy, since Figure 2 of Mo et al. (1998) shows that the value of v_c from the flat part of the total rotation curve does not differ much from the peak of the rotation curve from halo only. We also use $r_b/R_d \sim 0.1$, and $M_b/M_d \sim 0.5$, consistent with observed range of luminosity ratio between bulge and disc (Binney & Merrifield, 1998). We use radius of the bulge (r_b) as the base (launching) point of the wind.

2.3.2 Wind terminal speed

To determine the terminal speed of the wind, we use the fact that the Bernoulli function is preserved along a streamline, assuming that a streamline extends from the base to infinity. In an isothermal wind the terminal speed tends to infinity as the wind maintains constant sound speed. It is however more reasonable to assume a polytropic equation of state.

One can write the Bernoulli equation for a polytropic gas (with adiabatic index $\gamma = 5/3$) along a streamline along the pole : $\frac{v^2}{2} + \frac{c_s^2}{\gamma-1} + \Phi = E$, where c_s is the sound speed, Φ is the potential and E is a constant. Equating the values at the base and infinity, we get

$$\frac{v_\infty^2}{2} + \frac{c_{s,\infty}^2}{\gamma - 1} + \Phi_\infty = \frac{v_b^2}{2} + \frac{c_{s,b}^2}{\gamma - 1} + \Phi_b \,, \tag{2.4}$$

where v_b is the wind speed at the base ($z = 0$), $c_{s,b}$ is the sound speed at the base, and $c_{s,\infty}$ is the sound speed at infinity, which is negligible.

$$\begin{aligned}\Phi = \quad & -2\pi G\Sigma R_d\Gamma_0 \tan^{-1}(z/R_d) + 2\pi G\Sigma R_d \left(\frac{z}{R_d} - \sqrt{1+\frac{z^2}{R_d^2}}\right) \\ & -\frac{GM_b}{r} - \frac{GM_s}{r_s}\frac{\ln(1+r/r_s)}{r/r_s}\,. \end{aligned} \tag{2.5}$$

where $r = \sqrt{R^2+z^2}$ and $M_s = M_h/(\ln(1+c) - c/(1+c))$. In the above equation, the first term denotes a pseudo-potential due to radiation pressure. The second term refers to the gravitational potential of the disc. The last two terms represent the effect of the bulge and halo gravity. We have also assumed that the bulge exerts a negligible radiation pressure, since the dominant bulge stellar population is old and red and the mean opacity κ of dust grains in these wavelengths is smaller than in blue band.

We note that the values of the potential at the base and infinity are as follows,

$$\begin{aligned}\Phi_b = \quad & -2\pi G\Sigma R_d - \frac{GM_b}{r_b} - \frac{GM_s}{r_s}\left[\frac{\ln(1+r_b/r_s)}{r_b/r_s}\right] \\ \Phi_\infty = \quad & -2\pi G\Sigma R_d\Big(\frac{\Gamma_0\pi}{2}\Big)\,. \end{aligned} \tag{2.6}$$

The radiation pseudo-potential is zero at the base but $\sim 2\pi G\Sigma R_d(\frac{\Gamma_0\pi}{2})$ at infinity along the pole. Since the dark matter halo is truncated at $r_{\rm vir}$, its potential vanishes at infinity.

It is reasonable to assume that the wind speed at the base is comparable to the sound speed in the disc ($v_b \sim c_{s,b}$). Putting it all in equation (2.4), we have the following expression for the terminal speed,

$$\begin{aligned} v_\infty^2 = \quad & \Big[\frac{\gamma+1}{\gamma-1}c_{s,b}^2 + 2\pi\Gamma_0\frac{GM_d}{R_d}\Big] \\ & -\Big[\frac{4GM_d}{R_d} + \frac{2GM_b}{r_b} + \frac{2GM_s\ln(1+r_b/r_s)}{r_b}\Big]\,. \end{aligned} \tag{2.7}$$

In Figure 2.1 we have shown the dependence of v_∞/v_c on Γ_0, and on the concentration parameter c. We have used $c_{s,b} = 0$, as for the cold/warm ($T \sim 10^4$ K) outflows considered here, the sound speed will have a negligible effect on wind dynamics. We note here that, although the sound speed makes a small difference in the terminal speed, it helps establishing a quasi-steady regime in the outflow by redistributing the pressure over the whole flow. The curves in Figure 2.1, show that there is a minimum value of $\Gamma_0 \sim 3$ for the wind to reach infinity. In general the wind speeds are lower for larger c (dashed curve), which is the case of low-mass and more compact galaxies, but the variation is small. It is interesting to note

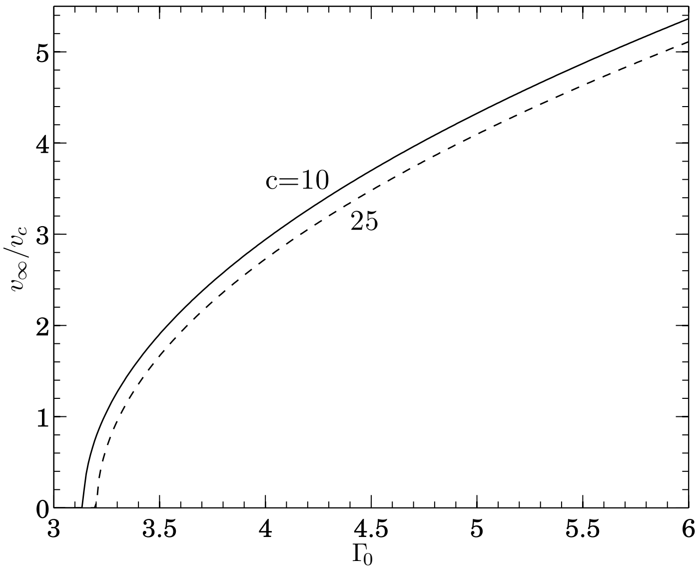

Figure 2.1: The ratio between v_∞ and v_c is shown as a function of Γ_0 for galaxies with two different concentration parameter c, for cold gaseous outflow.

here that the wind requires $\Gamma_0 > 1$.

We next use a relation between the concentration parameter c and galactic mass given by Macciò et al. (2007), and calculate the wind speed for galaxies with different masses, or rotation speeds. One can extend the calculations to higher redshift by using the scaling $c \propto (1+z)^{-1}$. We use $\Omega_0 = 0.27, h = 0.7$, and calculate the NFW parameters for the Λ-cosmology. Figure 2.2 shows the results for v_∞/v_c as a function of Γ_0 for different v_c, at $z = 0$ and at $z = 6$. The curves show that the v_∞/v_c depends mostly on Γ_0 and varies weakly with rotation speed and redshift. We next explore the question what determines the value of Γ_0 which is a crucial parameter for the wind dynamics.

2.3.3 Evolution of wind speed with time

We recall that the value of Γ_0 depends on disc parameters (Σ, I) and dust grain properties (through κ). Consider first the value of Σ/I that is essentially the disc mass-to-light ratio. One can compare the observed values of mass-to-light ratio with the minimum requirement as derived above. Li & Draine (2001) give the mean opacity for gas mixed with dust as ~ 128 cm^2 g^{-1} in U and ~ 93 cm^2 g^{-1} in the B band. Here we shall consider the B band value as a conservative estimate. This gives us a maximum value of disc mass-to-light ratio required for the outflow to occur, given by $M/L \sim \kappa/(2cG\Gamma_0)$. The maximum value thus required is $\frac{(M/M_\odot)}{(L_B/L_{B,\odot})} \equiv \Upsilon_B \sim 10^{-2}$.

This critical limit on disc Υ_B for the galaxy to have winds, is much lower than the observed values in present day disc galaxies. The Milky Way disc has a local value of

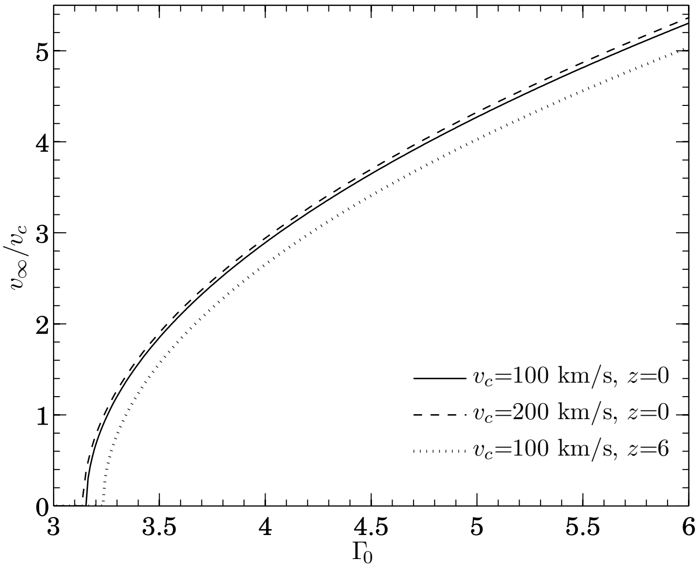

Figure 2.2: The ratio between v_∞ and v_c is shown as a function of Γ_0 for galaxies with different v_c at two different redshifts.

$\Upsilon_B \sim 1.2 \pm 0.2$ (Flynn et al., 2006), and the typical value for disc galaxies is 1.5 ± 0.4 (Fukugita et al., 1998). We note that according to Flynn et al. (2006), a third of the total disc mass comes from gas and the rest from stars. Starburst galaxies can have a much lower value of Υ_B. The estimated $M/L_{\rm bol}$ for NGC 7714 is ~ 0.02 (Bernloehr, 1993a), for regions in NGC 520 it is ~ 0.003 (Bernloehr, 1993b), and for a young super cluster in M82, Smith & Gallagher (2001) has estimated the $\Upsilon_V \sim 0.02$. These low values of Υ are believed to arise from a top heavy IMF and young age of the stellar population, comparing with the predictions from population synthesis models (e.g. Kotilainen et al., 2001; Smith & Gallagher, 2001).

For an instantaneous burst, suitable for starburst galaxies, these models predict an initial period of roughly constant luminosity for $t \leq 3$ Myr followed by abrupt behaviour and then decrease in the luminosity afterwards (Leitherer et al., 1999; Bruzual & Charlot, 2003; Vázquez & Leitherer, 2005). For a Salpeter IMF and a stellar mass-luminosity relation of the type $L \propto M^\beta$, the late-time decay of the luminosity is given by $L \propto t^{-(\beta-1.35)/(\beta-1)} (\propto t^{-0.9}$, for $\beta = 3.5$). The initial period of rather constant luminosity stems from the fact that while low-mass stars are yet to collapse, the massive stars evolve quickly, and the duration of this period corresponds to the main-sequence life-time of the most massive stars.

Using these models we determine the expected disc Υ_B ratio as a function of time after an instantaneous starburst. Using the results from STARBURST99 (Leitherer et al., 1999), for solar metallicity and a Salpeter IMF between 0.1 and 100 M$_\odot$, and using $M_{B,\odot} = 5.45$, we have calculated the Υ_B as a function of time. Using the mean dust opacity for B band,

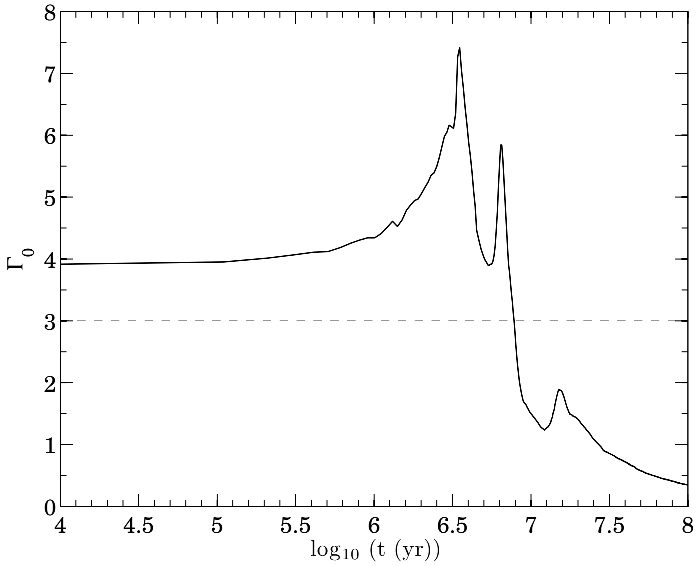

Figure 2.3: The evolution of Γ_0 with time is plotted using a solid line. The dashed line represents the minimum value of Γ_0 required to have a non-zero wind terminal speed.

we calculated the time evolution of Γ_0. We have plotted the Γ_0 as a function of time after the starburst in Figure 2.3. We have also shown the minimum value of $\Gamma_0 \approx 3$ required for having non-zero wind terminal speed using a dashed line. We find that for a period of 10 Myr, Γ_0 stays above the critical value. Time averaged value of Γ_0 over a period of 10 Myr is ≈ 4.2, therefore the galaxy can host a wind for a time of 10 Myr. In this time the wind should be propelled to roughly ~ 7 kpc. A typical starburst lasts for ~ 10 Myr, which implies that, if roughly after this time the old generation of starbursts is replaced by the new, then the starburst galaxies should be able to maintain an average $\widetilde{\Gamma}_0 \sim 4$ for a long time. Using this value, we find the wind terminal speed as a function of galaxy circular speed using equation (2.7). In Figure 2.4, we have plotted the terminal speed for galaxies at redshifts $z = 0, 2, 4$ and 6, using black, red, green and blue lines respectively. From these curves one can infer the result that $v_\infty \propto v_c$. There is a mild flattening for higher redshifts indicating a slope slightly lower than unity, which is due to the dependence of halo concentration parameter on halo mass and redshift.

In Figure 2.4 we also find that the terminal wind speed is roughly three times the circular speed of the galaxy ($v_\infty \approx 3v_c$). This result can be compared with the observed range of maximum wind speed. Martin (2005) found that the maximum speed of clouds embedded in outflowing gas ranges between 2–$3\, v_c$ and Rupke et al. (2005b) found a range of $[0.67$–$3]\, v_c$. Figure 2.2 and 2.4 also show that the wind speed is somewhat smaller at high redshift. The reason is that the galactic mass for a given v_c is smaller at high redshift, but $c \propto M^{-0.2}\,(1+z)^{-1}$, and the mass effect outweighs the redshift effect. However, the variation of v_∞/v_c

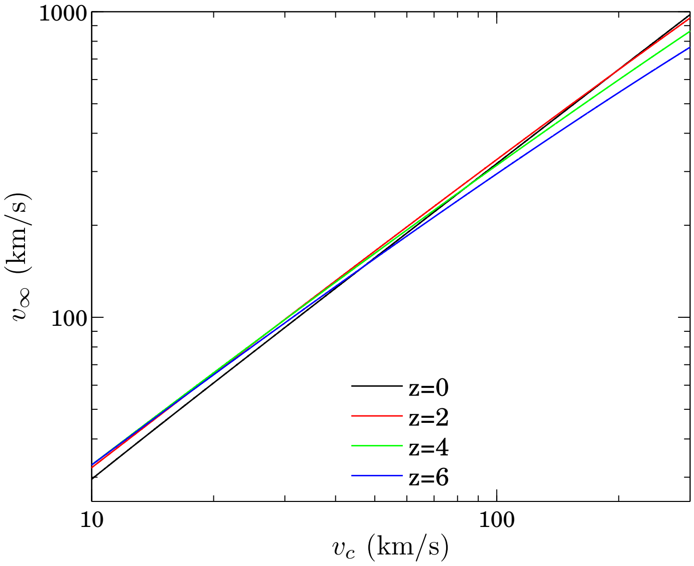

Figure 2.4: The terminal wind speed is plotted against galaxy circular speed for redshifts $z = 0, 2, 4$ and 6. We have used an average $\widetilde{\Gamma}_0 \approx 4.2$.

with redshift is expected to be small in this model, much smaller than those caused by other parameters, such as the IMF or frequency of starbursts.

2.4 Discussions

Figure 2.4 shows that dust-driven winds are likely to have a terminal speed, $v\infty \approx 3v_c$, for a combination of reasons that involve stellar physics and the relation between disc and halo parameters. It is interesting that this result coincides with observations.The strength of our approach lies in the fact that the terminal speed calculated using the Bernoulli function is independent of the streamline used by the gas, *as long as* streamlines do extend to infinity, which is our basic assumption. Below we discuss a few implications.

In the scenario of energy driven winds, the IGM is believed to be enriched by winds from dwarf galaxies, since they were numerous in the early universe (Silk et al., 1987; Nath & Trentham, 1997; Ferrara et al., 2000; Cen & Bryan, 2001; Madau et al., 2001; Aguirre et al., 2001). However, in the case of dust-driven winds, the importance of low-mass galaxies in IGM enrichment should diminish because of the correlation $v_\infty \propto v_c$. Our calculations here show that the wind speed depends strongly on the time elapsed after a starburst, or more generally on the star formation history and parameters. It is believed that the IMF is weighted towards massive stars at high redshift (Schneider & Omukai, 2010), in which case the wind speed likely increases with redshift. In this case the contribution of dwarf galaxies at high redshift may still be important.

Recent simulations for IGM enrichment including momentum driven winds have used the ansatz $v_\infty \sim 3v_c$ (Oppenheimer & Davé, 2006). It has been suggested that the momentum driven winds drive a feedback loop that results in $v_\infty \propto v_c$ (Martin, 2005; Murray et al., 2005). Our calculations show that such dust-driven winds are possible from disc galaxies certainly for a period of ~ 10 Myr after a starburst, and the outflow may continue for long time if the rate of occurrence of starbursts is large. Since the wind speed depends strongly on the value of disc Υ, which depends on the IMF (being smaller for a top-heavy IMF), the wind speed is expected to be larger for a IMF skewed towards massive stars. The implications needs to be studied with numerical simulations using modified prescriptions for the wind speed. It is possible that this put constraints on the metallicity of the wind gas. In addition, as the dust opacity is proportional to the metallicity, $\kappa \propto Z$, the existence of a threshold Γ_0 needed for the wind to reach infinity suggests that only metal-rich galaxies can enrich IGM.

We note that our calculation does not determine streamlines, without which we cannot calculate the density structure in the wind, and therefore cannot derive the mass loss rate. In the case of single scattering, the maximum mass loss rate is $\dot{M} \sim L/(v_\infty c)$ (Murray et al., 2005). This recovers the scaling that $\dot{M} \propto v_c^{-1}$ adopted by numerical simulations (Oppenheimer & Davé, 2006). Taking our results into account, the mass loss rate for a given luminosity is expected to be lower at high redshift, because of the possible rise of v_∞ with z arising from IMF evolution.

In summary, we have shown that the terminal speed (v_∞) correlates with the galaxy circular speed for radiation driven outflows from disc galaxies. We have found that, for an instantaneous starburst model, the terminal speed is $v_\infty \approx 3v_c$, which results due to the high value of disc luminosity to mass ratio. The terminal speed arises as a result of various factors such as the photon output from instantaneous burst of stars and the gravitational force of the disc, bulge and dark matter halo. We have shown that dust-driven winds from disc galaxies occur for a time-scale of ~ 10 Myr of a starburst, after which the luminosity becomes low and the radiation pressure on dust is unable to drive outflows. If the galaxy has a high rate of occurrence of starbursts, then the winds can be sustained for a long time.

Chapter 3

Simulation of Radiation Driven Wind from Disc Galaxy

Based on :
Chattopadhyay, I., Sharma, M., Nath, B. B. & Ryu, D. 2012, MNRAS, 423, 2153

Radiation pressure on dust grains is an important mechanism to drive large scale outflows. Recent theoretical modelling focuses on one dimensional calculations to determine the requirement on luminosity and possibility of such outflows from starburst galaxies (Murray et al., 2005; Sharma et al., 2011). However, the 3D structure of the outflow is yet unexplored. Also the work presented in previous chapter considers a disc with uniform surface density and uniform brightness for analytical simplicity. In reality the mass and light distribution in a disc galaxy is better represented by an exponential. In this chapter we model the outflow from an exponential disc using 2D simulations in cylindrical geometry. We explore the structure and rotation of the wind material.

Main Results

- We compute the force of radiation and gravity at a given point due to a disc with uniform and exponential distribution of mass and light in the disc plane.

- We find that for non-rotating outflow from a uniform density disc there is radial inflow of matter from the outskirts of the galaxy. The wind formed is conical in shape. The wind cone initially diverges but later its area of cross section becomes constant.

- For a disc with exponential distribution of mass and brightness, the non-rotating wind has a conical shape with half cone angle of roughly $\sim 30^{\circ}$. Compared to the case of uniform density disc, there is no significant radial inflow of gas lifted from outskirts of disc.

- We then model a rotating wind from an exponential disc. The radial inflow is now absent as the centrifugal force compensates for the inward pull of gravity. The resulting outflow is of conical shape. Apart from the central cone region there is significant mass loss from the outskirts of the disc as well. The outflow becomes steady roughly after ~ 50 Myr.

- The rotation speed of the gas in the wind cone is within 100 km s^{-1} . Thus the main wind cone is slowly rotating which is consistent with observations.

- The value of disc Eddington parameter required to drive the outflow is $\Gamma_0 \gtrsim 1.5$. This is smaller then the one found in 1D analytical calculations, which can be understood as the mass and light distribution in the disc is exponential and the wind is rotating therefore there is an additional centrifugal force which acts against gravity. Also the extent of the wind in this simulation is only 10 kpc, therefore this condition of Γ_0 is for driving outflows upto ~ 10 kpc.

3.1 Introduction

In this chapter, we study the effect of radiation pressure in driving cold and/or warm gas outflows from disc galaxies with 2D numerical simulations and explore the structure of these winds. In the previous chapter, we calculated the terminal speed of such a flow along the pole of a disc galaxy, taking into account the gravity of disc, stellar bulge and dark matter halo. We determined the minimum luminosity to drive a wind, and also found that the terminal speed is approximately $3v_c$ (where v_c is the rotation speed of the disc galaxy), consistent with observations (Rupke et al., 2005b), and the ansatz used by numerical simulations in order to explain the metal enrichment of the IGM (Oppenheimer & Davé, 2006). We investigate further the spatial structure and off-axis dynamics of a radiation driven outflow. Rotation is an additional aspect of the winds that we address in our simulation. As the wind material is lifted from a rotating disc, it likely rotates as seen in observations as well (Greve, 2004; Sofue et al., 1992; Seaquist & Clark, 2001; Westmoquette et al., 2009).

Previous simulations of galactic outflows have considered the driving force of a hot ISM energized by the effects of SNe (Tomisaka & Bregman, 1993; Suchkov et al., 1994; Mac Low & Ferrara, 1999; Strickland & Stevens, 2000; Fragile et al., 2004; Fujita et al., 2004; Cooper et al., 2008; Fujita et al., 2009). However, the details of a radiatively driven galactic outflows is yet to be studied with a simulation. In this chapter, we study the dynamics of an irradiated gas above an axisymmetric disc galaxy by using hydrodynamical simulation. Recently, Hopkins et al. (2012) have explored the relative roles of radiation and SNe heating in driving galactic outflows, and studied the effect of feedback on the star formation history of the galaxy. Our goal here is different in the sense that we focus on the structure and dynamics and the rotation of the wind. We begin with a constant density and surface brightness disc; afterwords, we implement the radial surface density and brightness profile and finally introduce rotation of the disc, in order to understand the effect of each factor in detail separately. In §3.2, we evaluate the force of radiation and gravity above the plane of a disc. In §3.3, we describe the numerical method and simulation set-up. We present our simulations and results in §3.4 and discuss our findings in §3.5.

3.2 Gravitational and radiation fields

The main driving force is radiation force and the containing force is due to gravity. We take the system to be composed of three components disc, bulge and the dark matter halo. We describe the forces due to these three constituents below. We take a thin galactic disc and a spherical bulge. All these forces are given in cylindrical coordinates because we solve the fluid equations in cylindrical geometry.

3.2.1 Gravitational field due to a disc

Consider a thin axisymmetric disc in R–ϕ plane with surface mass density $\Sigma(R)$. As derived in the Appendix F, the vertical and radial components of gravity due to the disc material at a point Q above the disc with coordinates $(R, 0, z)$, are given by

$$
\begin{aligned}
f_{disc,z} &= \int_{\phi'} \int_{R'} d\phi' \, dR' \, \frac{zG\Sigma(R') \, R'}{[R^2 + z^2 + R'^2 - 2RR' cos\phi']^{3/2}} \\
f_{disc,R} &= \int_{\phi'} \int_{R'} d\phi' \, dR' \frac{(r - R' cos\phi') \, G\Sigma(R') \, R'}{[R^2 + z^2 + R'^2 - 2RR' cos\phi']^{3/2}}
\end{aligned}
\qquad (3.1)
$$

The azimuthal coordinate of Q is taken to be zero, because of axisymmetry. The integration limit for $\phi' = 0$ to 2π.

We consider two types of disc in our simulations, one with uniform surface mass density and radius R_d, which we call UD, and another with an exponential distribution of surface mass density with a scale radius R_s and we call it ED. The surface mass density of uniform surface density disc (UD) is,

$$
\Sigma = \Sigma_0 = \text{constant} \qquad (3.2)
$$

and in the case of a disc with exponentially falling density distribution (ED)

$$
\Sigma = \tilde{\Sigma}_0 \text{exp}(-R'/R_s), \quad R_s \equiv \text{scale length}\,. \qquad (3.3)
$$

In case of UD (equation 3.2), the integration limit would be, $R' = 0$ to R_d, while for ED (equation 3.3), the limits of the integration run from $R' = 0$ to ∞. Numerically this means, we integrate up to a large number, increasing which will not change the gravitational field by any significant amount. We have normalized the Σs in such a way that the total disc mass remains same for both UD and ED. Therefore,

$$
\tilde{\Sigma}_0 = \frac{\Sigma_0}{2} \left(\frac{R_d}{R_s} \right)^2 . \qquad (3.4)
$$

In Figure 3.1, we plot the contours of gravitational field strength and its direction vectors due to a UD (left panel), and that for the ED (right panel). Interestingly, discs with same mass but different surface density distributions, produce different gravitational fields. For the UD the gravitational field is non-spherical and it is maximum at the edge of the disc. On the other hand, the field due to ED is closer to spherical configuration with the maximum

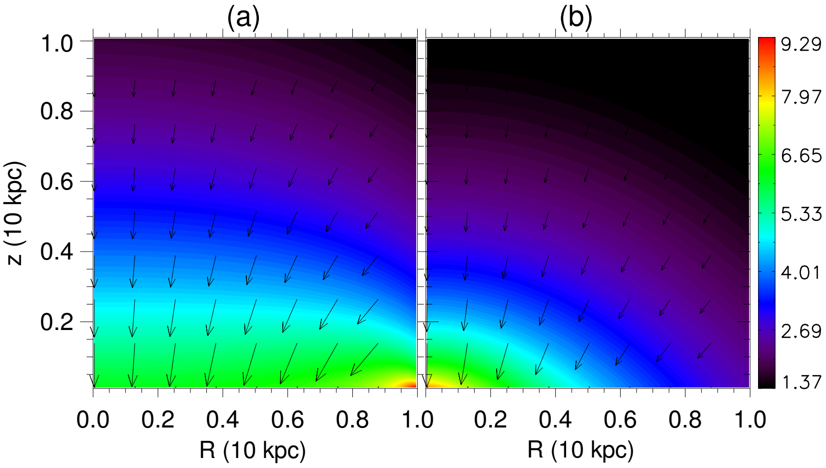

Figure 3.1: Magnitude of gravitational force of the (a) uniform disc (UD) (b) exponential disc (ED) in colours with direction in arrows. Values are in the units of $G\Sigma_0 (= 4.5 \times 10^{-9})$ dyne.

being closer to the centre of the disc and falling off outwards.

3.2.2 Bulge and the dark matter halo

We consider a bulge with a spherical mass distribution and constant density, with mass M_b and radius r_b. The radiation force due to the bulge is negligible as it mostly hosts the old stars. The gravitational force of the bulge is given by

$$f_{bulge,R} = \begin{cases} -\frac{GM_b R}{r_b^3} & \text{if } r < r_b \\ \\ -\frac{GM_b R}{r^3} & \text{otherwise} \end{cases} \tag{3.5}$$

$$f_{bulge,z} = \begin{cases} -\frac{GM_b z}{r_b^3}\,, & \text{if } r < r_b \\ \\ -\frac{GM_b z}{r^3}\,, & \text{otherwise} \end{cases} \tag{3.6}$$

where $r = \sqrt{R^2 + z^2}$.

We consider a NFW halo with a scaling with disc mass as given by Mo et al. (1998), where the total halo mass is ~ 20 times the total disc mass. The mass of an NFW halo has the following functional dependence on r,

$$M(r) = 4\pi \rho_{\text{crit}} \delta_0 r_s^3 \left[\ln\left(1 + cx\right) - \frac{cx}{1 + cx} \right] \tag{3.7}$$

where $x = \frac{r}{r_{\text{vir}}}, c = \frac{r_{\text{vir}}}{r_s}, \delta_0 = \frac{200}{3} \frac{c^3}{ln(1+c) - c/(1+c)}$. Here ρ_{crit} is the critical density of the universe at present epoch, r_s is scale radius of NFW halo and r_{vir} is the limiting radius of virialized halo within which the average density is $200\rho_{\rm crit}$. This mass distribution corresponds to the following potential,

$$\Phi_{\rm NFW} = -4\pi\rho_{\rm crit}\delta_0 r_s^3\Big[\ln\left(1+r/r_s\right)/r\Big] \tag{3.8}$$

The gravitational force due to the dark matter halo is therefore given by,

$$\begin{aligned} f_{halo,R} &= -\frac{\partial\Phi_{\rm NFW}}{\partial R} = -\frac{R\,GM(r)}{(R^2+z^2)^{3/2}}; \\ f_{halo,z} &= -\frac{\partial\Phi_{\rm NFW}}{\partial z} = -\frac{z\,GM(r)}{(R^2+z^2)^{3/2}}\,. \end{aligned} \tag{3.9}$$

The net gravitational acceleration is therefore given by

$$\begin{aligned} F_{grav,R} &= f_{disc,R} + f_{bulge,R} + f_{halo,R} = G\Sigma_0 f_{g,R}(R,z) \\ F_{grav,z} &= f_{disc,z} + f_{bulge,z} + f_{halo,z} = G\Sigma_0 f_{g,z}(R,z)\,. \end{aligned} \tag{3.10}$$

The gravitational field for both bulge and halo is spherical in nature, although, that due to the bulge maximises at r_b. However, the net gravitational field will depend on the relative strength of the three components. In Figure 3.2 (left panel), we plot the contours of total gravitational field strength due to the bulge, the halo and a UD. The non-spherical nature of the gravitational field is evident. A more interesting feature appears due to the bulge gravity. The net gravitational intensity maximizes in a spherical shell of radius $r_b(= 0.2L_{\rm ref}$, where $L_{\rm ref}$ is the unit of length in our simulation (see §3.3.1). Therefore, there is a possibility of piling up of outflowing matter at around a height $z \sim r_b$ near the axis. In the right panel of Figure 3.2, we present the contours of net gravitational field due to an exponential disc, a halo and a bulge.

3.2.3 Radiation from disc and the Eddington factor

We treat the force due to radiation pressure as it interacts with charged dust particles that are assumed to be strongly coupled to gas by Coulomb interactions and which drags the gas with it. The strength of the interaction is parameterized by the dust opacity κ.

Gravitational pull on the field point $Q(R,z)$ due to the disc point $P(R',\phi',0)$ is along the direction $\overrightarrow{QP}$ (see Appendix F). The difference in computing the radiation force arises due to the fact that one needs to account for the projection of the intensity at Q (for radiation force from more complicated disc, see Chattopadhyay (2005)). For a disc with surface brightness $I(R)$, we can find the radiation force by replacing $G\Sigma(R')$ in equation (3.1) by $I(R')\kappa/c$, and take into account the projection factor $z/\sqrt{R^2+z^2+R'^2-2RR'\cos\phi'}$. Similar to the

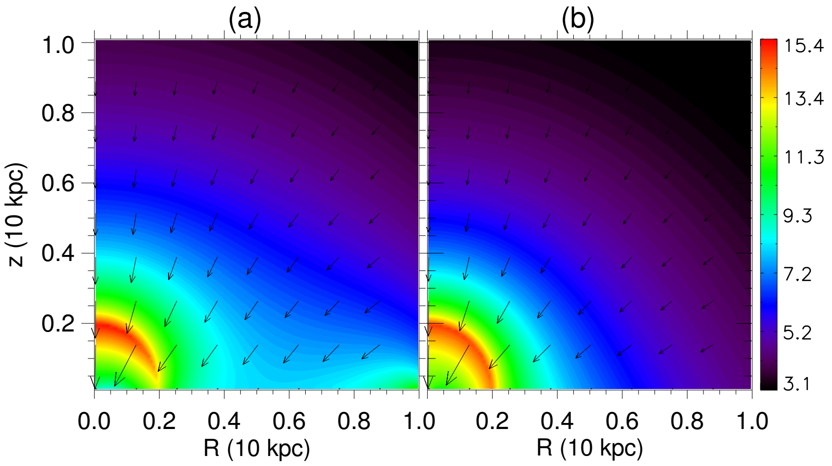

Figure 3.2: Total gravitational force due to contribution from bulge, halo and (a) uniform disc (b) exponential disc in colors with direction shown by arrows. The values are in the same units as in Figure 3.1.

disc gravity, the net radiation force $\overrightarrow{F}_{rad}$ at any point will have the radial component ($F_{rad,R}$) and the axial component ($F_{rad,z}$), which are given by,

$$\begin{aligned} F_{rad,R}(R,z) &= \frac{\kappa z}{c}\int\int \frac{d\phi' dR' I(R')(R - R'cos\phi')\, R'}{[R^2 + z^2 + R'^2 - 2rR'cos\phi']^2} \\ &= \frac{\kappa I_0}{c} f_{rad,R}(R,z) \end{aligned} \tag{3.11}$$

$$\begin{aligned} F_{rad,z}(R,z) &= \frac{\kappa z^2}{c}\int\int \frac{d\phi' dR' I(R') R'}{[R^2 + z^2 + R'^2 - 2RR'cos\phi']^2} \\ &= \frac{\kappa I_0}{c} f_{rad,z}(R,z) \end{aligned} \tag{3.12}$$

Since we have two models for disc gravity, we also consider two forms of disc surface brightness.

$$I = I_0 = \text{constant, for UD} \tag{3.13}$$

and

$$I = \tilde{I}_0 \text{exp}(-R'/R_s), \text{ for ED} \tag{3.14}$$

If the two disc types are to be compared for identical luminosity, then one finds

$$\tilde{I}_0 = \frac{I_0}{2}\left(\frac{R_d}{R_s}\right)^2 . \tag{3.15}$$

The disc Eddington factor is defined as the ratio of the radiation force and the gravitational force. In spherical geometry this factor is generally constant at each point because both

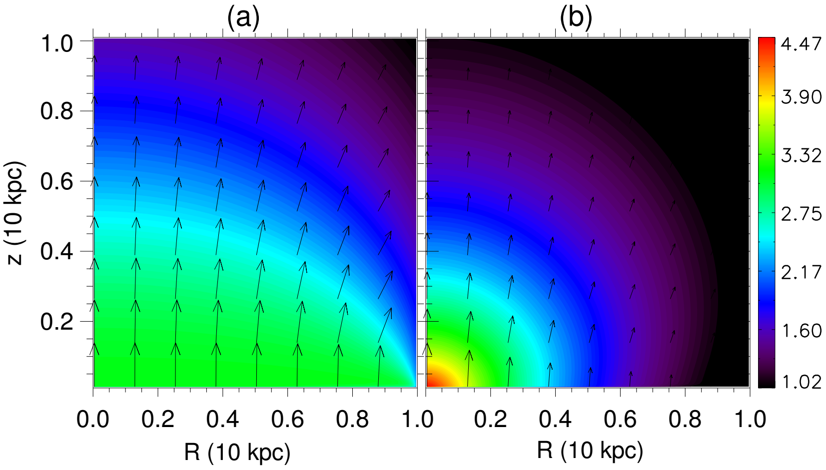

Figure 3.3: Magnitude of force due to radiation from the (a) uniform disc, (b) exponential disc for $\Gamma_0 = 0.5$, with arrows for direction.

gravity and radiation has an inverse square dependence on distance. Although in the case of a disc, the two forces have different behaviour, we can still define an Eddington parameter as $\Gamma = \frac{F_{rad}}{F_{grav}}$. In this case this parameter depends on the coordinates R, ϕ, z of the position under consideration. The Eddington factor at the centre of the disc can be given by,

$$\Gamma_0 = \frac{\kappa I}{2cG\Sigma}. \tag{3.16}$$

If $\Gamma_0 = 1$, then the radiation and gravity of the disc will cancel each other at the centre of the disc. We will parameterize our results in terms of Γ_0. Therefore, the components of the net external force due to gravity and radiation is given by

$$\begin{aligned} \mathcal{R}_R &= -F_{grav,R} + F_{rad,R} = -G\Sigma_0 \left(f_{g,R} + 2\Gamma_0 f_{rad,R} \right) \\ \mathcal{R}_z &= -F_{grav,z} + F_{rad,z} = -G\Sigma_0 \left(f_{g,z} + 2\Gamma_0 f_{rad,z} \right) \end{aligned} \tag{3.17}$$

In Figure 3.3, we plot the contours of radiative acceleration from UD, and the same from an ED. There is a significant difference between the radiation field above ED and that above the UD. While the radiation field from UD is largely vertical for small radii, but starts to diverge at the disc edge, at $R = R_d$. One can therefore expect that for high enough surface brightness (I), the wind trajectory will diverge. In case of ED, the radiation field above the inner portion of the disc is strong and decreases rapidly towards the outer disc.

3.3 Numerical method

The hydrodynamic equations have been solved in this paper by using the TVD (i.e. Total Variation Diminishing) code, which has been quite exhaustively used in cosmological and accretion disc simulations (Ryu et al., 1993; Kang et al., 1994; Ryu et al., 1995; Molteni et al., 1996) and is based on a scheme originally developed by Harten (1983). We have solved the equations in cylindrical geometry in view of the axial symmetry of the problem. This code is based on an explicit, second order accurate scheme, and is obtained by first modifying the flux function and then applying a non-oscillatory first order accurate scheme to obtain a resulting second order accuracy (see Harten (1983) and Ryu et al. (1993) for details). The equations of motion which are being solved numerically in the non-dimensional form are given by,

$$\frac{\partial \mathbf{q}}{\partial t} + \frac{1}{R}\frac{\partial (R\mathbf{F}_1)}{\partial R} + \frac{\partial \mathbf{F}_2}{\partial R} + \frac{\partial \mathbf{G}}{\partial z} = \mathbf{S} \tag{3.18}$$

where, the state vector is,

$$\mathbf{q} = \begin{pmatrix} \rho \\ \rho\, v_R \\ \rho\, v_\phi \\ \rho\, v_z \\ E \end{pmatrix}, \tag{3.19}$$

and the fluxes are,

$$\mathbf{F}_1 = \begin{pmatrix} \rho\, v_R \\ \rho\, v_R^2 \\ \rho v_R v_\phi \\ \rho v_z v_R \\ (E+p) v_R \end{pmatrix}, \quad \mathbf{F}_2 = \begin{pmatrix} 0 \\ p \\ 0 \\ 0 \\ 0 \end{pmatrix}, \quad \mathbf{G} = \begin{pmatrix} \rho v_z \\ \rho v_R v_z \\ \rho v_\phi v_z \\ \rho v_z^2 + p \\ (E+p) v_z \end{pmatrix} \tag{3.20}$$

and the source function is given by,

$$\mathbf{S} = \begin{bmatrix} 0 \\ \frac{\rho v_\phi^2}{R} - \rho\mathcal{R}_r \\ -\frac{\rho v_R v_\phi}{R} \\ -\rho\mathcal{R}_z \\ -\rho[v_R\mathcal{R}_R + v_z\mathcal{R}_z) \end{bmatrix} \tag{3.21}$$

3.3.1 Initial and boundary conditions

We do not include the disc in our simulations and only consider the effect of disc radiation and total gravity on the gas being injected from the disc. We choose the disc mass to be $M_d = 10^{11}$ $\mathrm{M}_\odot$ and assume it to be the unit of mass ($M_{\rm ref}$). We take $R_d = 10$ kpc as the unit of length ($L_{\rm ref}$), and $v_c = 200$ km s^{-1} as the unit of velocity ($v_{\rm ref}$). Therefore, the unit of time is $t_{\rm ref} = 48.8$ Myr. We introduce a normalization parameter ξ such that $GM_d/v_c^2 = \xi r_d$, which turns out to be $\xi \approx 1.08$. Hence the unit of density is $\rho_{\rm ref} = 6.77 \times 10^{-24}$g cm^{-3} ($\sim 4{\rm m_p}$ cm^{-3}). All the flow variables have been made non-dimensional by the choice of unit system mentioned above.

It is important to choose an appropriate initial condition to study the relevant physical phenomenon. We note that previous simulations of galactic outflows have considered a variety of gravitational potential and initial ISM configurations. For example, Cooper et al. (2008) considered the potential of a spherical stellar bulge and a flat disc potential, but no dark matter halo, and the initial gas distribution stratified in z-direction with an effective sound speed that is ~ 5 times the normal gas sound speed. Suchkov et al. (1994) considered the potential of a spherical bulge and a dark matter halo and an initial gas configuration that is spherically stratified. Fragile et al. (2004) considered a spherical halo and a z-stratified gas distribution. In a recent simulation of outflows driven by SNe from disc galaxies, Dubois & Teyssier (2008) found that the outflowing gas has to contend with infalling material from halo, which inhibits the outflow for a few Gyr. Fujita et al. (2004) also studied outflows from pre-formed disc galaxies in the presence of a cosmological infall of matter.

We choose a z-stratified gas to fill the simulation box, with a scale height of 100 pc. For the M$_2$ and M$_3$ case (of exponential disc), we also assume a radial profile for the initial gas, with a scale length of 5 kpc. For the M$_3$ case, we further assume this gas to rotate with v_ϕ decreasing with a scale height of 5 kpc. These values are consistent with the observations of the warm neutral gas ($T \sim 10^4$ K) in Milky Way (Dickey & Lockman, 1990; Savage et al., 1997). We note that although the scale height for the warm neutral gas in our Galaxy is ~ 400 pc at the solar vicinity, this is expected to be smaller in the central region because of strong gravity due to bulge. The density of the gas just above the disc is assumed to be 0.1 particles /cc (0.025 in simulation units). Furthermore, the adiabatic index of the gas is $5/3$ and the gas is assumed initially to be at the same temperature corresponding to an initial sound speed $c_{s,ini} = 0.1 v_{\rm ref}$, a value which is consistent with the values in our Galaxy for the warm ionized gas with sound speed ~ 18 km s^{-1}.

Our computation domain is $R_d \times R_d$ in the $R - z$ plane, with a resolution 512×512 cells. The size of individual computational cell is ~ 20 pc. We have imposed reflective boundary condition around the axis and zero rotational velocity on the axis. Continuous boundary conditions are imposed at $R = R_d$ and $z = R_d$. The lower boundary is slightly above the galactic disc with an offset $z_0 = 0.01$. We impose fixed boundary condition at lower z boundary. The velocity of the injected matter is $v_z(R, z_0) = v_0 = 10^{-5} v_{\rm ref}$, and its

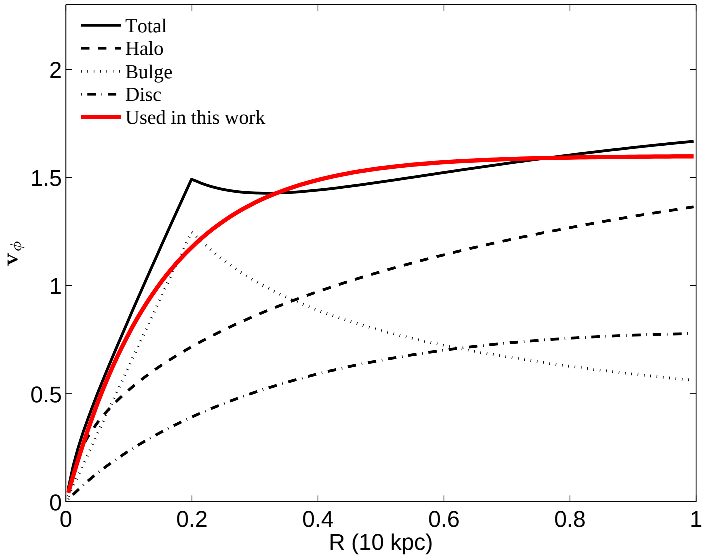

Figure 3.4: Rotation curves corresponding to the gravitational fields of an exponential disc, bulge and halo are shown here in the units of $v_{\rm ref}[= 200$ km s$^{-1}]$, along with the total rotation curve. The approximation used in our simulation is shown by thick red line.

density is given by,

$$\begin{aligned} \rho(R, z_0) &= \rho_{z_0}, \quad \text{for UD} \\ &= \rho_{z_0}\text{exp}\left(-\frac{R}{R_s}\right), \quad \text{for ED}\,. \end{aligned} \tag{3.22}$$

The density of the injected matter at the base $\rho_{z_0} = 0.025$ in simulation units (corresponds to $0.1\,\rm m_p/cc$).

For the case of exponential disc with rotation (M$_3$), we assume for the injected matter to have an angular momentum corresponding to an equilibrium rotation profile. We show in Figure 3.4 the rotation curves at $z = 0$ for all components (disc, bulge and halo) separately and the total rotation curve. We use the following approximation (shown by thick red line in Figure 3.4) which matches the total rotation curve,

$$v_\phi(R, z_0) = 1.6\, v_c\, [1 - \text{exp}(-R/0.15R_d)]\,. \tag{3.23}$$

We assume a bulge of mass $M_b = 0.1 M_{\rm ref}$ and radius $r_b = 0.2 L_{\rm ref}$. The scale radius for NFW halo (r_s) is determined for a halo mass $M_h = 20 M_d$, as prescribed by Mo et al. (1998). The corresponding disc scale radius is found to be $R_s \sim 5.8$ kpc, again using Mo et al. (1998) prescriptions. Therefore, we set the disc scale length for the ED case to be $R_s \sim 0.58 L_{\rm ref}$.

The above initial conditions have been chosen to satisfy the following requirements in order to sustain a radiatively driven wind as simulated here.

Table 3.1: Models.

Model name	Γ_0	v_ϕ	Disc type
M_1	2.0	0.0	UD
M_2	2.0	0.0	ED
M_3	2.0	1.0	ED

1. The strong coupling between dust grains and gas particles require that there are of order $\sim \mathrm{m_d}/\mathrm{m_p}$ number of collisions between protons and dust grains of mass $\mathrm{m_d} \sim 10^{-14}$ g, for size $a \sim 0.1\,\mu$m with density $\sim$ 3g cm^{-3}. To ensure sufficient number of collisions, the number density of gas particles should be $n \geq \frac{\mathrm{m_d}}{\mathrm{m_p}} \frac{1}{\pi a^2} \frac{1}{L_{\mathrm{ref}}} \sim 10^{-3}$ cm^{-3}, for $L_{\mathrm{ref}} = 10$ kpc.

2. The time scale for radiative cooling of the gas, assumed to be at $T \sim 10^4$ K, is $t_{cool} \sim \frac{1.5kT}{n\Lambda}$, where $\Lambda \sim 10^{-23}$ erg cm^3 s^{-1} (Sutherland & Dopita 1993; Table 6) for solar metallicity. The typical density filling up the wind cone in the realistic case (M_3) is $\sim 10^{-3}$–10^{-4} cm^{-3}, which gives $t_{cool} \sim 8$–80 Myr and the dynamical time scale of the wind is $t_{\mathrm{ref}} \sim 50$ Myr. Hence, radiative cooling seems marginally important and will be addressed in future. In this regard, we also note that the growth rate of thermal instability is likely suppressed for diverging galactic wind (Ferrara & Einaudi, 1992).

3. Radiative transfer effects are negligible since the total opacity along a vertical column of length L_{ref} is $\kappa(n\mathrm{m_p})L_{\mathrm{ref}} \sim 0.003$, for $n \sim 10^{-3}$ cm^{-3} and $\kappa \sim 100$ cm^2 g^{-1}.

4. The mediation of the radiation force by dust grains also implies that the gas cannot be too hot for the dust grains to be sputtered. The sputtering radius of grains embedded in even in a hot gas of temperature T$\sim 10^5$ K is $\sim 0.05(n/0.1\,/\mathrm{cc})\,\mu$m in a time scale of 100 Myr (Tielens et al., 1994), and this effect is not important for the temperature and density considered here.

3.3.2 Simulation set up

We present three models with parameters listed in the Table 3.1. The initial condition for all the models are described in §3.3.1. The boundary condition is essentially the same, except that the mass flux into the computational domain from the lower z boundary depends on the type of disc. As has been mentioned in §3.3.1, we keep the velocity of injected matter very low, $v_z(r, z_0) = v_{z,ini} = 10^{-5} v_{\mathrm{ref}}$, so that it does not affect the dynamics. The three models have been constructed by a combination of different values of three parameters Γ_0, v_ϕ and

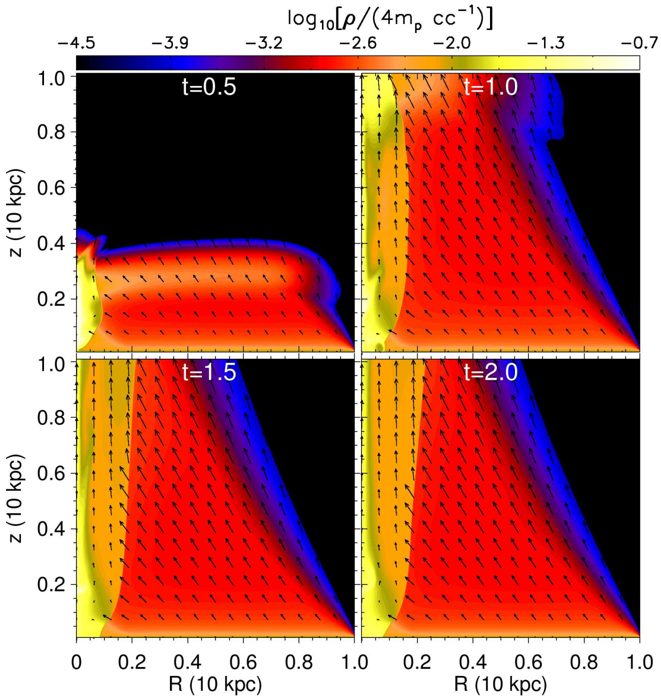

Figure 3.5: M_1 : Logarithmic density contours for radiation driven wind from UD for four snapshots running up to $t = 98$ Myr, with velocity vectors shown with arrows. Densities are colour-coded according to the computational unit of density, 6.7×10^{-24} g cm^{-3} $\approx 4\mathrm{m_p}$ cm^{-3}.

the distribution of the density in the disc. Model M_3 has been run for different values of Γ_0, to ascertain the effect of radiation.

3.4 Results

In Figure 3.5, we present the model M_1 for a constant surface density disc (UD). The density contour and the velocity vectors for the wind are shown in four snapshots in Figure (3.5) upto a time $t = 98$ Myr (corresponding to $t = 2$ in computational time units). There are a few aspects of the gaseous flow that we should note here. Firstly, the disc and the outflowing gas in this case has no rotation ($v_\phi = 0$). In the absence of the centrifugal force due to rotation which might have reduced the radial gravitational force, there is a net radial force driving the gas inward. At the same time, the radiation force, here characterised by $\Gamma_0 = 2$, propels the gas upward (the radial component of radiation being weak). The net result after a few Myr is that the gas in the region near the pole moves in the positive z direction, and there is a density enhancement inside a cone around the pole, away from which the density and velocities decrease.

Also, because of the strong gravity of the bulge, the gas tends to get trapped inside the bulge region, and even the gas at larger r tends to get dragged towards the axis. This region

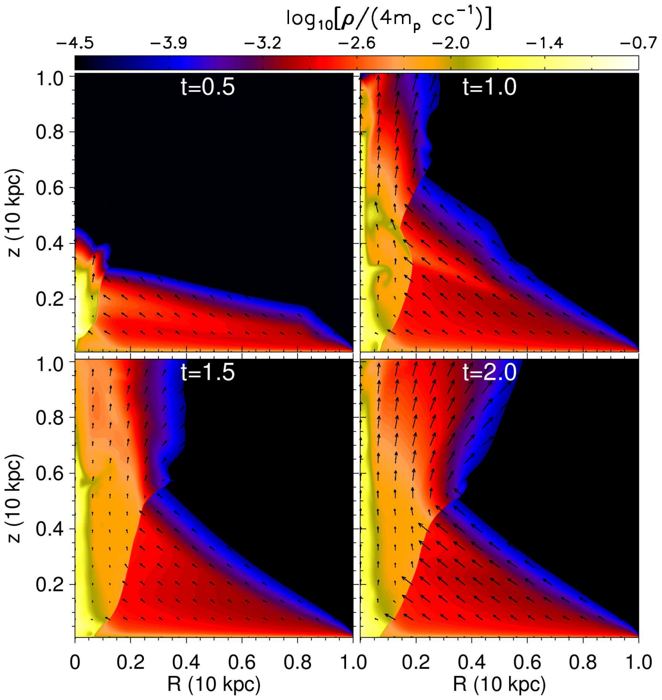

Figure 3.6: M_2 : Logarithmic density contours for radiation driven wind from ED for four snapshots running up to $t = 98$ Myr, with velocity vectors shown with arrows.

puffs due to accumulation of matter. Ultimately the radiative force drives matter outwards in the form of a plume.

Next, we change the disc mass distribution and simulate the case of wind driven out of an exponential disc (ED). We show the results in Figure 3.6. Since both gravity and radiation forces in this case of exponential disc are quasi-spherical in nature, therefore in the final snapshot the flow appears to follow almost radial streamlines. Although in the vicinity of the disc, the injected matter still falls towards the axis, but this is not seen at large height as was seen in the previous case of M_1. This makes the wind cone of rising gas more diverging than in the case of UD (M_1).

3.4.1 Rotating wind from exponential disc

The direction of the fluid flow in M_1 and M_2 is by and large towards the axis at low height, and this flow is mitigated in the presence of rotation in the disc and injected gas. In the next model M_3, we consider rotating matter being injected into the computational domain and which follows a v_ϕ distribution given by equation (3.23). This is reasonable to assume since the disc from which the wind is supposed to blow, is itself rotating. In M_3, we simulate rotating gas being injected above a ED and being driven by a radiation force of $\Gamma_0 = 2$. We present nine snapshots of the M_3 case in Figure 3.7.

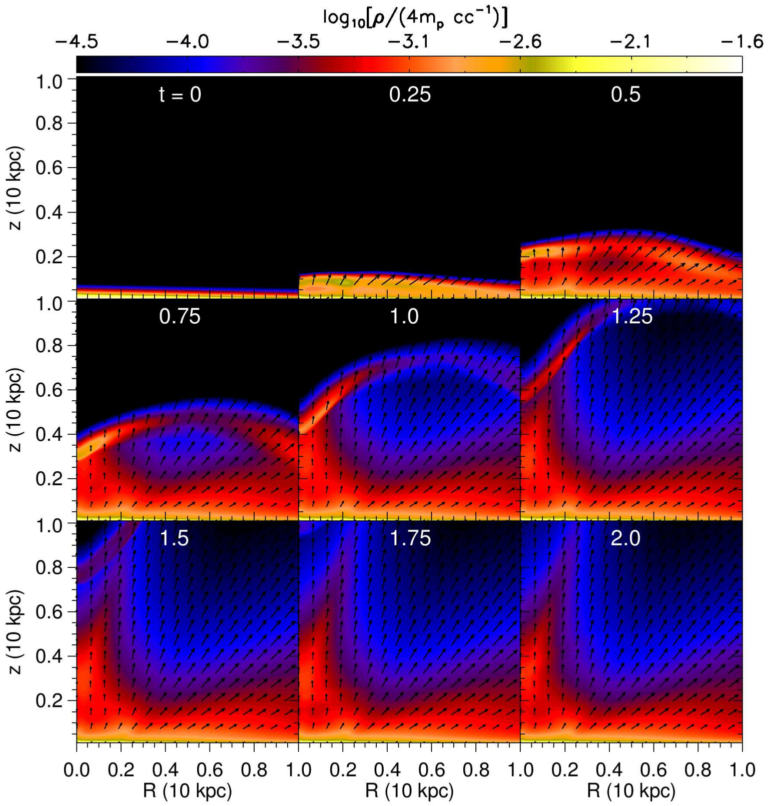

Figure 3.7: M_3: Contours of $\log_{10}(\rho)$ and **v**-field of radiation driven wind with $\Gamma_0 = 2.0$ from an ED. $t = 2$ corresponds to 98 Myr.

The first six snapshots of Figure 3.7 show the essential dynamics of the outflowing gas. The fast rotating matter from the outer disc is driven outward because the radial gravity component is overcome by rotation. Near the central region, rotation is small and also the radial force components are small. Therefore the gas is mostly driven vertically. The injected gas reaches a vertical height of ~ 5 kpc in a time scale of ~ 37 Myr ($t = 0.75$). The flow reaches a steady state after ~ 60 Myr ($t = 1.25$). In the steady state we find a rotating and mildly divergent wind.

We show the azimuthal velocity contours in Figure 3.8 in colour for the fully developed wind (last snapshot in M_3), and superpose on it the contour lines of ρ. The density contours clearly show a conical structure for outflowing gas. The rotation speed of the gas peaks at the periphery of the cone, and is roughly within 100 km s^{-1}. Compared to the disc rotation speed, the rotation speed of the wind region is somewhat smaller. In other words, we find the wind mostly consisting of low-angular momentum gas lifted from the disc. We plot the velocity of gas close to the axis in Figure 3.9 for different times in this model (M_3), considering $v(0,z) \sim v_z(0^+, z)$. The velocity profile in the snapshots at earlier time fluctuates at different height, but becomes steady after $t \geq 1.5$, as does the density profile. We have run this

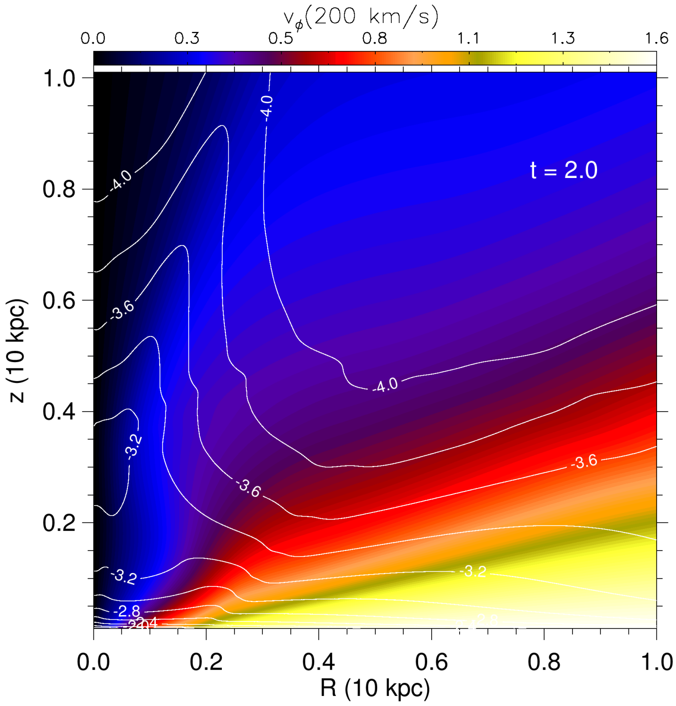

Figure 3.8: The rotation velocity v_ϕ for the case M$_3$ at a time of 98 Myr is shown in colours. Contour lines of $\log_{10}(\rho)$ are plotted over it.

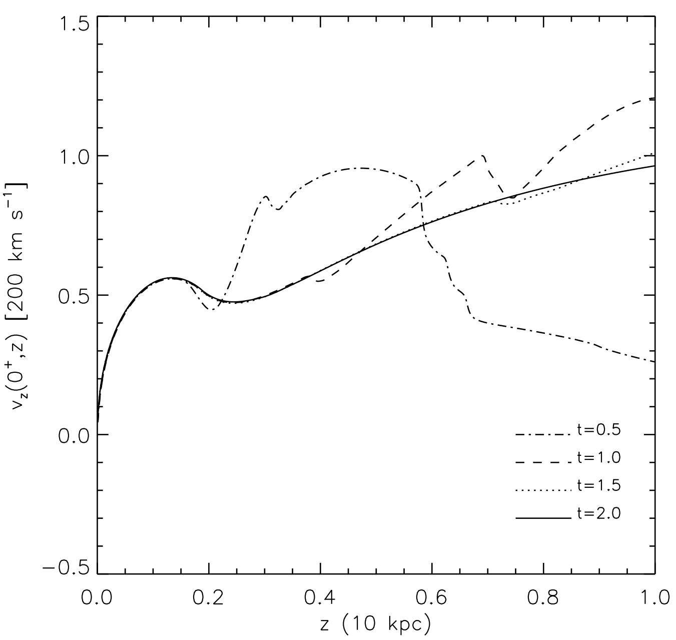

Figure 3.9: The axial velocity $v_z(0^+, z)$ with z at different time steps for the model M$_3$. $t = 2.0$ corresponds to a time of 98 Myr.

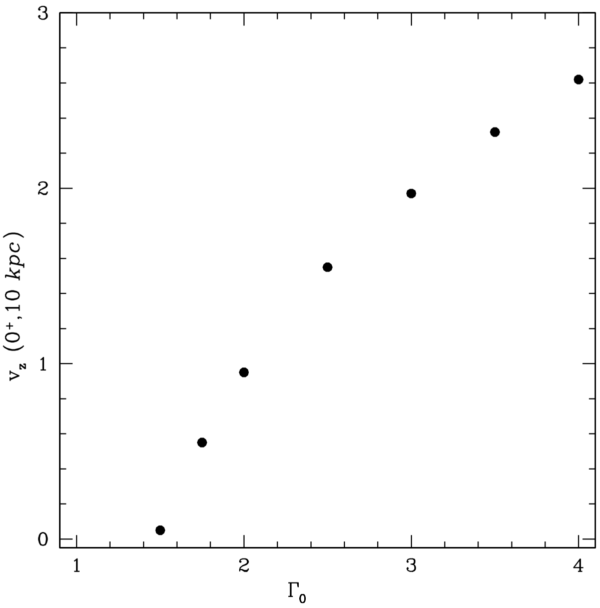

Figure 3.10: The axial velocity $v_z(0^+, 10\ \mathrm{kpc})$ in simulation units $v_{\mathrm{ref}} = 200$ km s^{-1} with Γ_0, at a time $t \sim 10$ Myr.

particular case of ED with rotation (model M_3) for different values of Γ_0. In order to illustrate the results of these runs, we plot the z-component of velocity ($v_z(0^+, 10\,\mathrm{kpc})$) at 10 kpc and at simulation time, $t = 2$ as a function of Γ_0 in Figure 3.10. We find that significant wind velocities are obtained for $\Gamma_0 \gtrsim 1.5$ and wind velocities appear to rise linearly with Γ_0 after this critical value is achieved. In the previous chapter, using 1D analytical calculation, we found this critical value to be $\Gamma_0 \approx 3$ for a constant density disc and wind launched above the bulge. For the realistic case of an exponential disc in the present simulation, we note that the critical Γ_0 is smaller, which is likely because of the fact that scale of the winds is limited by box size and also there is an additional centrifugal force due to rotation. The important point is that the critical Γ_0 is not unity. This is because the parameter Γ_0 is not a true Eddington parameter since it is defined in terms of disc gravity and radiation, whereas halo and bulge also contribute to gravity.

3.5 Discussions

Our simulation differs from earlier works (e.g. Suchkov et al., 1994) mainly in that we specifically target warm outflows and the driving force is radiation pressure. Most of the previous simulations of galactic wind have used energy injected from supernovae blasts as a driving force. However, with the ideas presented in Murray et al. (2005), which worked out the case of radiation pressure in a spherical symmetric set-up, it becomes important to study the physics of this model in an axisymmetric set up, as has been done analytically by Sharma et al. (2011). Also we have tried to capture all features of a typical disc galaxy like a bulge and a dark matter halo, and a rotating disc. Recent analytical works (Sharma et al., 2011) and simulations (Hopkins et al., 2012) have shown that outflows from massive galaxies ($M_h \geq 10^{12}$ $\mathrm{M}_\odot$) have different characteristics than those from low mass galaxies. Outflows from massive galaxies are mostly driven by radiation pressure and the fraction of cold gas in the halos of massive galaxies is large (van de Voort & Schaye, 2012). Our simulations presented here addresses these outflows in particular.

We have parameterized our simulation runs with the disc Eddington factor Γ_0, and it is important to know the corresponding luminosity for a typical disc galaxy, or the equivalent star formation rate. For a typical opacity of a dust and gas mixture ($\kappa \sim 200$ cm^2 g^{-1}) (Draine, 2011), the corresponding mass-to-light ratio requirement for $\Gamma_0 \gtrsim 1.5$ is that $M/L \leq 0.03$. In the previous chapter we have shown that for the case of instantaneous star formation, large value of Γ_0, is possible for a period of ~ 10 Myr after the starburst. However for a continuous star formation, which is more realistic for disc galaxies, Sharma & Nath (2012) found that only massive ultra luminous infrared galaxies (ULIRGs), with star formation rate larger than ~ 100 $\mathrm{M}_\odot$ yr^{-1}, are suitable candidates for such large values of Γ_0, and for radiatively driven winds.

The results presented in the previous sections show that the outflowing gas within the central region of a few kpc tends to stay close to the pole, and does not move outwards because of its low angular momentum. This makes the outflow somewhat collimated. Although outflows driven by SN heated hot wind also produce a conical structure (e.g. Fragile et al., 2004) emanating from a breakout point of the SN remnants, there is a qualitative difference between this case and that of radiatively driven winds as presented in our simulations. While it is the pressure of the hot gas that expands gradually as it comes out of a stratified atmosphere, in the case of a radiation driven wind, it is the combination of mostly the lack of rotation and almost vertical radiation force in the central region that produce the collimation effect. We also note that the conical structure of rotation in the outflowing gas is similar to the case of outflow in M82 (Greve, 2004), where one observes a diverging and rotating periphery of conical outflow.

From our results of the exponential and rotating disc model, we find the wind comprising of low-angular momentum gas lifted from the disc. It is interesting to note that recent simulations of supernovae driven winds have also claimed a similar result (Governato et al., 2010). Such loss of low angular momentum gas from the disc may have important implication for the formation and evolution of the bulge, since the bulge population is deficient in stars with low specific angular momentum. Binney et al. (2001) have speculated that outflows from disc that preferentially removes low angular momentum material may resolve some discrepancies between observed properties of disc and results of numerical simulations.

As a caveat, we should finally note that the scope and predictions of our simulation is limited by the simple model of disc radiation adopted here. In reality, radiation from discs is likely to be confined in the vicinity of star clusters, and not spread throughout the disc as we have assumed here. This is likely to increase the efficacy of radiation pressure, but which is not possible within the scope of an axisymmetric simulation.

In summary, we have presented the results of hydrodynamical (Eulerian) simulations of radiation driven winds from disc galaxies. After studying the cases of winds from a constant surface density disc and exponential disc without rotation, we have studied a rotating outflow originating from an exponential disc with rotation. We find that the outflow speed increases rapidly with the disc Eddington parameter $\Gamma_0 = \kappa I/(2cG\Sigma)$. The density structure of the outflow has a conical appearance, and most of the outflowing gas consists of low angular momentum gas.

Chapter 4

The Roles of Radiation and Ram Pressure in Driving Galactic Winds

Based on:
Sharma, M. & Nath, B. B. 2012, ApJ, 750, 55
Uhlig, M., Pfrommer, C., Sharma, M., Nath, B. B., Enßlin, T. A. & Springel, V. 2012, MNRAS, 423, 2374

We found in the previous chapters that the dynamics of the cold phase is better explained by radiation driving if the luminosity is sufficient. Whether a disc with continuous star formation is able to generate large enough luminosity to drive the outflow is a question worth exploring. The cold phase of the outflows is clumpy in nature. Cold clouds are generally embedded in a hot phase of the outflow which is believed to be moving with high velocities ($\gtrsim 500$ km/s) as inferred from X-ray temperatures. The hot phase can exert ram pressure force on the cold clouds and may thus act as an important driving agent. One should take into account the ram pressure force as well in modelling the dynamics of cold phase. in this chapter, we solve for the ballistic motion of a cold clump along the pole of disc galaxy, driven by a combined action of ram pressure and radiation pressure.

Main Results

- We find that initially the radiation pushes the cloud to a few kpc where the surrounding hot wind coming from below is dilute enough due to geometrical divergence so that the cloud crushing time is increased. Therefore the cold clouds can easily survive.
- We find that the driving force due to ram pressure is a function of SFR and the radiation force is a function of both the circular speed (v_c) and the SFR. The containing force of gravity is a function of galactic circular speed. Therefore v_c and SFR are the two free parameters of this problem. Hence we solve for cloud dynamics in the parameter space of v_c and SFR.
- We find that the criteria for galaxies to harbour outflows at the scales of ~ 20 kpc is given by,
$$\mathrm{SFR}^{3/4}_{10\ \mathrm{M_\odot/yr}}\, v^{-2}_{c,140\ \mathrm{km/s}} > 1 \tag{4.1}$$
- When the above criteria is satisfied, the wind speed (v_w) in units of galaxy circular speed (v_c) obeys the following scaling,
$$\frac{v_w}{v_c} \sim 10^{0.7} \left[\frac{\mathrm{SFR}}{50\,\mathrm{M_\odot/yr}}\right]^{0.4} \left[\frac{v_c}{120\,\mathrm{km/s}}\right]^{-1.25} . \tag{4.2}$$
- We have shown that the ram and radiation pressure driven outflows at the scales of ~ 20 kpc should occur only for galaxies which have star formation surface density, $\Sigma_{\mathrm{SFR}} \gtrsim 10^{-1}$ M$_\odot$ yr^{-1} kpc^{-2} .
- We find that there may be outflows even in galaxies with $\Sigma_{\mathrm{SFR}} < 10^{-1}$ M$_\odot$ yr^{-1} kpc^{-2}, however, a different mechanism may be at work in such situations. One such mechanism is the cosmic ray streaming which can cause outflows even in the faint dwarfs. We refer the reader to Appendix G of this thesis where we explore cosmic ray driven winds.

4.1 Introduction

In the previous chapters we explored the outflows driven by radiation pressure on dust grains. We derived that a large value ($\sim 10^2$) of luminosity-to-mass ratio is required in order to have escaping outflows. Such a large value may be possible in some cases as we discussed in chapter 1. For normal galaxies undergoing star formation in continuous manner, the SFR required to generate high luminosities is ~ 100 M$_\odot$ yr^{-1}. Another aspect is the clumpiness of the cold phase of the outflow under discussion here. Owing to the clumpy nature of the gas one may use ballistic type calculation to study the dynamics of gas (e.g. Murray et al., 2011).

In the standard SNe/starburst driven wind scenario, the cold clouds are thought to be entrained in the hot phase of flow via ram pressure (e.g. Heckman et al., 2000). However, the recent calculations based on radiation pressure ignore the ram pressure as a driving mechanism. If one carefully compares the ram pressure driving and the radiation pressure driving, both mechanisms have limitations. In the case of ram pressure, although the hot gas provides the momentum to cold clouds but, it can also disrupt the clouds via shocks and instabilities and, as a result, the cloud may not survive long enough (e.g. Marcolini et al., 2005), which is quite contrary to observations in which the cold clumps are seen upto heights of ~ 10 kpc. On the other hand, in case of radiation driving, as we mentioned above, the luminosities required are quite large, which may be available only for short periods (~ 10 Myr). In the face of the two processes (ram pressure and radiation pressure) leading to outflows, one wonders if both processes contribute equally, or if there are regimes in which one of these two processes dominate over the other.

In this chapter we address these questions and study the dynamics of the wind as a result of an interplay between the ram pressure due to hot wind and the radiation force due to a star-forming disc, whose photon output is inferred using STRABURST99 following the continuous star formation model. In §4.2 we discuss the role of radiation pressure in prolonging the lifetime of clouds and set up the equations for the dynamics of the cold gas. In §4.3 we solve for the velocity of clouds as a function of height, z. We find the terminal speed for a range in SFR and galaxy circular speed (v_c) and compare our results with observations. We discuss our findings in §4.4.

4.2 Gaseous outflows with ram and radiation pressure

We consider the dynamics of cold clouds ($T \lesssim 10^4$ K) embedded in hot gas, in which the hot gas component exerts a drag force due to ram pressure. We also assume that dust grains in the cold clouds are strongly coupled to the gas, and therefore the dynamics of these clouds is also influenced by radiation pressure.

To start with, we discuss the issue of the survival of clouds. Observations show that clouds can be present upto vertical distances of several kpc from the galaxy centre. However, if they are acted upon by the ram pressure of the hot wind right from the beginning where the clouds start their journey, then they can get disrupted via the shocks and effects of the hot wind. The shock disruption time scale is given by $\tau_{\rm dis} = \frac{R_c}{v_h}\sqrt{\frac{\rho_c}{\rho_h}}$, where R_c is the cloud radius, ρ_c is its density. Also, ρ_h and v_h are the density and velocity of the hot wind respectively. If we consider a density contrast of almost unity at the base of the wind, then the cloud crushing time scale is of the order of shock passage time scale (R_c/v_h), which is roughly a Myr and hence small. Therefore, the cloud should not survive long enough if it is acted upon by the ram pressure right from the base. Simulations of clumps embedded in hot dense flow also show that the survival of the clumps is very difficult (Marcolini et al., 2005) due to a combination of disruption mechanisms such as impact shocks and Kelvin-Helmholtz instability. However, observations show that the cold clumps are present upto large distances.

Radiation pressure driving in the initial stages of cloud motion can provide a solution to this mystery (e.g. Murray et al., 2011). Let us think of a scenario in which the clouds are lifted to a significant distance ($\sim$ kpc) before the hot wind comes into action. At these heights the hot wind would be diluted because of geometrical divergence. Therefore, when the hot wind impacts the cloud the density contrast between the cloud and surrounding can be as large as 10^2, and hence the crushing time scale is also very large (~ 10 Myr) and the cloud can survive easily. To elaborate on this, let us do a 'Gedankenexperiment'. As soon as some region in galaxy undergoes a strong burst of star formation the radiation is emitted first, which drives a surrounding shell of gas. This shell while erupting out of disc will fragment to form the clumps. In case of radiation driving mediated by dust grains these clumps easily would have travelled to the distance of roughly a kpc in 3–4 Myr. This is typically the time when the first SNe would blast, which will launch the hot flow from below. Thus when the ram pressure of the hot wind will finally come into picture, the cold cloud would already be situated at a distance of $\sim$ kpc. At this moment the problem becomes well defined. The cloud survival is no more a problem and also the clouds are high enough so that their dynamics is influenced by radiation from entire disc, the global gravitational force of galaxy and the ram pressure from a hot superwind present at kpc scales. We can then write the following equation for the dynamics of the cold cloud ($P_c = M_c v$), see Figure 4.1,

$$\frac{dP_c}{dt} = M_c\frac{dv}{dt} = F_{ram} + F_{rad} - F_{grav} \tag{4.3}$$

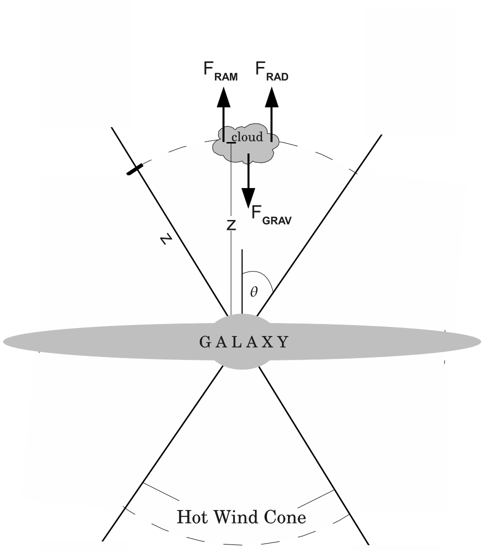

Figure 4.1: A schematic diagram for the motion of a cold cloud embedded in a cone of hot flow and acted upon by forces of radiation and gravity from the parent galaxy. Cloud is at a height z. The total mass loss in hot flow, $\dot{M}_{hot}$ = 2 $\rho_h v_h A$, where A is the area at the top of conical patch, and a factor of 2 for two-sided mass loss. For a half-cone angle of θ the area $A = z^2 \int_0^{2\pi} \int_0^{\theta} \sin(\theta')\mathrm{d}\theta' d\phi$.

where M_c is the mass of the cloud and v is its velocity in z direction. F_{ram} represents the force exerted by the hot wind via ram pressure in g cm s^{-2}. F_{rad} is the force due to radiation on dust grains and F_{grav} is the gravitational force.

We first discuss the role of ram pressure on the motion of cold blobs of gas dragged in it, following the model of Strel'Nitskii & Sunyaev (1973). In this scenario, the hot gas observed in X-rays and which is thought to provide the ram pressure, has temperatures in the range 0.5–1 keV (Heckman, 2002; Martin, 2005), which correspond to the isothermal sound speed $c_s \sim 300$–400 km/s. Current X-ray instruments can not detect the speed of this hot and tenuous material and hence the kinematics of this hot phase is poorly constrained. If we assume it as an adiabatic wind passing through a sonic point, then $v_h^2 \sim \alpha c_s^2$, where $\alpha = 2.5$–5 (Efstathiou, 2000), which gives $v_h \sim 1.2$–$2.2\, c_s$. In this chapter, we take $v_h \sim 800$ km s^{-1}, which corresponds to $v_h \sim 2c_s$ and $T_X \sim 1$ keV.

Consider then the hot gas flow (with density ρ_h and velocity v_h), emerging through a cone. Mass loss in a hot wind is given by the following expression (see figure 4.1),

$$\dot{M}_{hot} = 2\rho_h v_h z^2 \int_0^{2\pi} \int_0^{\theta} \sin(\theta') d\theta' d\phi \tag{4.4}$$

Observations indicate conical angles for hot wind in the range $2\theta \sim 10°$–$100°$ (Veilleux et al., 2005; Lehnert & Heckman, 1996). We consider a mass loss rate of $\dot{M}_{hot} \approx (\pi/2) z^2 \rho_h v_h$, which roughly corresponds to half-cone angle $\theta \sim 30°$. The momentum injection rate is

$\dot{p}_h = \dot{M}_{hot} v_h$, so we can write

$$\rho_h v_h^2 = \frac{\dot{p}_h}{\pi z^2/2} \tag{4.5}$$

The force exerted by the ram pressure on a cold cloud of mass M_c and cross-section A_c is given by

$$\begin{aligned} F_{ram} \quad &= \frac{1}{2} C_D A_c \rho_h (v_h - v)^2 \, \mathcal{H}(v_h - v) \\ &= \frac{C_D A_c}{2} \rho_h v_h^2 \left(1 - \frac{v}{v_h}\right)^2 \mathcal{H}(v_h - v) \end{aligned} \tag{4.6}$$

Here $\mathcal{H}(v_h - v)$ is the step function whose value is 1 for $v < v_h$ and 0 otherwise. $C_D \sim 0.5$ is the drag coefficient. For the cloud, one can write $\frac{M_c}{A_c} = \mu m_p N_H$ where N$_H$ is the column density and μ is the mean molecular weight. Also the momentum injection rate $\dot{p}_h \approx \left[5 \times 10^{33} \left(\frac{\text{SFR}}{1\,\text{M}_\odot/\text{yr}}\right)\right]$ dyne in a starburst (Leitherer et al., 1999). Using these and substituting eqn.(4.5) in eqn.(4.6) we get,

$$\frac{F_{ram}}{M_c} = \frac{[5 \times 10^{33} \, (\frac{\text{SFR}}{\text{M}_\odot/\text{yr}})]\text{dyne}}{4 \, N_H \, \mu m_p \, (\pi z^2/2)} \left(1 - \frac{v}{v_h}\right)^2 \mathcal{H}(v_h - v) \tag{4.7}$$

4.2.1 Disc, bulge and halo

Next we consider the forces due to a thin galactic disc. We will use f for force per unit mass ($f = \frac{F}{M_c}$). In cylindrical geometry, the force of gravitation $f_{g,d}(z)$, and that due to radiation $f_{r,d}(z)$, along the pole of a disc of radius R_d, with constant surface mass density (Σ) and surface brightness (I) are given by,

$$f_{g,d} = 2\pi G \Sigma \int^{R_d} \frac{z R dR}{(R^2 + z^2)^{3/2}} \, , f_{r,d} = \frac{2\pi \kappa I}{c} \int^{R_d} \frac{z^2 R dR}{(R^2 + z^2)^2} \, , \tag{4.8}$$

where κ is the average opacity of a dust and gas mixture. The ratio of these forces, the disc Eddington ratio, increases with the height z, beginning with a value of $\Gamma_0 = \frac{\kappa I}{2cG\Sigma}$ at the disc centre at $z = 0$. Since $\frac{I}{\Sigma} \propto \frac{L}{M_d}$, where M$_d$ is the disc mass, we can express Γ_0 in terms of the SFR by calculating the luminosity L of a galaxy in any desired band for a certain SFR using the code STARBURST99. The luminosity in this case is proportional to SFR, therefore if L_1 is the luminosity at 1 Gyr for an SFR of 1 M$_\odot$ yr^{-1} then we can write Γ_0 as,

$$\Gamma_0 = \frac{\kappa}{2cG} \frac{L_1 \times \frac{\text{SFR}}{\text{M}_\odot/\text{yr}}}{M_d} \tag{4.9}$$

The opacity (κ) depends on the situation whether the clouds are optically thick or thin to the UV radiation. Mean opacity for gas mixed with dust corresponding to a colour temperature

~ 9000 K is $\kappa \approx 200$ cm^2 g^{-1} in the U band (Figure 1b, Draine (2011)). This opacity can be used if the clouds are optically thin. For large clouds with size, $\ell_c \sim 1$ kpc and with density, $\rho_c \sim 1$ $\mathrm{m_p}$ cc^{-1}, the optical depth would be $\tau \sim 1$, which means the cloud can be marginally optically thick. In this case, the opacity would be given by $\kappa \to A_c/M_c \approx (\rho_c \ell_c)^{-1}$, which comes out to be approximately 200 for the cloud size and density mentioned above. Therefore, we work with $\kappa \approx 200$ in this chapter.

To determine the gravitational force, we assume a spherical mass distribution in the bulge and halo. For the bulge, we assume a total mass of $M_b \sim 0.1 M_d$ inside a radius $r_b \sim 0.1 r_d$ for simplicity. For the distribution of dark matter, we once again consider a NFW profile, with total mass M_h (Navarro et al., 1996). We fix M$_h$ for a given disc mass (M_d), by the ratio $M_h/M_d \sim 20$, as determined by Mo et al. (1998) and we use their prescription to evaluate the disc exponential scale-length (R_d). we use this scale-length as the size of galactic disc to compute the disc forces. Gravitational potential of NFW halo is,

$$\Phi_{\mathrm{NFW}} = -\frac{GM_h}{\ln(1+c) - c/(1+c)} \left[\frac{\ln\left(1 + \frac{r}{r_s}\right)}{r} \right] \tag{4.10}$$

where r_s is the NFW scale length and r_{vir} is the radius within which the mean overdensity is 200. $c = \frac{r_{\mathrm{vir}}}{r_s}$ is the halo concentration parameter. We use the value of c as obtained from the M_h–c relation given by Macciò et al. (2007). The NFW potential implies a gravitational force along z which is given by,

$$\begin{aligned} f_{halo,z} &= \left| -\frac{\partial \Phi_{\mathrm{NFW}}}{\partial z} \right|_{R=0} \\ &= \frac{GM_h}{z^2} \left[\frac{\ln(1+\frac{z}{r_s}) - z/(z+r_s)}{\ln(1+c) - c/(1+c)} \right] \end{aligned} \tag{4.11}$$

4.2.2 Equation of motion for clouds

Using the expressions for various forces as given above, one can finally rewrite eqn(4.3) for evaluating the velocity of clouds as a function of z,

$$\begin{aligned} v\frac{dv}{dz} &= \frac{\dot{p}_h (1 - v/v_h)^2 \, \mathcal{H}(v_h - v)}{4 N_H \, \mu m_p \, (\pi z^2/2)} + 2\pi G \Sigma \Gamma_0 \left(\frac{R_d^2}{z^2 + R_d^2} \right) \\ &- 2\pi G \Sigma \left(1 - \frac{z}{\sqrt{z^2 + R_d^2}} \right) - \frac{GM_b}{z^2} - \frac{GM_h}{z^2} \left(\frac{\ln(1+\frac{z}{r_s}) - \frac{z}{z+r_s}}{\ln(1+c) - \frac{c}{1+c}} \right) \end{aligned} \tag{4.12}$$

where Γ_0 is given by equation (4.9). We use $\mu = 1.4$ and $N_H \sim 10^{21}$ cm^{-2} (e.g. Martin, 2005; Heckman et al., 2000). Here the first term on RHS denote ram pressure, second the radiation pressure and the last three terms represent the gravity of the disc, bulge & NFW halo respectively. This equation is non-linear due to the presence of v in ram pressure term and should be solved numerically, although previous authors have approximated it assuming $v \ll v_h$. The form of the ram pressure term suggests that ram pressure would not be effective once the velocity becomes greater than velocity of hot component. Hence the ram pressure is likely to be effective for low-mass galaxies.

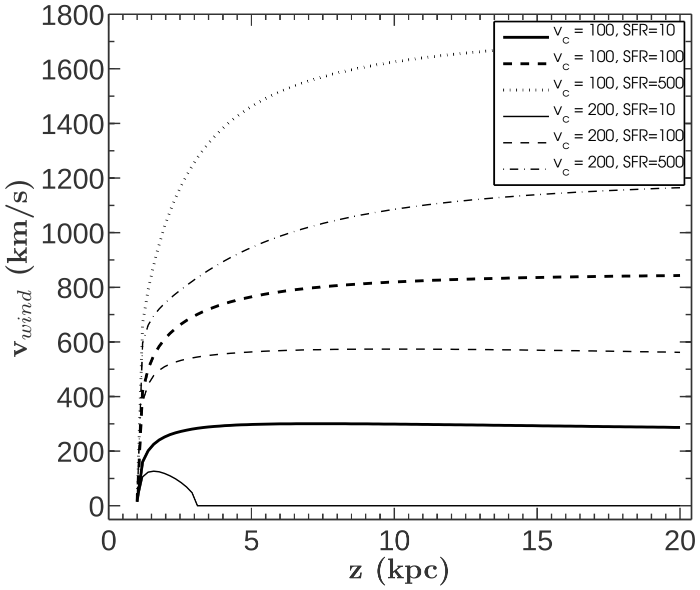

Figure 4.2: Variation of wind speed with vertical distance (z) for galaxies of different circular speeds. The thick solid, dashed and dotted lines refer to $v_c = 100$ km s^{-1}, and for SFR of $10, 100, 500$ M$_\odot$ yr^{-1}, respectively. The thin solid, dashed and dot-dashed lines refer to $v_c = 200$ km s^{-1}, for the same values of SFR, respectively.

4.3 Results

We solve the wind equation (equation 4.12) numerically. Figure 4.2 shows the wind speed as a function of z for different values of SFR for two galaxies, with $v_c = 100$ km s^{-1} and $v_c = 200$ km s^{-1}. Instead of rising continuously, the wind speed saturates after travelling a distance of ≥ 10 kpc, with a terminal speed that is lower for higher mass galaxies. The thick solid line roughly corresponds to M82, and the wind speed ~ 300 km s^{-1} is consistent with the observations (Heckman et al., 2000; Schwartz & Martin, 2004).

4.3.1 Outflow velocity as a function of v_c and SFR

Next we solve the wind equation for a grid of values of SFR and galaxy circular speed (v_c), for the cases of ram pressure and radiation pressure alone, and then for the combination of the two.

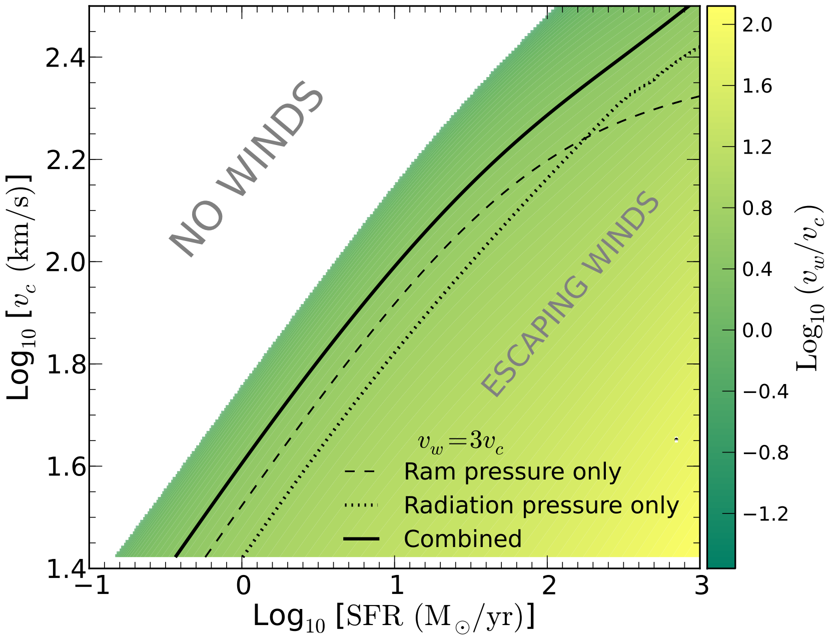

Figure 4.3: Ratio of wind speed (v_w) and the galaxy circular speed (v_c) is shown using the colour coding. We have also plotted the contour levels where $v_w/v_c = 3$, for three cases as follows : thick solid line for combined ram and radiation pressure driving; dashed line for only ram pressure driving and the dotted line for only radiation pressure driving.

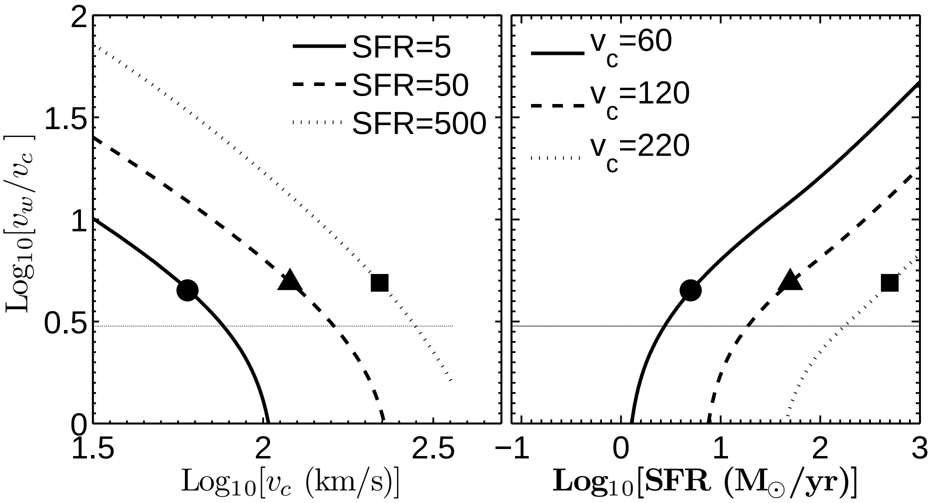

Figure 4.4: Ratio of wind velocity at 20 kiloparsec and the galactic rotation speed plotted with v_c for three different SFR in the left panel and with SFR for three different v_c in the right panel. Three representative cases are shown with solid circle (dwarf starbursts), solid triangle (LIRGs) and solid square (ULIRGs). The thin horizontal line corresponds to $v_w = 3v_c$.

In Figure 4.3 we plot the logarithm of wind velocity (v_w) at 20 kpc, in units of v_c, as a function of v_c and SFR using colour code. The white part of the plot toward the top left corner represents the cases when there are 'no winds'. The coloured part of the plot is where we find non-zero wind speeds. The interface between the 'no wind' and 'wind region' roughly follows the scaling $v_c \propto \mathrm{SFR}^{3/8}$. Using the scaling of this interface, we can write following criteria for outflows,

$$\mathrm{SFR}^{3/4}_{10\ \mathrm{M_\odot/yr}}\, v^{-2}_{c,140\ \mathrm{km/s}} > 1 \tag{4.13}$$

In Figure 4.3, the wind velocity increases as one moves diagonally towards the bottom right corner in the coloured region of the plot. The escape velocity in a NFW halo is roughly $\sim 3v_c$. Therefore, we plot the contour for $v_w = 3v_c$ using a solid line to find out which of the winds are going to escape. The escaping winds are the ones which lie on the right side of the thick solid line. We note that this contour is due to a combination of ram and radiation pressure driving. We wish to explore which of these processes is effective at a particular point in this plot. Therefore, we plot two more contours, one using a dashed line to represent the case of only ram pressure driving and another contour using a dotted line to represent the case of only the radiation pressure driving. In the case of only radiation pressure, the wind speed is found to be roughly proportional to SFR, which can be understood from the fact that $\Gamma_0 \propto \mathrm{SFR}$. The case for only ram pressure appears to better power the wind in low mass galaxies. However, from the dashed contour it is clear that ram pressure can not drive the cold clouds out of the galaxies with rotation speeds $\gtrsim$ 200 $\mathrm{km\,s^{-1}}$, which is due to the maximum limit on hot wind speed. However for galaxies with $v_c \gtrsim 200\ \mathrm{km\,s^{-1}}$, the radiation pressure wins over the ram pressure. This points to the existence of a critical rotation speed above which the physical mechanism of outflow changes. Therefore outflows from galaxies with $v_c \lesssim 200$ km/s and SFR $\lesssim 100$ M$_\odot$/yr are dominated by ram pressure and those from the more massive galaxies with larger SFR, are influenced more by radiation pressure.

We further elaborate on the winds from galaxies with three representative values of v_c and SFR. We show the variation of v_w/v_c with circular speed (v_c) and SFR for three representative galaxies in the left and right panels of Figure 4.4. We find that, for a constant SFR, v_w/v_c decreases with v_c, as the gravitational force increases with v_c. The three representative cases in this plot are as follows : dwarf starbursts (solid circle: $v_c \sim 60$ km s^{-1}, SFR ~ 5 M$_\odot$ yr^{-1}), LIRGs (solid triangle: $v_c \sim 120$ km s^{-1}, SFR ~ 50 M$_\odot$ yr^{-1}), ULIRGs (solid square: $v_c \sim 220$ km s^{-1}, SFR ~ 500 M$_\odot$ yr^{-1}). The values of v_w/v_c for three representative galaxies are greater than 3, which can be taken as a criteria for escape and shown by the thin horizontal line. Interestingly the near constancy of v_w/v_c for the three representative points recovers the observed scaling of v_w with v_c. We can find the slopes of lines in Figure 4.4,

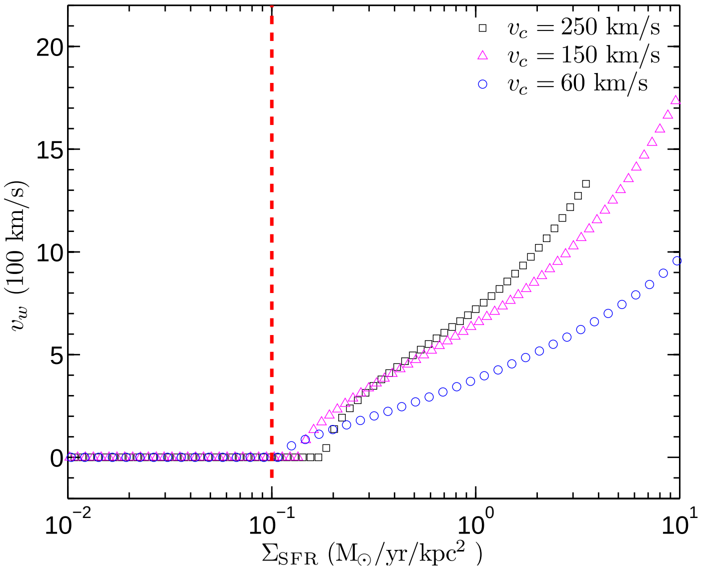

Figure 4.5: Wind velocity is plotted as a function of $\Sigma_{\rm SFR}$ from our solutions. The data for three values of circular speed v_c are shown; using squares for $v_c = 250$, triangles for $v_c = 150$ and circles for $v_c = 60$ $\rm km\ s^{-1}$. The vertical dashed line represents the threshold value of $\Sigma_{\rm SFR}$ for driving outflows from observations (Heckman, 2002).

and infer the scaling of v_w/v_c with v_c and SFR. We find that, for the galaxies which satisfy the criteria in equation (4.13) in our solutions, the wind velocity can be approximated by the following fit,

$$\frac{v_w}{v_c} \sim 10^{0.7} \left[\frac{\rm SFR}{50\,{\rm M_\odot/yr}}\right]^{0.4} \left[\frac{v_c}{120\,{\rm km/s}}\right]^{-1.25} . \tag{4.14}$$

Observations show that the winds are generally observed for galaxies with star formation surface density , $\Sigma_{\rm SFR} \gtrsim 10^{-1}\ {\rm M_\odot\ yr^{-1}\ kpc^{-2}}$ (Heckman, 2002). If we consider that the circular speed is roughly proportional to the radial extent of the galactic disc, then our theoretical criteria in equation (4.4) would imply a similar condition on $\Sigma_{\rm SFR}$. We have solved the wind equation (4.12), for every possible combination of v_c and SFR. According to formalism of Mo et al. (1998), circular speed of the galaxy is proportional to the scale radius (R_d) in disc galaxy . Using this we find the value of R_d corresponding to a particular v_c. Therefore, we now have a solution for wind speed for all combinations of R_d and SFR, where each combination should represent a galaxy. We then find $\Sigma_{\rm SFR}$ for these galaxies using the relation, $\Sigma_{\rm SFR} = {\rm SFR}/(2\pi R_d^2)$ [*]. We then plot the wind velocity from our calculation, for each $\Sigma_{\rm SFR}$ in Figure 4.5 for galaxies with circular speeds $v_c = 250$, 150 and 60 $\rm km\ s^{-1}$ using squares, triangles and circles respectively. Interestingly we find non-zero wind speeds only for galaxies with $\Sigma_{\rm SFR}$ larger than the threshold value, $\Sigma_{\rm SFR,threshold} \approx 10^{-1}\ {\rm M_\odot\ yr^{-1}}$

---

[*] An extra 2 is there because R_d is the scale radius of an ‘exponential’ disc in the formalism of Mo et al. (1998).

kpc^{-2}. We note that the threshold value for wind shows a mild increase with circular speed (or equivalently the galactic mass) of the galaxy which is understandable due to increase in gravitational pull with mass. In fact the behaviour with mass is evident if we go back to our theoretical criteria in equation (4.13), and use $v_c \propto R_d$, then we get an interesting trend which is, $\Sigma_{\rm SFR,threshold} \propto R_d^{2/3} \propto M_h^{2/9}$. To end this section, we also note that for large and fixed value of $\Sigma_{\rm SFR}$, the wind velocity increases with the circular speed, a correlation reported recently (Martin, 2005; Rupke et al., 2005b).

4.4 Discussions

The most important result of our calculation is that galactic outflows require both ram and radiation pressure, especially for high mass and high SFR cases. Our calculation has a number of ingredients from stellar physics and disc and halo parameters, and apart from the value of the hot wind speed v_h, there is no free parameter in this calculation. It is therefore interesting to note that our theoretical results are consistent with most data of outflows when studied in the parameter space of v_c and SFR. It is also interesting that a recent simulation with ram and radiation pressure driven outflows has concluded that these two processes are important in different mass regimes, although it is not clear where the dividing line between the two regimes lies (Sharma et al., 2011; Hopkins et al., 2012). (Cold clumpy) outflows from galaxies on the left of the contours in Figure 4.3 are unlikely to escape into the IGM and likely get trapped in the circumgalactic region or fall back (Oppenheimer & Davé, 2008).

Next we compare our results with the outflow observations in parameter space of v_c and SFR. For this purpose we compile a set of outflow data from the studies in past two decades, covering a wide range of galaxies from dwarf starbursts to supermassive ULIRGs. In Figure 4.6, we plot the separating boundary between ‘no winds’ and ‘winds’ using a red dashed curve in the parameter space of v_c and SFR. We have also shown the boundary for criteria for escaping winds using a thick solid line. We then overplot various data sets, which we have compiled, as follows : squares for ULIRGs from Martin (2005); Genzel et al. (2001), triangles for high redshift ULIRGs from Weiner et al. (2009), asterisks for dwarf starbursts from Schwartz & Martin (2004), big blue cross for ULIRGs from Rupke et al. (2005b), filled circles for faint dwarfs from Martin (1998). Apart from these we have also shown two representative galaxies from a recent SPH simulation in which the cosmic rays power the galactic winds (Uhlig et al., 2012).

We find that our theoretical results explain the observation in the region $v_c \gtrsim 100 \ {\rm km \ s^{-1}}$, SFR$\gtrsim 1$ M$_\odot$/yr. Recent observations of ULIRG winds (Martin, 2005; Rupke et al., 2005b;

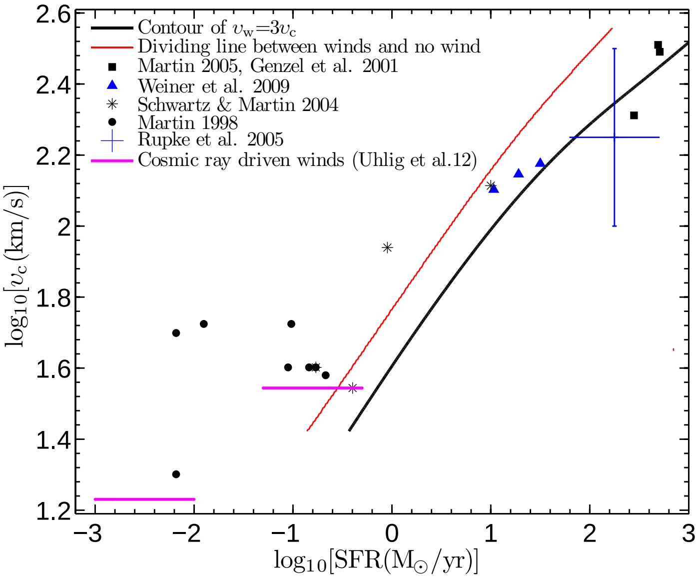

Figure 4.6: Contours of wind velocity v_w at 20 kpc, in units of v_c for combined ram and radiation pressure driving. Thick black contour is for $v_w/v_c = 3$ and the thin red contour separates no wind region on the left from the wind region on the right. The wind velocity increases as one moves from top left corner to bottom right corner. Also plotted are the data points with different symbols: squares (Martin, 2005; Genzel et al., 2001), triangles (Weiner et al., 2009), filled circles (Martin, 1998), asterisks (Schwartz & Martin, 2004), big blue cross represents the range of data in Rupke et al. (2005b). We have also shown the galaxies from simulation of Uhlig et al. (2012), using two red bars, which represent the case of cosmic ray driving.

Weiner et al., 2009) fall within our theoretical prediction and also follow the trend of constant v_w/v_c. This implies that cold outflows from these galaxies may indeed be driven by the combined action of ram and radiation pressure. We note that the faint dwarf galaxies in which Martin (1998) and Schwartz & Martin (2004) have reported outflows (circles and astrisks), lie on the left of the red curve, which is the region where our theoretical model predict no outflows. Also if we calculate the star formation surface density for these galaxies we find that only a few of them satisfy $\Sigma_{\rm SFR} > 0.1$ M$_\odot$ yr^{-1} kpc^{-2}, which is the criteria for winds. This points to some other process, responsible for powering winds in these galaxies. One such process may be the cosmic ray streaming and resulting outflows (e.g. Ipavich, 1975; Samui et al., 2008; Uhlig et al., 2012). Recently, using SPH simulations of cosmic ray streaming, Uhlig et al. (2012) have shown that this mechanism can power the outflows in low SFR and low mass galaxies (shown by two pink bars in Fig. 4.6). We explore the theoretical basis behind cosmic ray driven wind from low mass galaxies in Appendix G of this thesis.

We note that our results assumed a value of $v_h \sim 800$ km s^{-1}, and a column density of cold clouds of $\sim 10^{21}$ cm^{-2}. If we assume a larger value of v_h (~ 1000 km s^{-1}), then the contour for only ram pressure will be able to explain the winds in ULIGs with large SFR and high mass. A similar result will follow from larger values of κ for the radiation pressure case.

It is interesting to note that the contour for only radiation pressure can explain the ULIRG region of Figure 4.3 (top right corner). Extending to larger SFR, our results indicate that radiation pressure will also be important for Hyperluminous Infra Red Galaxies (HLIRGs) (Rowan-Robinson, 2000). Lastly, although it may appear that the role of radiation pressure in galaxies other than ULIRGs is less dominant than ram pressure as far as energetics is concerned, radiation pressure may still play an important role in lifting the clouds to a large height before it is embedded in the hot wind to help it survive long (Nath & Silk, 2009; Murray et al., 2011).

In summary, we have studied the outflows from disc galaxies driven by ram and radiation pressure. We found the criteria for the existence of outflows at the scales of ~ 20 kpc in galaxies. We further explained theoretically the threshold value of $\Sigma_{\rm SFR}$, required for outflows as reported in observations. We compared our results with data in the parameter space of galaxy circular speed and SFR. We found that the driving mechanism of escaping wind is different in low mass and high mass galaxies, with radiation pressure being important for high mass galaxies with high SFR. We also found that outflows may occur in galaxies even with very low star formation rates (SFR< 0.5 M$_\odot$ yr^{-1}), however a different mechanism would be operating in such cases. One such mechanism is the cosmic ray streaming as discussed in Appendix G.

Chapter 5

Hydrodynamic Model for SNe and AGN Driven Outflows

Based on :
Sharma, M. & Nath, B. B. 2013, ApJ, 763, 17

The standard SNe/starburst driven free-wind models neglected the effect of dark matter halo gravity (e.g. Chevalier & Clegg, 1985). Gravity may not be important for dwarf galaxies but definitely important for the high mass galaxies (e.g. Mac Low & Ferrara, 1999). SNe driven winds are important for low mass galaxies and the inclusion of these in galaxy formation models can account for observed stellar content of galaxies at low mass end of the halo mass function. At the higher mass end, it is believed that AGN feedback shapes the galaxy luminosity function. In semi-analytic modelling the SNe and AGN feedback are used as free parameters which are tuned to explain the observed galaxy properties. A proper understanding for the outflow velocities and mass loss, invoked by current studies of galaxy formation, is still missing. We address these questions in this chapter and construct a trans-sonic wind model taking into account the energy injection from SNe and momentum injection from AGN.

Main Results

- We derive steady state closed form solutions for the hydrodynamic wind from NFW dark matter halo driven by the energy and mass injection from SNe and the momentum injection from an Eddington limited AGN.

- We find that the wind dynamics depends on three velocity scales: (a) $v_\star \sim (\dot{E}/2\dot{M})^{1/2}$ describes the effect of starburst activity, with $\dot{E}, \dot{M}$ as energy and mass injection rate in a central region of radius R; (b) $v_\bullet \sim (GM_\bullet/2R)^{1/2}$ for the effect of a central black hole of mass $M_\bullet$ on gas at distance R and (c) $v_s = (GM_h/2\mathcal{C}r_s)^{1/2}$ which is closely related to the circular speed (v_c) for NFW halo, with r_s as the halo scale radius and $\mathcal{C}$ is a function of halo concentration parameter.

- We find a general expression for wind terminal speed given by $v_\infty = (4v_\star^2 + 6(\Gamma - 1)v_\bullet^2 - 4v_s^2)^{1/2}$, where Γ is the ratio of force due to radiation pressure to gravity of the central black hole.

- We find that the winds from quiescent star forming galaxies cannot escape when the halo mass is in range $10^{11.5} \leq M_h \leq 10^{12.5}$ $\mathrm{M}_\odot$. We note that the circumgalactic gas at large distances(> 10 kpc) from galaxy centres should be present for galaxies in this mass range.

- For an escaping wind, the wind speed in low to intermediate mass galaxies is $\sim$ 400–1000 km/s, consistent with observed X-ray temperatures.

- We find that the winds from massive galaxies with AGN at Eddington limit (due to electron scattering) should have speeds $\gtrsim 1000 \mathrm{~km~s^{-1}}$.

- Using inputs from our outflow model, we derive stellar to halo mass ratio in galaxies, following the scheme suggested in Granato et al. (2004) and Shankar et al. (2006). We find that the stellar to halo mass ratio peaks roughly at $M_h \sim 10^{12}$ $\mathrm{M}_\odot$ where the cross-over occurs towards AGN domination in outflow properties from starburst activity at lower masses. The stellar mass for massive galaxies scales as $M_\star \propto M_h^{0.26}$, and for low mass galaxies, $M_\star \propto M_h^{5/3}$.

5.1 Introduction

In the standard scenario of galaxy formation the baryonic matter falls inside the potential wells created by dark matter halos. This in-falling material cools and forms stars. This picture is met with problems as the galaxy stellar mass function does not follow the halo mass function. Both low and high mass halos have significantly lower than predicted value of stellar masses (Somerville et al., 2008; Moster et al., 2010; Behroozi et al., 2010). To reconcile with these problems it has been proposed that the SNe and starbursts provide thermal energy injection and cause large amount of mass to flow out of the galaxy as galactic superwinds (Dekel & Silk, 1986; Larson, 1974; Oppenheimer & Davé, 2006). The star formation is suppressed as the galaxies lose a significant portion of their baryons due to this negative feedback. Although this picture can provide explanation for the low ratios of $M_\star/M_h$ for the low mass halos, but for the high mass halos, gravity becomes strong and the SNe are not sufficient to drive the gas out. In order to resolve the discrepancy at high mass end, it has been argued that the AGN outflows may sweep away the baryons and suppress the star formation in high mass galaxies (Silk & Rees, 1998; Wyithe & Loeb, 2003; Di Matteo et al., 2005; Springel et al., 2005; Croton et al., 2006; Bower et al., 2006). These two feedback processes, when considered together, are believed to explain the shape of galaxy stellar mass function at both low and high mass end (Binney, 2004; Cattaneo et al., 2006; Puchwein & Springel, 2013).

Apart from their cosmological importance as a feedback process, galactic winds have been a topic of research as a gas dynamical problem in galactic physics. Speculations on the possibility that galaxies can harbour large scale winds followed the models of solar wind developed by Parker (1965). Burke (1968) proposed a model of trans-sonic winds from the galaxy with heat and mass addition from SNe. It was further proposed that galactic winds may cause ellipticals to lose all of their gas (Johnson & Axford, 1971; Mathews & Baker, 1971). The review by Holzer & Axford (1970) gives an elaborate account of the theoretical aspects of solar and galactic winds. Chevalier & Clegg (1985) showed that energy injection at the center can drive a fast super-wind from the dwarf star-burst galaxy M82. In this work the gravity of the galaxy was not considered and the obtained solutions were trans-sonic with a heat injection up to the sonic point. Wang (1995) modeled the wind from a power law gravitational potential and showed that wind may escape the galaxy or settle in a galactic corona depending on the mass of the galaxy and the effect of radiative cooling. Silich et al. (2011) studied the effects of cooling on winds from individual star clusters with exponential stellar density distribution. Winds driven by cosmic rays have also been studied in the literature (Ipavich, 1975; Breitschwerdt et al., 1991; Samui et al., 2008; Uhlig et al., 2012).

Observations show that the winds do not consist of a homogeneous medium. The hot gas emitting X-rays and the cold/warm gas visible in emission and absorption lines (Strickland et al., 2004; Bouché et al., 2012; Kornei et al., 2012), coexist in the galactic winds (Heckman et al., 2000; Veilleux et al., 2005). Hot phase appears as a smooth flow of tenuous gas while the colder phase is clumpy in nature. It is usually believed that cold neutral clouds form as a result of thermal instabilities in the hot flow and they are entrained with the parent flow because of its ram pressure (Heckman et al., 1993). Hydrodynamical simulations with radiative cooling also supported this scenario (Suchkov et al., 1994; Strickland & Stevens, 2000; Cooper et al., 2008). However, recent observations show that the velocity of neutral clouds does not correlate with the velocity of hot flow and rather it correlates with the circular speed of the host galaxy (Martin, 2005; Rupke et al., 2005b). If one considers the momentum driven winds where the radiation from the galaxy acts on the dust grains, then these observations can be explained (Murray et al., 2005; Sharma et al., 2011; Chattopadhyay et al., 2012; Nath & Silk, 2009). However, the radiation may not be sufficient in fainter low mass galaxies and ram pressure is still required to explain the cold winds in these galaxies (Sharma & Nath, 2012; Murray et al., 2011; Hopkins et al., 2012). On the other hand in high mass ULIRGs, radiation from AGN may be an alternate mechanism for driving outflows apart from SNe and stellar radiation.

In spite of the general consensus about the AGN driving in quasar outflows, observationally it has been hard to establish that outflows in galaxies are also powered by AGN (Rupke et al., 2005a; Westmoquette et al., 2012). However, recent observations do show compelling evidence for the AGN driving in galactic outflows (Sturm et al., 2011; Rupke & Veilleux, 2011; Alexander et al., 2010; Morganti et al., 2007; Dunn et al., 2010; Feruglio et al., 2010; Fu & Stockton, 2009; Villar-Martín et al., 2011). From the theoretical point of view, considerable amount of work has been carried out in modeling radiation driven outflows in the immediate vicinity of the AGN (Murray et al., 1995; Proga et al., 2000; Kurosawa & Proga, 2009; Risaliti & Elvis, 2010). However, the effects of radiation from accreting black holes has not been discussed for driving galaxy scale outflows. Murray et al. (2005) proposed the existence of a critical luminosity for the AGN (or the galaxy) necessary for the blow-out of all the available gas. The value of this critical luminosity depends on the dust scattering opacity at UV. Everett & Murray (2007) studied Parker wind from AGN occurring at scales of ~ 100 pc. Debuhr et al. (2012) carried out simulations showing that the initial momentum injection and the fast outflow in the vicinity of hole may shock the surrounding ISM and can result in a galaxy scale outflow. Whether the outflows due to the AGN are energy conserving or momentum conserving has been a topic of debate as well. Silk & Nusser (2010) argued that the energy driven outflows are not possible in the galactic bulges. King et al. (2011) proposed that AGN outflows are momentum driven at small scales and energy driven on larger scales. Faucher-Giguère & Quataert (2012) showed that the cooling in the region, shocked by AGN radiation pressure, may not be effective and the outflows can be energy conserving. McQuillin & McLaughlin (2012) studied the large scale motion of momentum-conserving supershells from a dark matter halo. Novak et al. (2012) carried out a radiation transfer calculation assessing the efficiency of various components of AGN spectrum in driving outflows. This work showed that most of the UV flux is quickly absorbed and re-radiated in IR. The IR radiation can drive a dusty outflow and may result in mass loss much higher than the line driving mechanisms, on the scales connecting the AGN and host galaxy as shown by radiation hydrodynamic simulations (Dorodnitsyn et al., 2011) .

It is evident from the studies on starburst and AGN driven outflows that these processes play an important role in the formation and evolution of galaxies. In galaxy formation models, these two processes are generally invoked using simple recipes through feedback factors. However, in theoretical models of winds they have been treated separately for the low mass and high mass galaxies. There is a lack of models that develop a complete hydrodynamic theory of winds which can envisage both these feedback processes. In this chapter we address this problem analytically and bring in both these wind driving agents together and using the analytical results from our calculation we also attempt an explanation for the galaxy stellar to halo mass relation.

We start with the derivation of a general wind equation in §5.2, which accounts for any possible mass, energy and momentum injection. We then present a brief derivation of SNe driven wind model of CC85 and extend this model to the case including a dark matter halo in §5.3. Afterwards in §5.5 we introduce the momentum injection from the AGN and derive a general analytic solution for the galactic wind, which has inputs from SNe injection, NFW gravity and the central black hole. This solution leads us to important results like the terminal velocity of winds, condition for escaping winds and the dependence of wind properties on the halo mass and the black hole mass. In §5.5.2 we show the velocity, density and temperature of the outflow as a function of the distance from the centre. Interestingly a class of our solutions can explain the gas reservoirs in the the galactic halos seen in observations (Tumlinson et al., 2011) and simulations (van de Voort & Schaye, 2012; Stinson et al., 2012). In §5.6, we study the cosmological implications of our results followed by discussion and summary of our findings.

5.2 Basic equations

We consider steady spherically symmetric winds driven by mass and energy/momentum injection from processes that are confined in a central region of radius R. Consider a heating rate $\dot{E}$ and mass injection rate $\dot{M}$ in this region, which has a size of a few hundred parsecs (see below) then the basic fluid equations can be written as,

$$\frac{1}{r^2}\frac{d}{dr}(\rho v r^2) = \dot{m} = \frac{\dot{M}}{V} \tag{5.1}$$

$$v\frac{dv}{dr} = -\frac{1}{\rho}\frac{dp}{dr} - \frac{d\Phi}{dr} + f(r) - \frac{\dot{m}v}{\rho} \tag{5.2}$$

$$\frac{1}{r^2}\frac{d}{dr}\left[\rho v r^2\left(\frac{v^2}{2} + \frac{c_s^2}{\gamma - 1}\right)\right] + \rho v\left(\frac{d\Phi(r)}{dr} - f(r)\right) = q = \frac{\dot{E}}{V} \tag{5.3}$$

Here V is the volume of the central region in which the energy injection and the mass injection is occurring. $\Phi(r)$ represents the gravitational potential and $f(r)$ is the momentum injection force per unit mass. c_s is the Laplacian sound speed. In this work we will be considering the momentum injection from the AGN in optically thin limit hence the $f(r)$ has an inverse square dependence on r. The above written system of equations do not have a critical point if the heating and mass injection is zero. However, for a finite energy and mass injection there is a critical point. For an extended energy and mass distribution the critical point can be determined numerically as done for super star-cluster winds in Silich et al. (2011). To extract maximum information analytically we have considered the energy and mass injection to be confined in a region of radius $r = R$, following Chevalier & Clegg (1985, hereafter CC85). Therefore in the present case the critical point is situated right at the boundary of central injection region.

In this work we do not consider the radiative cooling, as it is generally believed that the energy loss via radiation over the entire wind is small and less dominant than the adiabatic loss (Grimes et al., 2009), hence the cooling does not affect the dynamics of the flow. However, it may still be important for the thermodynamics of the flow (see Appendix D) and may result in the precipitation of the wind which can not be dealt with the steady stable flow solutions. The dynamics and survival of clouds formed by thermal instability in the galactic wind is also an important issue and it has been studied elsewhere in the category of cold winds (Murray et al., 2011; Sharma & Nath, 2012; Marcolini et al., 2005; Cooper et al., 2009). Therefore, we distinguish our model from that of the clumpy winds and in the present work we study analytically the large scale dynamics of homogeneous steady outflow from a NFW dark matter halo and its cosmological implications.

By introducing the mach number $\mathcal{M} = v/c_s$, the above equations can be transformed to the following ordinary differential equation (see Appendix A for a complete derivation).

$$\frac{\mathcal{M}^2-1}{\mathcal{M}^2(\mathcal{M}^2(\gamma-1)+2)}\frac{d\mathcal{M}^2}{dr} = \frac{2}{r} - (1+\gamma\mathcal{M}^2)\frac{\dot{m}}{\rho v} - \frac{\dot{m}(1+\gamma\mathcal{M}^2)}{2\rho v}\left(\frac{\dot{E}/\dot{M}}{\epsilon(r)} - 1\right) + \frac{(\gamma+1)\left(f(r)-\frac{d\Phi(r)}{dr}\right)}{2(\gamma-1)\epsilon(r)} \tag{5.4}$$

where $\dot{m} = \dot{M}/V$ and $\epsilon(r) = \frac{v^2}{2} + \frac{c_s^2}{\gamma-1}$. We will use $\gamma = 5/3$. As mentioned above, the terms $\dot{E}$ and $\dot{M}$ represent the energy and mass injection in a central region of size $r = R$, beyond which they become zero. We use $R = 200$ pc for the present work.

5.2.1 Zero gravity case: Chevalier & Clegg's solution

In this section we briefly reproduce the CC85 solution, therefore this subsection also serves as a consistency check for equation (5.4). In the CC85 solution gravitational force of the galaxy is not considered as the wind speeds were of the order of thousand $\mathrm{km\,s^{-1}}$ which is an order of magnitude larger than the circular speed of starburst galaxy M82. There is no external driving force ($f(r) = 0$). Hence the main driving force is the energy injection from SNe in a central 200 pc region. The size of the central region also marks the boundary where the energy injection and the subsonic part ends. The wind equation then can be solved analytically for subsonic ($\mathcal{M} < 1$) and supersonic ($\mathcal{M} > 1$) part of the wind.

In order to derive the subsonic part of the solution, we can use $\dot{m} = 3\rho v/r$ which results from the integration of continuity equation. Therefore equation (5.4) becomes

$$\frac{\mathcal{M}^2-1}{\mathcal{M}^2(\mathcal{M}^2(\gamma-1)+2)}\frac{d\mathcal{M}^2}{dr} = \frac{2}{r} - \frac{3(1+\gamma\mathcal{M}^2)}{r} - \frac{3(1+\gamma\mathcal{M}^2)}{2\,r}\left(\frac{\dot{E}/\dot{M}}{\epsilon(r)} - 1\right) \tag{5.5}$$

Direct integration of energy equation (5.3) by retaining the energy and mass injection and neglecting the gravity and external driving results in, $\epsilon(r) = \dot{E}/\dot{M} = 2v_\star^2$, where we have defined a velocity parameter, $v_\star = \sqrt{\dot{E}/2\dot{M}}$. It can be shown that at the critical point, $v_{\rm crit} = v(R) = c_s(R) = v_\star$. Substituting this $\epsilon(r)$ in equation (5.5), we get,

$$\frac{\mathcal{M}^2-1}{\mathcal{M}^2[(\gamma-1)\mathcal{M}^2+2]}\frac{d\mathcal{M}^2}{dr} = \frac{-1-3\gamma\mathcal{M}^2}{r} \tag{5.6}$$

This can be integrated to get the following solution,

$$\delta_<(\mathcal{M}) = \left(\frac{3\gamma+1/\mathcal{M}^2}{3\gamma+1}\right)^{-\frac{3\gamma+1}{5\gamma+1}}\left(\frac{\gamma-1+2/\mathcal{M}^2}{\gamma+1}\right)^{\frac{\gamma+1}{2(5\gamma+1)}} = \frac{r}{R}\,; \qquad r < R \tag{5.7}$$

Following similar steps and additionally dropping the injection terms, we can evaluate supersonic part of the solution. Analytically it implies setting $\Phi = f = \dot{M} = \dot{E} = 0$ in the wind equation (5.4). Therefore, we are left with the following differential equation,

$$\frac{\mathcal{M}^2 - 1}{\mathcal{M}^2[(\gamma-1)\mathcal{M}^2 + 2]} \frac{d\mathcal{M}^2}{dr} = \frac{2}{r} \tag{5.8}$$

This can be integrated to get the following solution for the supersonic part of the wind,

$$\delta_>(\mathcal{M}) = \mathcal{M}^{\frac{2}{\gamma-1}} \left(\frac{\gamma - 1 + 2/\mathcal{M}^2}{\gamma + 1} \right)^{\frac{\gamma+1}{2(\gamma-1)}} = \left(\frac{r}{R}\right)^2 \; ; \qquad r > R \tag{5.9}$$

These expressions were arrived at by CC85. We shall use these definitions of $\delta_<(\mathcal{M})$ and $\delta_>(\mathcal{M})$ in the rest of this chapter. The terminal velocity of the wind in this solution can be obtained easily from the energy equation which gives $\epsilon(r) = v^2/2 + c_s^2/(\gamma-1) = 2v_\star^2$. For $r \to \infty$, the sound speed can be neglected and we get $v_\infty = 2v_\star = (2\dot{E}/\dot{M})^{1/2}$. In the supersonic part of the wind for $\mathcal{M} > 1$ the relation in equation (5.9) can be approximated by $\mathcal{M}^3 \propto r^2$. Therefore, when the velocity attains its terminal value, then $c_s^2 \propto T \propto r^{-4/3}$ and $\rho \propto r^{-2}$.

5.3 SN driven winds from NFW halo

In this section we study the effects of NFW dark matter halo on the wind velocity in detail. One can therefore consider the calculation in this section as an extension of the supersonic part of CC85 solution. We proceed first by fixing the dark matter halo parameters in the next subsection.

5.3.1 Dark matter halo properties

Here we discuss the properties of the NFW dark matter halo which will be used throughout the rest of the chapter. We consider a Navarro Frank and White(NFW) dark matter halo with a density profile $\rho = \rho_s r_s^3/[r(r+r_s)^2]$ (Navarro et al., 1996). For a dark matter halo of total mass M_h, which collapses at a redshift z, the virial radius is given by $r_{\rm vir} = [3M_h/(4\pi\Delta_c(z)\Omega_m^z\rho_{crit})]^{1/3}(1+z)^{-1}$ Where Δ_c is the critical over density which can be written as $\Delta_c(z) = 18\pi^2 - 39d_z^2 + 82d_z$, with $d_z = \Omega_m^z - 1$ and $\Omega_m^z = \frac{\Omega_m(1+z)^3}{\Omega_m(1+z)^3 + \Omega_\Lambda + \Omega_k(1+z)^2}$ with parameters having their usual meaning (Bryan & Norman, 1998; Bullock et al., 2001). We set $\Omega_m = 0.258,\ \Omega_\Lambda = 0.742,\ h = 0.72$, according to the results from WMAP5 (Komatsu et al., 2009). Using these values, the virial radius can be written as

$$r_{\rm vir} = 210 \left(\frac{M_h}{10^{12}\ \mathrm{M_\odot}}\right)^{1/3} \left[\frac{\Omega_m}{\Omega_m^z}\frac{\Delta_c(z)}{18\pi^2}\right]^{-1/3} (1+z)^{-1}\ \ \mathrm{kpc} \tag{5.10}$$

The corresponding circular speed is, $v_c = \sqrt{GM_h/r_{\rm vir}}$. So it can be written as,

$$v_c = 143 \left(\frac{M_h}{10^{12}\,{\rm M_\odot}}\right)^{1/3} \left[\frac{\Omega_m}{\Omega_m^z}\frac{\Delta_c(z)}{18\pi^2}\right]^{1/6} (1+z)^{1/2}\ \ {\rm km\ s^{-1}} \tag{5.11}$$

The gravitational potential due to the NFW dark matter halo can be written as,

$$\Phi_{\rm NFW} = -\frac{GM_h}{\ln(1+c) - c/(1+c)}\,\frac{\ln(1+r/r_s)}{r} = -2v_s^2\,\frac{\ln(1+r/r_s)}{r/r_s} \tag{5.12}$$

In this $v_s^2 = GM_h/2\mathcal{C}r_s$ and $\mathcal{C} = \ln(1+c) - c/(1+c)$. Also $r_s = r_{\rm vir}/c$ is the NFW scale radius with c as the halo concentration parameter which depends on both halo mass and the redshift of virialization. We use the fitting formula for c given by Muñoz-Cuartas et al. (2011).

5.3.2 Effect of dark matter halo on winds

We study the effect of gravity in the supersonic part of the solution. In the subsonic part, the NFW gravity does not make a difference as shown in Appendix B. Therefore the subsonic part is same as in the previous section and we can assume that the energy injection propels the gas to a speed of $v_{\rm crit} = v_\star = (\dot{E}/2\dot{M})^{1/2}$ at the critical point. To study the supersonic solution beyond the critical point ($r > R$) , we set $\dot{E}$ and $\dot{m}$ equal to zero, and use the NFW potential in equation (5.4), which results in the following equation for the supersonic part,

$$\frac{\mathcal{M}^2 - 1}{\mathcal{M}^2[(\gamma-1)\mathcal{M}^2 + 2]}\,\frac{d\mathcal{M}^2}{dr} = \frac{2}{r} - \frac{2}{\epsilon(r)}\,\frac{d\Phi_{\rm NFW}(r)}{dr} \tag{5.13}$$

where $\epsilon(r) = v^2/2 + c_s^2/(\gamma-1)$. From the direct integration of energy equation we obtain

$$\begin{aligned} &\left.\frac{v^2}{2} + \frac{c_s^2}{\gamma-1} + \Phi_{\rm NFW}(r)\right|_R^r = 0 \\ \Rightarrow\quad &\epsilon(r) = 2v_\star^2 + \Phi_{\rm NFW}(R) - \Phi_{\rm NFW}(r) \end{aligned} \tag{5.14}$$

where we have used the value of velocity at the critical point as $v_{\rm crit} = v(R) = c_s(R) = v_\star = (\dot{E}/2\dot{M})^{1/2}$ Substitution of this $\epsilon(r)$ in equation (5.13) followed by integration results in,

$$\ln|\delta_>(\mathcal{M})| = 2\ln|r| + 2\ln|2v_\star^2 + \Phi_{\rm NFW}(R) - \Phi_{\rm NFW}(r)| + const. \tag{5.15}$$

where $\delta_>(\mathcal{M})$ is defined in equation (5.9). In Appendix C we have plotted the contours of $\mathcal{M}$ versus r for an arbitrary value of constant. For the analysis here we pick the solution which has a critical point at radius R. To pick that solution we set, $\delta_>(\mathcal{M}) = 1$ and $r = R$

in the above equation which fixes the constant and we get,

$$\delta_{>}(\mathcal{M}) = \left[\frac{r}{R}\right]^2 \left[\frac{2v_\star^2 + \Phi_{\rm NFW}(R) - \Phi_{\rm NFW}(r)}{2v_\star^2}\right]^2 \tag{5.16}$$

Using the definition of $\Phi_{\rm NFW}$ given in equation (5.12) we get,

$$\delta_{>}(\mathcal{M}) \simeq (r/R)^2 \left[1 - \frac{v_s^2}{v_\star^2}\left(1 - \frac{\ln(1+r/r_s)}{r/r_s}\right)\right]^2 \tag{5.17}$$

where $v_s = \sqrt{GM_h/2\mathcal{C}r_s}$. Comparing with equation (5.9), one can clearly see that the solution picks up an additional term due to the gravitational force of NFW halo. The solution has three different regimes depending on the value of the ratio $v_\star^2/v_s^2$, as described below

- case 1 : $v_\star^2 >> v_s^2$
  This is the case when the initial injection upto the critical point is very strong and hence the wind velocity at the critical point is large. Then we can neglect the ratio $v_s^2/v_\star^2$, and we get
  $$\delta_{>}(\mathcal{M}) = (r/R)^2 \tag{5.18}$$
  The NFW halo has negligible effect in this particular case and we have recovered the supersonic part of CC85 solution.

- case 2 : $v_\star^2 = v_s^2$
  In this case we get
  $$\delta_{>}(\mathcal{M}) = \left(\frac{r_s}{R}\ \ln(1+r/r_s)\right)^2 \tag{5.19}$$
  which shows that the gravity of dark matter halo affects the flow significantly. As there is a logarithmic dependence in the above equation, therefore in large $\mathcal{M}$ limit, the Mach number and hence the velocity increases slowly with r, in comparison to the case without gravity.

- case 3 : $v_\star^2 < v_s^2$
  In this interesting case, we find that the wind speed decreases and finally becomes zero at some distance. This distance is decided by the ratio $v_\star^2/v_s^2$, and can be determined by requiring that R.H.S = 0 at some $r = r_{\rm F}$. We get,
  $$\frac{\ln(1+r_{\rm F}/r_s)}{r_{\rm F}/r_s} = 1 - \frac{v_\star^2}{v_s^2} \tag{5.20}$$
  If the ratio $v_\star^2/v_s^2 \sim 0$ then $r_{\rm F} \sim 0$ from the above equation, which contradicts the assumption in deriving this solution as it is a supersonic solution and valid for $r > R$.

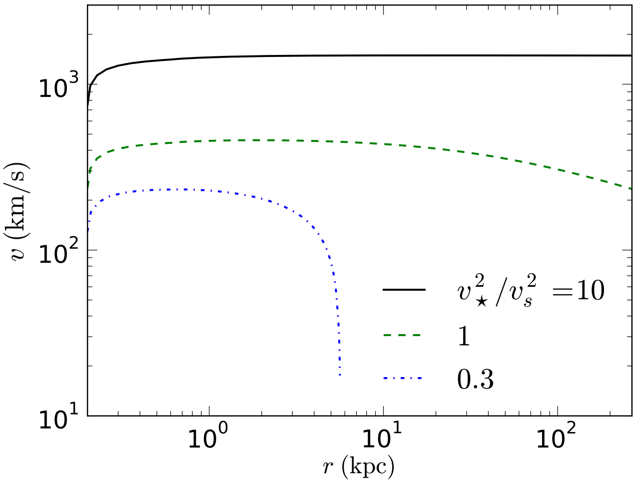

Figure 5.1: The wind velocity in the supersonic regime for the solution with Navarro-Frenk-White dark matter halo. The reference mass used is $M_h = 10^{12}\mathrm{M}_\odot$. The solid, dashed and dotted line are for $v_\star^2/v_s^2 = 10, 1, 0.3$ respectively. The x-axis starts at $r = R = 200$ pc and ends at the virial radius of the halo.

It implies that the ratio needs to have a finite value so that we get, $r_\mathrm{F} > R$. Therefore, in this case wind starts with velocity being equal to the sound speed at $r = R$ and then stops at a distance r_F.

Another interesting result which can be deduced from the above equation is the condition for escape of the wind. If $v_\star = v_s$ then $r_\mathrm{F} = \infty$, which means that winds will escape the galaxy. Hence any heating occurring at the base need to somehow propel the gas at least to a speed of $\sim v_s$ so that the gas can escape the galaxy.

In Figure 5.1 we plot the supersonic wind velocity for a reference halo mass $M_h = 10^{12}\ M_\odot$ with other NFW parameters calculated using definitions in §5.3.1 at $z = 0$. The value of $v_s = 236\ \mathrm{km\ s}^{-1}$ for this halo. The solid line is for $v_\star^2 = 10v_s^2$ and in this case the injection is large so that the gravity of the halo does not affect the flow. That is why the solid line leaves the plot window and the wind velocity at largest distance is $\approx 1500\ \mathrm{km\ s}^{-1}$ which is double the value at $r = R$ in agreement with the result $v_\infty = 2v_\star$ of previous section on the solution of CC85. The dashed line represents the case 2 when $v_\star = v_s$ and the NFW gravity is important. Consequently the velocities are reduced and at the virial radius, we get a wind velocity $\sim 200\ \mathrm{km\ s}^{-1}$. The dotted line is for $v_\star^2 = 0.3v_s^2$ and it represents the case 3 discussed above. This line exhibits the flow which ends inside the galactic halo at a final radius, $r_\mathrm{F} \sim 50$ kpc. We find that for the low $v_\star$ values, which implies a low value of velocity at the critical point, the gas stops at some point within the halo. We note that similar solutions were obtained by Wang (1995) for power-law potential, and for specific values of wind speed and mass loss rate, but the calculations were done numerically. The analytical model presented here generalizes these solutions to NFW halo and to general values of wind speed.

5.4 Injection parameters and value of $v_\star$

In the last section we discussed the importance of the ratio, $v_\star^2/v_s^2 = \dot{E}/(2\dot{M}v_s^2)$. Here we would like to determine the possible values of $v_\star$ which we will use for the rest of the analysis. We can define the energy injection from supernovae per unit time as $\dot{E} = \alpha f_{SN}\dot{M}_\star \times (10^{51}\ \mathrm{erg})$ where 10^{51} erg is the energy output of a single supernova, α is the fraction of this energy retained by the gas after radiative energy losses, $\dot{M}_\star$ is the SFR in solar mass per year and f_{SN} stands for energy injection per year per solar mass of star formation. For a Kroupa-Chabrier IMF, $f_{SN} \sim 1.26 \times 10^{-2}$. Therefore we have,

$$\dot{E} \approx \left[\alpha\ \dot{M}_\star\ (4 \times 10^{41})\right]\ \mathrm{erg\ s^{-1}} \tag{5.21}$$

The mass injection rate is written as

$$\dot{M} = \beta \mathcal{R}_f \dot{M}_\star \tag{5.22}$$

Where $\mathcal{R}_f$ is the return-fraction. Typically 30% of the mass is returned to the ISM hence $\mathcal{R}_f \approx 0.3$. The factor β takes into account the entrainment of mass from ISM which can increase the overall mass injection. For the starburst galaxy M82, β is in the range 1.0 to 2.8 which gives $\dot{M} \sim$ 1.4 – 3.6 $\mathrm{M_\odot\ yr^{-1}}$ (Strickland & Heckman, 2009). Martin (1999) found that for a range of galaxies from low to high masses the mass loss rate roughly scales with SFR (see also Heckman, 2002). We therefore use $\dot{M} \sim \dot{M}_\star$, which corresponds to $\beta\mathcal{R}_f \sim 1$.

With these value of $\dot{E}$ and $\dot{M}$ we estimate the value of $v_\star$ which is $(\dot{E}/2\dot{M})^{1/2} = 562\sqrt{\alpha}$ $\mathrm{km\ s^{-1}}$. We consider two modes of energy injection from SNe. In the first case, almost 90% of the energy of SNe is lost via radiation and only a small fraction goes into heating of the wind. For this 'quiescent mode', we use $\alpha = 0.1$ which gives $v_\star \approx 180$ km s^{-1}. In the other case, when the central injection region is dense and the supernovae are overlapping so that radiative losses reduce, and due to thermalization, 30% to 100% of the supernova energy goes in heating the wind (Strickland & Heckman, 2009). This type of situation is evident in galaxies like M82 where the SFR is generally high and the injection regions are supposedly quite dense. For such a case $\alpha = 0.3$ – 1.0 and we get $v_\star \approx 308$ – 562 km s^{-1}. To represent this mode we take $v_\star = 500\ \mathrm{km\ s^{-1}}$. We will call this the 'starburst mode'.

The values of $v_\star$ chosen here brackets the range of the possible values. We emphasize that this range of $v_\star$, when equated with sound speed corresponds to a temperature range of roughly $\sim 0.2 - 1$ keV, which is consistent with the hot wind temperatures observed in a wide range of galaxies (Martin, 2005). On the other hand the quiescent mode ($v_\star = 180\ \mathrm{km\ s^{-1}}$) is suitable for the galaxies with low values of SFR, like our own Galaxy. This particular mode also yields interesting results, and we will discuss the implications in a later section.

5.5 Winds in the presence of AGN

The AGN is important as it gives a strong momentum injection to the gas via its radiation field. A large fraction of AGNs show the evidence of outflowing gas, and it is possible that all AGNs drive outflows and they are observed when they are viewed edge-on. Theoretically, these outflows have been associated with the co-evolution of black holes and the bulge of the host galaxy (Silk & Rees, 1998; King, 2003, 2005). How the AGN interacts with the ISM of the host galaxies and whether it can drive a large scale outflow which can escape the galaxy is an important question. AGN can affect the gas in the host galaxy indirectly where it produces fast nuclear winds which shock the ISM into shells. The fate of these shells is then decided by the supply of energy and momentum injection from the inner regions. Apart from this indirect way AGN can also interact with the dust-rich ISM directly via its radiation field. This interaction is capable of driving large scale outflows (Murray et al., 2005). Here we consider this mechanism and model the outflows as being driven by (Eddington limited) continuum radiation from the black hole.

5.5.1 Effect of momentum injection from AGN

Momentum injection can be provided by the AGN in several ways. Firstly it can be provided via the scattering of photons by the free-electrons. As the Thompson opacity is generally small ($\kappa_T \approx 0.34$ cm^2 gm^{-1} for a fully ionized gas with solar metallicity), this may be effective in the regions close to AGN where the densities are quite large and the radiation field is strong. Another way momentum is transferred to produces outflows is via line driving mechanism (Murray et al., 1995; Proga et al., 2000). We consider the momentum injection via the absorption and scattering of AGN radiation by dust grains. Dust opacities are rather high and recent models of momentum driving of outflows due to AGNs and galactic radiation as well, consider the scattering of photons by dust grains. The gas is assumed to be coupled to these grains through momentum coupling, and get dragged. We justify this assumption in Appendix E.

Let us derive the force due to momentum injection by AGN radiation ($f(r)$) which then will be substituted in equation (5.4). In its general form, the momentum injection from a radiation field can be written as,

$$f(r) = \kappa \frac{\mathcal{F}}{c} \tag{5.23}$$

where κ is the volume averaged opacity, $\mathcal{F}$ stands for the frequency integrated flux of radiation and c is the speed of light. For spherical symmetry and for a optically thin atmosphere, the radiation flux can be written as $\mathcal{F} = L/4\pi r^2$. Hence the force of radiation becomes $\kappa L/4\pi r^2 c$. This force has an inverse square dependence on r, hence it can be represented as a factor (Γ) times the gravitational force of the black hole. Therefore, if the gravity of the central black hole is given by $f_{grav} = -GM_{\bullet}/r^2$ then in the presence of an outward radiation force, the effective force is written as $f_{g,eff} = -(1-\Gamma)GM_{\bullet}/r^2$ with $\Gamma = \kappa L/(4\pi GM_{\bullet}c)$. For $\Gamma = 1$, the effective force is zero, and for the case of Thompson scattering the corresponding luminosity is called the Eddington luminosity (L_E). The luminosity required to exactly cancel the gravitational force may be different depending on the opacity and process responsible for momentum injection. For example, in case of scattering of UV light by dust, for which the opacity is roughly 3500 times the electron-scattering opacity (Draine, 2003), only a luminosity of $\sim 0.001\ L_E$ is required to counter the black hole gravity. However, it has been showed recently that most of the UV photon field from the AGN may get attenuated within a short distance because of the large optical depths in AGN environments (Novak et al., 2012). In that case the re-radiated Infrared(IR) photons serve as the mainstay of AGN radiation (see also Dorodnitsyn et al. (2011). Therefore in this work we consider the momentum injection from IR radiation. IR to dust scattering opacity is, $\kappa_{IR} = 13$ cm^2 gm^{-1}, in K band (Li & Draine, 2001; Draine, 2003) for a gas to dust ratio of 125. Opacity in IR is not as large as it is in UV, however we find that it is large enough to drive strong outflows in massive galaxies. Hence the momentum injection force in our case becomes,

$$f(r) = \frac{\kappa_{IR} L}{4\pi r^2 c} = \Gamma \frac{GM_{\bullet}}{r^2} \tag{5.24}$$

where $\Gamma = \kappa_{IR} L/(4\pi GM_{\bullet}c)$. We consider an Eddington limited AGN ($L = L_E$), where $L_E = (4\pi GM_{\bullet}c/\kappa_T)$ is the usual Eddington luminosity for electron scattering. This fixes the value of $\Gamma = \kappa_{IR}/\kappa_T \approx 38$, for our case.

We need to justify that the atmosphere is optically thin in IR so that we can work with a constant Γ. In order to do this we estimate the optical depth for IR light. Optical depth can be estimated as, $\tau \sim \int \kappa\rho(r)dr$. Using $\kappa_{IR} = 13$ cm^2 gm^{-1} and $\rho \sim 10$ m$_\mathrm{p}$ cc^{-1}which, as we will see is an upper limit for density in our wind models, the optical depth comes out to be 0.01 at 20 pc and 0.13 at 200 pc. Even at the edge of the injection region the optical depth is very small, hence we conclude that the atmosphere is optically thin to IR radiation. Beyond

200 pc, the density decreases rapidly, as the wind expands adiabatically in the supersonic regime. As we will see in next section, density becomes as low as $0.001\ \mathrm{m_p}\ \mathrm{cc}^{-1}$ at 10 kpc, hence the wind material stays optically thin to IR radiation at large distances as well.

Let us consider the supersonic section of the wind in which both SNe and AGN radiation are effective. (See Appendix B for the subsonic part of this wind.) For the supersonic part the energy and the mass injection both are zero, although the gravity due to NFW halo and the effective force due to radiation and gravity from the central AGN are present. The total potential can be written as,

$$\Phi_{total}(r) = \Phi_\bullet(r) + \Phi_{\rm NFW}(r) = -\frac{GM_\bullet}{r} - 2v_s^2\,\frac{\ln(1+r/r_s)}{r/r_s} \tag{5.25}$$

With the aid of this total potential and the momentum injection term $f(r) = \Gamma GM_\bullet/r^2$, the wind equation (5.4) for supersonic part ($r > R$) can be written as,

$$\frac{\mathcal{M}^2-1}{\mathcal{M}^2[(\gamma-1)\mathcal{M}^2+2]}\frac{d\mathcal{M}^2}{dr} = \frac{2}{r} - \frac{2}{\epsilon(r)}\left(\frac{(1-\Gamma)GM_\bullet}{r^2} + \frac{d\Phi_{\rm NFW}(r)}{dr}\right) \tag{5.26}$$

Next we integrate the energy equation directly as below,

$$\begin{aligned} & \epsilon(r) - \frac{(1-\Gamma)GM_\bullet}{r} + \Phi_{\rm NFW}(r)\Bigg|_R^r = 0 \\ \Rightarrow\quad & \epsilon(r) = \left[2v_{\rm crit}^2 - 2(1-\Gamma)v_\bullet^2 + \Phi_{\rm NFW}(R)\right] + 2(1-\Gamma)v_\bullet^2\frac{R}{r} - \Phi_{\rm NFW}(r) \end{aligned} \tag{5.27}$$

where we have used $\epsilon(R) = 2v_{\rm crit}^2 = 2v_\star^2 - (1-\Gamma)v_\bullet^2$, from Appendix B for the subsonic section of this wind. We have also used $v_\bullet^2 = GM_\bullet/2R$. The term inside the square bracket in the above equation is a constant, so if we substitute eq (5.27) in 5.26 it becomes exactly integrable and we get,

$$\begin{aligned} \ln|\delta_>(\mathcal{M})| &= 2\ln|r| \\ &+ 2\ln\left|2v_{\rm crit}^2 - 2(1-\Gamma)v_\bullet^2 + \Phi_{\rm NFW}(R) + 2(1-\Gamma)v_\bullet^2\frac{R}{r} - \Phi_{\rm NFW}(r)\right| + const. \end{aligned} \tag{5.28}$$

Using the condition*, $\delta_>(\mathcal{M}) = 1$ at $r = R$, and substituting the expression for NFW potential we get,

$$\delta_>(\mathcal{M}) \approx (r/R)^2\left[1 - (1-\Gamma)\frac{v_\bullet^2}{v_{\rm crit}^2}\left(1-\frac{R}{r}\right) - \frac{v_s^2}{v_{\rm crit}^2}\left(1 - \frac{\ln(1+r/r_s)}{r/r_s}\right)\right]^2 \tag{5.29}$$

---

[*] By imposing this condition we have picked the solution which becomes supersonic at $r = R = 200$ pc. To see the complete solution space the reader is referred to the $\mathcal{M}$ versus r diagrams in Appendix C.

where $v_{\rm crit}^2 = v_\star^2 - (1-\Gamma)v_\bullet^2/2$. This equation gives the complete solution of the wind from a galaxy driven by energy injection from SNe and momentum injection from the AGN. Let us discuss some asymptotic behaviours,

- Terminal speed :
  We use the Bernoulli equation (5.27) to obtain the terminal speed. Taking the limit $r \to \infty$ in equation (5.27) and neglecting the sound speed we obtain the following general expression for terminal speed of SNe and AGN driven wind from a NFW halo,

  $$v_\infty = 2\left(v_\star^2 + \frac{3}{2}(\Gamma - 1)v_\bullet^2 - v_s^2\right)^{1/2} \tag{5.30}$$

  Here $v_s^2 = GM_h/(2\mathcal{C}r_s)$. In the absence of dark matter halo and the AGN we can neglect v_s and $v_\bullet$ which gives $v_\infty = 2v_\star$. However in presence of NFW gravity but no AGN we get the relation $v_\infty = 2\sqrt{v_\star^2 - v_s^2}$. For dwarf galaxies, the effect of NFW gravity can be neglected, and therefore the wind speed in starburst mode is expected to be $v_\infty \approx 1000$ km s^{-1} , consistent with observations of winds in starburst galaxy M82. If the black hole is massive so that the $v_\bullet$ dominates then by neglecting $v_\star$ and v_s and putting $\Gamma = 38$, we get $v_\infty \approx 15v_\bullet$, which for a black hole of mass $\sim 10^9$ M$_\odot$ estimates to $v_\infty \sim 1500$ km s^{-1} .

- Behaviour with r :
  In equation (5.29) if the SNe injection term ($v_\star$) is dominant then we get $\mathcal{M}^3 \propto r^2$. When the wind is moving with constant terminal speed, $T \propto r^{-4/3}$ and $\rho \propto r^{-2}$ as derived in §2.1. If the AGN provides the main driving then neglecting v_s and $v_\star$ from equation (5.29), for large r, we once again retain $\mathcal{M}^3 \propto r^2$, and hence the scaling $T \propto r^{-4/3}$. The density scales as $\rho \propto r^{-2}$.

It is clear that, apart from the $v_\star$, the wind properties depend on two more terms. One involves $v_\bullet$ which is a parameter of the black hole and the other being v_s, which depends on the mass of NFW halo. To proceed further we need to learn whether the black hole mass is somehow related to dark matter halo.

Observations show that the black hole mass is related to the velocity dispersion of the central spheroidal bulge component of the galaxies, and the relation can be written as

$$\log\left(\frac{M_\bullet}{\rm M_\odot}\right) = a + b\log\left(\frac{\sigma}{200\ {\rm km\ s^{-1}}}\right) \tag{5.31}$$

This correlation has been extensively studied in the literature, with slightly different values for a and b. We will list a few of them. Gebhardt et al. (2000) was one of the earliest to report the correlation with $a \simeq 8.08 \pm 0.07$ and $b = 3.75 \pm 0.3$. Ferrarese (2002) gives $a \simeq 8.22 \pm 0.08$ and $b = 4.58 \pm 0.52$. Values in Tremaine et al. (2002) reads $a = 8.13 \pm 0.06$ and $b = 4.02 \pm 0.32$. For our analysis we use $a = 8.12$ and $b = 4.24$ from a recent study by Gültekin et al. (2009).

We also use a relation between the σ and circular speed v_c. Ferrarese (2002) reported a correlation between the circular speed in outskirts of galaxy and the σ, given roughly as $v_c \propto \sigma^{0.84\pm0.09}$. Similar relations were also deduced by Baes et al. (2003) and Pizzella et al. (2005). All these relation are very close to the linear relation $v_c = \sqrt{2}\sigma$ for spherical mass distribution (Binney & Tremaine, 2008), found in massive ellipsoidal galaxies where the bulge to total mass ratio is unity (see also Volonteri & Stark 2011). Hence for our analysis we use $v_c = \sqrt{2}\sigma$.

The relation between v_c and σ breaks down for low mass galaxies (Ferrarese, 2002). It is easy to understand this as the lower mass galaxies may admit a bulge to total mass ratio less than unity. Hence the galaxies with smaller bulges will have the mass of their black holes smaller than the one expected from $M_\bullet$–σ–v_c relation. On similar grounds, Kormendy & Bender (2011) concluded against the co-evolution of central black hole and dark matter halo. However, they also showed that a cosmic conspiracy causes v_c to correlate with σ for massive galaxies ($v_c \gtrsim 200 \mathrm{km\ s^{-1}}$).

We would like to emphasize here that even if the v_c–σ relation breaks down below a $v_c \lesssim 200\ \mathrm{km\ s^{-1}}$, still it does not make a difference in our results because the AGN term is effective only for very massive systems. In equation (5.26) it is the relative values of $v_\bullet$ and v_s, which govern the dynamics. For v_c=200 $\mathrm{km\ s^{-1}}$, using $c = 12$ we get $v_s = (GM_h/2\mathcal{C}r_s)^{1/2} \approx 400\ \mathrm{km\ s^{-1}}$ which is larger than $(\sqrt{\Gamma - 1})v_\bullet \approx 100\ \mathrm{km\ s^{-1}}$, and the black hole term is even smaller for $v_c < 200\ \mathrm{km\ s^{-1}}$.

Using the $M_\bullet$–σ relation provided by Gültekin et al. (2009), aided with the relation $\sigma = v_c/\sqrt{2}$, where v_c is given by equation (5.11) we arrive at the following relation between black hole mass and the halo mass (see also Volonteri & Stark (2011)).

$$\left(\frac{M_\bullet}{0.74 \times 10^7\, M_\odot}\right)^{1/\sqrt{2}} \simeq \left(\frac{M_h}{10^{12}\, \mathrm{M}_\odot}\right)\left[\frac{\Omega_m}{\Omega_m^z}\frac{\Delta_c(z)}{18\pi^2}\right]^{1/2}(1+z_{\mathrm{vir}})^{3/2} \tag{5.32}$$

where z_{vir} is the redshift at which the halo collapsed and got viriallized. This relation can be used to determine $v_\bullet$ as a function of halo mass through, $v_\bullet = (GM_\bullet/2R)^{1/2}$. Substituting $v_\bullet$ and $v_s = \sqrt{GM_h/2r_s\mathcal{C}}$ in equation (5.29) with r_s and $\mathcal{C}$ determined from the redshift dependent definitions for NFW parameters given in §5.3.1. This enables us to compute the mach numbers as a function of r for the galaxy of any desired halo mass(M_h) and its halo collapsing at any desired redshift. The mach numbers can then be converted to the velocity simply by multiplying it with the sound speed which can be obtained using the relation $c_s^2 = \epsilon(r)/(\mathcal{M}^2/2 + 1/(\gamma - 1))$.

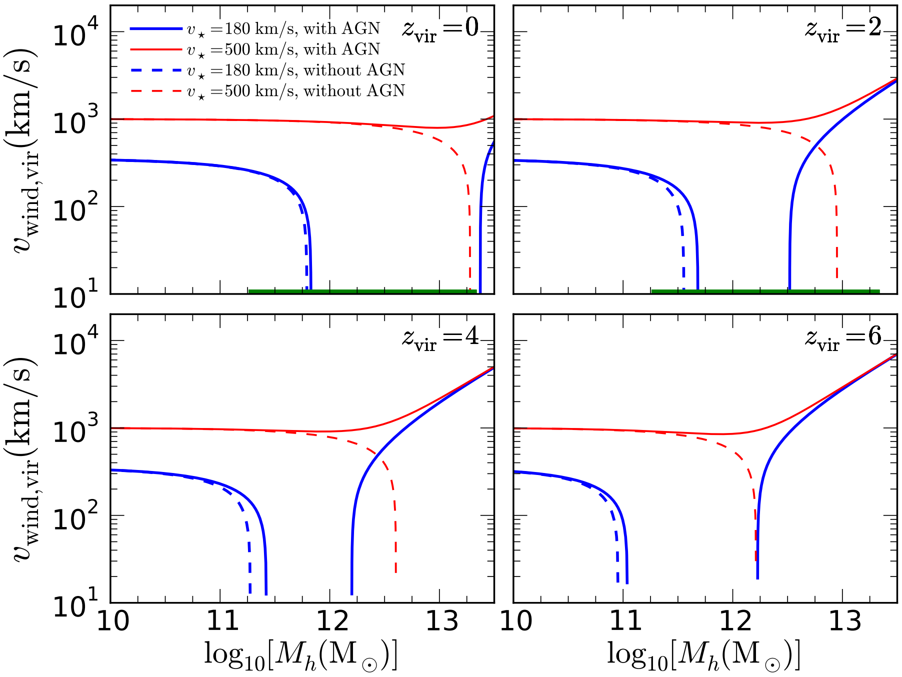

Figure 5.2: Wind velocity at virial radius as a function of halo mass for four different redshifts of collapse, $z_{\rm vir} = 0, 2, 4, 6$ in the panels from top-left to bottom-right respectively. The thin red lines in each panel are for starburst mode ($v_\star = 500$ km s^{-1}) and thick blue ones are for quiescent mode ($v_\star = 180$ km s^{-1}). Dashed line represent the outflow speeds without AGN. The green bar on x-axis in top two panels gives the range of galaxies in which the gas reservoirs in halos are observed (Tumlinson et al., 2011).

In Figure 5.2 we plot the wind velocities at virial radius† ($v_{\rm wind,vir}$) as a function of halo mass(M_h). The velocities are obtained by solving equation (5.29) with inputs from equation (5.32) and definitions in §5.3.1. We show the results corresponding to four different value of $z_{\rm vir}$ in four panels. red lines are for the starburst mode $v_\star = 500$ km s^{-1} and the blue lines are for the quiescent mode $v_\star = 180$ km s^{-1} . The dashed lines represent the solution without AGN and these show that the wind velocities cut of at some halo mass as the gravity becomes strong enough to counter the energy injection. For larger value of $v_\star$ this cut-off occurs at a larger halo mass.

Consider a situation in which for low halo masses the AGN driving term is smaller than the NFW gravity term. This implies that the wind velocity at virial radius in low mass halos decreases with increase in halo mass. However, the black hole mass also increases with the

---

[†] Wind velocity at virial radius ($v_{\rm wind,vir}$) need not be equal to the the terminal speed at infinity (v_∞) as the later is calculated by using the fact that the gravitational force at the infinity is zero while in case of $v_{\rm wind,vir}$ there may be a contribution from NFW gravity at virial radius.

halo mass. Since the slope of $M_\bullet$–M_h relation is greater than unity, hence the rate of increase of the black hole or AGN term is larger and at a particular halo mass it overcomes the NFW gravity term. Hence for largest galaxies we should see an increase in wind velocity with halo mass, which indeed is the case as shown by rising solid lines for massive halos. One can further compare the solid lines with dashed lines where the latter represent the case without the AGN and does not show any winds in high mass galaxies, which is a confirmation of the fact that in high mass galaxies outflows are driven by AGN.

The thick solid blue curve is special as it features the wind quenching due to NFW gravity as well as the high velocity winds due to AGN. There is a falling part of the curve which exhibits the cut off at some halo mass and then there is another part which rises at some larger halo mass. Hence there exist a range of halo masses roughly within $10^{11-13}\mathrm{M}_\odot$, which do not have escaping winds. The exact value of this range depends on the redshift of collapse ($z_{\rm vir}$). For example at $z_{\rm vir} = 0$ the rising part of the thick blue curve, which shows the effect of AGN, starts rising beyond a halo mass of $10^{13}\mathrm{M}_\odot$ while for $z_{\rm vir} = 2$ it rises roughly at a halo mass $\sim 10^{12}\mathrm{M}_\odot$. This is easy to understand as the AGN driving depends on the black hole mass which does increase with redshift (see equation 5.32). Also the falling part of the thick blue curve ends at a smaller halo mass for a larger value of $z_{\rm vir}$, because the value of v_s increases with redshift. We would like to mention here that the recent detection of gas reservoirs in the halos of galaxies by Tumlinson et al. (2011) covers roughly the similar range in halo masses shown by the green bar on x-axis in upper two panels of Figure 5.2.

If we focus on the wind velocities in lower to intermediate mass halos $M_h < 10^{12}\mathrm{M}_\odot$, we find that AGN never dominate in these and if there are winds they have to be driven by starbursts and SNe. We note that the wind velocities in low mass galaxies fall in the range 400–1000 km s^{-1} , depending on the efficiency of the energy injection process. These velocities agree with the ones inferred from the X-ray temperatures of the superwind regions in dwarf straburst and luminous infrared galaxies (Heckman et al., 2000; Martin, 1999). However, in case of galaxies with halo mass, $M_h \gtrsim 10^{12.5}\mathrm{M}_\odot$ the wind velocities either exceed 1000 km s^{-1} or they are quenched, depending on whether the AGN is present or not.

We note that in low mass galaxies where the outflows are driven by SNe, the wind velocity, $v_{\rm wind} \lesssim 1000$ km s^{-1} . However, this limit is exceeded when an AGN is present, since the curves with AGN show wind velocities $\gtrsim 1000$ km s^{-1} . This reveals the presence of a dividing line of 1000 km s^{-1} between SNe and AGN domination in velocity space as well.

In a hot wind with velocity of $v_{\rm wind}$ the neutral clumps in the wind can be dragged via the ram pressure. Maximum velocity these clouds can achieve is the velocity of the hot wind. As mentioned above, $v_{\rm wind}$ is always within 1000 km s^{-1} at the low mass end where SNe injection dominates, therefore the cold clouds should also be outflowing with velocity lower than 1000 $\mathrm{km\,s^{-1}}$. On the other hand at the higher mass end, where the AGN dominates, the velocities may exceed this limit. Interestingly, the observed outflow speeds of the neutral clouds in diverse galaxies like dwarf starbursts, ULIRGs, post-starburst galaxies and Low-ionization BAL quasars also follow this trend (Tremonti et al., 2007; Sturm et al., 2011; Trump et al., 2006).

It has been debated in the literature that the neutral cold/warm winds in ULIRGs are driven by ram pressure of the hot wind and/or radiation from stars in the galaxy or by the AGN. If we consider the winds driven by stellar radiation then the wind speed is roughly 3 times the circular speed of the galaxy (Murray et al., 2005; Martin, 2005; Sharma et al., 2011). For a massive ULIRG with a circular speed $\sim 300\,\mathrm{km\,s^{-1}}$ the wind velocity predicted by radiation driven wind model will be $900\ \mathrm{km\,s^{-1}}$. On the other hand, if ram pressure is the driving mechanism, then also the velocities of the continuous hot wind and hence of the neutral clouds can not exceed 1000 $\mathrm{km\,s^{-1}}$ unless an AGN is present. Therefore we emphasize that the observations of wind velocity in excess of 1000 $\mathrm{km\,s^{-1}}$ indicate the presence of an AGN.

5.5.2 Wind properties with distance : Implications for gas observed in galactic halos

In the last section we have established that for a particular mass range the galactic winds may not escape the galaxy. Therefore these galaxies are not very important for the intergalactic medium (IGM) enrichment. Interestingly our Milky Way with a total mass roughly $\sim 10^{12}\mathrm{M}_{\odot}$, also falls in this mass range. However, an important question arises for these type of galaxies, as to whether or not these galaxies can retain all the gas in the disk even though they can contain the gas inside r_{vir}.

We show in this section that infact these galaxies have outflows which spill their gas reservoir throughout the halo. In Figure 5.3 we show the radial dependence of wind properties for three galaxies which differ in the values of their halo mass. We have considered the halos collapsing at a redshift of $z_{\mathrm{vir}} = 2$ which corresponds to a look-back time of roughly ~ 10 Gyr. We choose this collapse redshift, as a fiducial value, in order to model galaxies like Milky Way and more massive galaxies, whose halos were already in place by $z \sim 2$. The thick disk in our Galaxy shows that Milky Way underwent its last major merger before ~ 10 Gyr, which corresponds to $z \sim 2$ (Gilmore et al., 2002). Therefore our results can be compared with observations of winds at low redshift ($z \leq 2$) universe.

In Figure 5.3, the thick blue lines refer to the quiescent mode ($v_{\star} = 180\ \mathrm{km\,s^{-1}}$) and the thin red lines represent the starburst mode ($v_{\star} = 500\ \mathrm{km\,s^{-1}}$). The solid lines denote

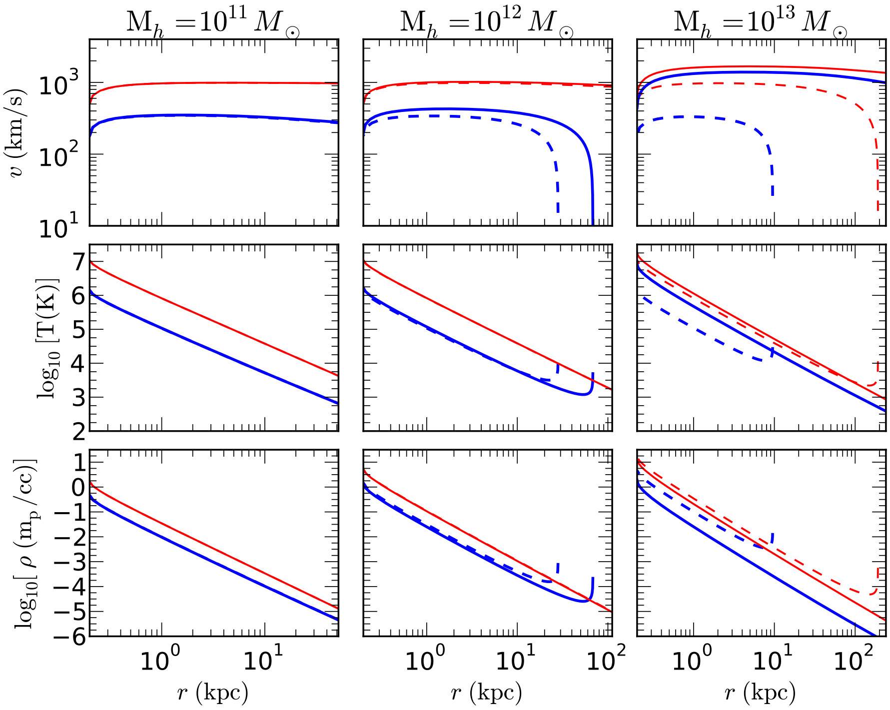

Figure 5.3: The wind properties as a function of distance from the base. Legend is same as in Figure 5.2. From left to right, the three columns correspond to three different halo masses, representing a dwarf galaxy, a Milky Way size galaxy and a giant galaxy respectively. The x-axis in all the plots extend upto the corresponding virial radius. The solid lines represent the winds in presence of an Eddington limited AGN and the dashed lines, the case of no AGN. Thin red lines represent the starburst mode ($v_\star = 500$ km s^{-1}) and the thick blue lines are for the quiescent mode ($v_\star = 180$ km s^{-1}). The middle row contains the temperature profiles of winds in three galaxies. The lowermost row shows the densities. To calculate densities we have used $\dot{M}_\star = 1, 3, 10$ M$_\odot$ yr^{-1} for $v_\star = 180$ km s^{-1} , and $\dot{M}_\star = 10, 30, 100$ M$_\odot$ for $v_\star = 500$ km s^{-1} , for three galaxies respectively.

the effect of AGN activity and dashed lines consider only the SNe injection. The upper panels plot the velocity as a function of radius, and the middle and bottom panels plot the temperature and densities respectively. The densities are estimated using the relation $\rho = \dot{M}/4\pi v r^2$, where $\dot{M} \sim \dot{M}_\star$. For three galaxies with $M_h = 10^{11}, 10^{12}, 10^{13}\mathrm{M}_\odot$, we have used $\dot{M}_\star = 1, 3, 10$ M$_\odot$yr^{-1} for quiescent mode and $\dot{M}_\star = 10, 30, 100$ M$_\odot$yr^{-1} for starburst mode respectively.

The curves show that for low mass galaxies, all types of winds (with or without AGN, quiescent and starburst mode) escape the virial radius. At the other extreme, for massive galaxies, winds with AGN activity can escape, but without an AGN, they stop at a distance within the halo ($\sim$ 10–200 kpc). The gas temperature and density slightly rises at this final halting point due to adiabatic compression. We would like to mention here that the radiative cooling can be important for these particular cases as the steady solution ceases to exist beyond a point. Even if the cooling time is shorter than the flow time initially, after many flow crossing times the cooling will become effective which may cause thermal instability. This can lead to formation of clouds whose fate then will be decided by the physical properties in their environment (see also Wang 1995).

For the intermediate mass galaxy ($M_h \sim 10^{12}\mathrm{M}_{\odot}$), we find that both of the thick blue lines (i.e., quiescent mode of star formation with or without AGN) are contained inside the virial radius. This implies that the wind needs strong starburst activity in order to escape the galaxy irrespective of whether or not AGN is present. The dashed thick blue line corresponds to a quiescent mode of star formation without AGN and roughly corresponds to our own Galaxy. Interestingly, we find that a slow wind is possible, which may extend to a distance of ~ 20 kpc. This can explain the recent observations of clouds roughly at 10–20 kpc in our halo (Keeney et al., 2006).

The solutions which end inside r_{vir} are important in the wake of recent observation of warm-hot gas clouds in the halo of our galaxy and for other galaxies as well (Tumlinson et al., 2011). Also recent simulations confirm these gas reservoirs around the galaxies of intermediate masses. Recent works find that although in the general scenario of galaxy formation the intermediate mass galaxies are efficient in retaining their baryons, these galaxies do not retain *all* of the baryons. It appears that only 20% to 30% of baryons are converted to stars in these galaxies as well (Somerville et al., 2008; Moster et al., 2010; Behroozi et al., 2010). Our results provide a natural explanation for the missing baryons in these intermediate mass galaxies.

5.6 Discussions

In this chapter we have studied galactic outflows driven by SNe injection and AGN radiation. We have calculated the outflow properties in halos ranging from low to high mass. The treatment is analytical which enabled us to extract fundamental results for these feedback processes. Below we present a simple analytical estimate of the stellar to halo mass ratio of galaxies, following the work of Granato et al. (2004); Shankar et al. (2006). Afterwords we recapitulate and discuss the results obtained in this work and a few caveats.

In the scenario of hierarchical structure formation low mass galaxies form at earlier times and post formation history is influenced by mergers and the periods of enhanced star formation activity. The semi-analytical modelling (SAM)(see Baugh 2006), which uses simple recipes for feedback and follows the structure formation according to ΛCDM model, can explain the observed properties of galaxies (Somerville et al., 2008). In recent years there have been a growing amount of observational evidence that the massive black holes were already in place at high redshifts. Also, it is well accepted that the massive galaxies formed their stars at earlier epochs as they appear redder at present times, compared to the younger galaxies in which star formation is still going on (Fontanot et al., 2009, and references therein). This phenomenon, which are commonly referred as 'downsizing', indicate a possible role the massive black holes would have played in quenching the star formation in massive galaxies at earlier epochs (Somerville et al., 2004; Granato et al., 2004; Croton et al., 2006). We follow the semi-analytical scheme proposed in Granato et al. (2004) for which an approximate analysis is provided in the Appendix A of Shankar et al. (2006), using which, we can write the rate of change of cool gas in halos as,

$$\dot{M}_{cold}(t) = \frac{M_{infall}(t)}{t_c} - \dot{M}_\star(t) + \mathcal{R}_f \dot{M}_\star(t) - \mathcal{L}\dot{M}_\star(t)\,, \tag{5.33}$$

where $\mathcal{R}_f$ is the return fraction of stars whose value is 0.3 for a Salpeter IMF. $\mathcal{L}\dot{M}_\star$ is the mass loss rate, t_c is the cooling time. $M_{infall}(t)$ is the mass available in the halo for infall at a time t . Equation (5.33) can be solved to obtain a time independant solution in large time limit and yields a stellar mass at present epoch as (see equation (17) in Shankar et al. 2006),

$$M_\star = f_{surv} \frac{f_{cosm} M_h}{1 - \mathcal{R}_f + \mathcal{L}}\,, \tag{5.34}$$

where $f_{cosm} = 1/6$ is the cosmic baryon ratio, f_{surv} is the fraction of stars surviving up to now and its value is approximately 0.6 for a Salpeter IMF. As $f_{surv},\ f_{cosm}$ and $\mathcal{R}_f$ are constants, therefore we get $M_{star} \propto M_h/\mathcal{L}$. In case of SNe feedback the feedback factor is written as $\mathcal{L} = \frac{\alpha f_{SN}(10^{51}\,\mathrm{erg})}{E_{bind}}$, where $E_{bind} = [v_c^2 f(c)(1+f_{cosm})/2]$ with $f(c)$ as given in Mo et al. (1998), represent the binding energy of gas in the halo per unit mass. The quantity in the numerator is nothing but $\dot{E}/\dot{M} = 2v_\star^2$ where $v_\star$ is the value of velocity at the critical point for the case of only SNe injection and no AGN. When the AGN is also present we can use the modified value of velocity at the critical point given in equation (5.27) which is $v_{\rm crit}^2 = v_\star^2 - (1-\Gamma)v_\bullet^2/2$. Hence in the case of both SNe and AGN feedback we can write the loss term $\mathcal{L}$ as,

$$\mathcal{L} = \frac{2v_{\rm crit}^2}{\frac{1}{2}v_c^2 f(c)(1+f_{cosm})} = \frac{2[v_\star^2 - (\frac{1-\Gamma}{2})v_\bullet^2]}{\frac{1}{2}v_c^2 f(c)(1+f_{cosm})} \tag{5.35}$$

$v_{\rm crit}$ is the velocity at the critical point and v_c the virial velocity of the halo. While the velocity at the critical point measures the strength of SNe and/or AGN as a mechanism of mass expulsion, the velocity at the virial radius is a measure of binding energy of the halo.

For NFW halo, $v_c \propto M_h^{1/3}$. Also $v_\bullet^2 \propto M_\bullet \propto M_h^{1.41}$ (see equation 5.32). Using these we get

$$M_\star \propto \frac{M_h}{1-\mathcal{R}_f+\frac{4v_\star^2+CM_h^{1.41}}{DM_h^{2/3}}} \propto \frac{M_h^{5/3}}{A+CM_h^{1.41}} \tag{5.36}$$

where C, D are constants and $A=[0.8f(c)v_c^2+4v_\star^2]$. From the above relation, for a fixed value of $v_\star$, we find that for small halo masses we have $M_\star \propto M_h^{5/3}$ and for large halo masses, when the AGN dominates, we get $M_\star \propto M_h^{0.26}$. The break occurs and $M_\star/M_h$ peaks roughly in the range $\sim 10^{12-12.5}\mathrm{M}_\odot$ as the ratio $v_{\rm crit}^2/v_c^2$ becomes minimum around this mass.

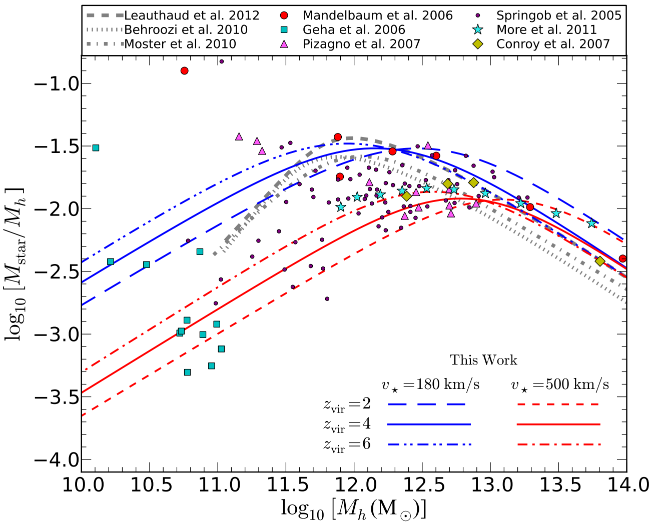

Figure 5.4: Stellar to halo mass ratio at present time from theoretical considerations in this work is compared with the observational data for individual galaxies courtesy Alexie Leauthaud. The upper three (blue) lines represent the case with $v_\star = 180 \ \mathrm{km\,s^{-1}}$ and may represent a quiescent galaxy. The lower three (red) lines are for $v_\star = 500 \ \mathrm{km\,s^{-1}}$. In these the dashed, solid and dash-dotted lines correspond to collapse redshifts, $z_{\rm vir} = 2$, 4 and 6 respectively. The data points are from Mandelbaum et al. 2006 : filled red circles, Geha et al. 2006:filled green squares, Pizagno et al. 2007 : filled purple triangles, Springob et al. 2005 : dots, More et al. 2011 : stars, Conroy et al. 2007 : diamonds. The thick gray dashed, dotted and dash-dotted lines represent the results of halo abundance matching from Leauthaud et al. (2012), Behroozi et al. (2010) and Moster et al. (2010) respectively.

In Figure 5.4, we plot the SHMR at present day, against the halo mass obtained by using equation (5.34), (5.35) and (5.32). The set of upper three blue lines is for $v_\star = 180 \ \mathrm{km\ s^{-1}}$ and the lower three red line represent $v_\star = 500 \ \mathrm{km\ s^{-1}}$. In each set the dashed, solid and the dash-dotted lines correspond to three different redshifts of collapse, $z_{\rm vir} = 2$, 4 and 6 respectively. We note that, in this section the quantity $v_\star$ is arbitrary and we have used two values to show the dependence of SHMR on $v_\star$. Also, we stress here that the theoretical lines denote the value of SHMR at present day ($z = 0$) for the galaxies which got viriallized at a particular $z_{\rm vir}$.

The squares, dots, and triangles in Figure 5.4 represent the stellar and halo mass data inferred from works on Tully fisher relation by Geha et al. (2006), Springob et al. (2005) and Pizagno et al. (2007) respectively. The stars and diamonds represent the data from (More et al., 2011) and (Conroy et al., 2007) who deduced the stellar and halo mass using stellar dynamics. Red circles shows the estimates based on weak lensing by (Mandelbaum et al., 2006). For details on the data sets the reader is referred to Leauthaud et al. (2012) and Blanton et al. (2008) and the original papers for the the data sets. We have also shown the SHMR obtained by the technique of halo abundance matching (Moster et al., 2010; Behroozi et al., 2010; Leauthaud et al., 2012) using broken thick gray lines. At the higher mass end we note that our results agree with these works. To be more specific we find a stellar to halo mass slope of 0.26 as mentioned above, which is in agreement with the value 0.29 deduced in Behroozi et al. (2010). The slope at higher mass end depends on the $M_\bullet - M_h$ relation, which is still being debated in the literature. However, even if we use a different scaling like $M_\bullet \propto \sigma^{4.02}$ given by Tremaine et al. (2002), then the slope at high mass end becomes 0.33 which is also in agreement with observations and other works.

The slope at low mass end as found by halo abundance matching is roughly ~ 2.2, which is larger than $5/3$ from theoretical considerations in this work and others (e.g. Dekel & Woo 2003). However, it is possible that other physical processes not considered in our model can explain the discrepancy. For example, if $v_\star$ depends on halo mass, with the efficiency of SNe energy injection being larger in low mass halos, the slopes can be reconciled.

If one naively compares the lines from our analytical calculation with the observational data points for individual galaxies then the plot seems to say something interesting. By looking at the data for low to intermediate mass galaxies (Geha et al., 2006; Springob et al., 2005; Pizagno et al., 2007) one may infer that the data points lie systematically below the results of halo abundance matching. There are a lot of galaxies which have lower stellar content than expected from halo abundance matching. However, if we compare these with our lower three red lines which are for starburst mode then these data points can be reconciled. As we have already described, the outflow activity in low to intermediate mass galaxies is governed by SNe and starbursts. The two modes we are following in this chapter represent two extreme efficiencies of energy injection by SNe. Quiescent galaxies like ours lie on one extreme and the violent galaxy like M82 on the other extreme. All the galaxies in low to intermediate halo mass range ($\lesssim 10^{12.5}\mathrm{M}_\odot$) are covered between these two extremes. Interestingly in Figure 5.4 also, most of the data points lie between the blue and red lines of our theoretical model which represent the quiescent and starburst mode of energy injection respectively. This is not mere a coincidence given the simplicity of our model and shows the importance of outflows in shaping the galaxies.

In the above analysis, we have assumed that the relation given in equation (5.34), which is valid in the long time limit, gives the stellar mass in the present day universe. In the hierarchical structure formation scenario where small halos form first and undergo periods of high merger rates, this assumption may not be completely valid. However, recent observations and theoretical works have shown that cosmic downsizing mitigates the effects of hierarchical structure formation models, and that massive galaxies are believed to form stars at high redshift after which they evolve passively.

Let us discuss our results and a few caveats as follows. We have found that the NFW gravity causes the outflows to stop inside virial radius in intermediate to high mass halos. In Appendix C, we have shown the solutions for winds from NFW halo in terms of Mach number, where the closed contours show the importance of the halo. In other words, gravitational force of the halo causes the flow to stop inside the virial radius if the energy injection from SNe is not large. We note that a minimum value of SNe energy injection so as to produce $v_\star \sim v_s$ is required for the gas to escape the galaxy. Our models in which the gas can not escape the galaxy, provides a natural explanation for the circumgalactic material observed inside the halos and also predict mild winds in quiescent star forming galaxies such as our Galaxy.

When an AGN component is included, the contours in the Mach number–radius plot can open up for massive galaxies ($M_h \gtrsim 10^{12.5} \mathrm{M}_\odot$). This implies that AGN radiation can become important in winds from massive galaxies (such as ULIGs), reaching a wind velocity of $v_{\rm wind} \gtrsim 1000 \ \mathrm{km \ s^{-1}}$. If we consider that neutral clouds are entrained in this wind then the speeds of the cold clouds can be at the most equal to $v_{\rm wind}$. This result is consistent with observed outflow speeds in post-starburst galaxies, ULIRGs and Low-ionization quasars at intermediate to high redshifts (e.g. Tremonti et al., 2007; Sturm et al., 2011). We have derived a general expression for the terminal speed of the wind from the NFW halo which can be written as $v_\infty = (4v_\star^2 + 6(\Gamma - 1)v_\bullet^2 - 4v_s^2)^{1/2}$, where $v_\star$ is the contribution from SNe and the term with $v_\bullet$ stands for the momentum injection from AGN. According to our results 1000 $\mathrm{km \ s^{-1}}$ is an upper limit for the starburst driven winds while in case of AGN driving which is possible in high mass galaxies only, the velocities always exceed 1000 $\mathrm{km \ s^{-1}}$. We note here that this limit holds for large scale escaping outflows for all galaxies; however there may be exceptional cases where the system is going through a period of extreme star formation, and even without AGN, the wind speed at a few kpc can be more than 1000 $\mathrm{km \ s^{-1}}$ (Diamond-Stanic et al., 2012). These episodic winds are likely to be driven by the radiation from galaxy as the galaxy becomes highly luminous due to extreme star formation (Sharma et al., 2011).

We have also shown that our results can explain the observed trends of stellar to halo mass ratio. We find that the stellar mass scales with the halo mass as $M_\star \propto M_h^{0.26}$ at the higher mass end and $M_\star \propto M_h^{1.67}$ at the lower mass end. The slope at higher mass end agrees with the observations and abundance matching results. We find that the large scatter in observational data at the lower mass end is due to the fact that the efficiency of energy injection is different in different galaxies. We would like to mention here that we have used a simple recipe to calculate the stellar mass corresponding to a particular halo mass using the outputs from our wind models. Implementing feedback recipes from our wind models into a full semi analytical work is beyond the scope of this study. Also we have assumed spherical symmetry for our calculation which is justified considering the large length scale (~ 100 kpc) of these outflows. However in the vicinity of the disk the effect of gravity due to a flattened system may be important as explored using a self-similar model in Bardeen & Berger (1978). We leave the problem of finding streamlines in a cylindrical geometry for these outflows to a future work.

We note that the reprocessed IR radiation is sufficient to drive strong outflows from high mass galaxies and the resulting feedback is enough to explain the mismatch between stellar mass and halo mass at high mass end. This is important as one need not to rely on UV radiation which is supposed to be attenuated quickly within a small distance from the center.

The injection of energy and mass in our model occurs in the central region. However, recent observations show the evidence of outflows emerging from individual star clusters which may be situated away from the center of the galaxies (e.g. Schwartz et al., 2006). It becomes however analytically complicated to take into account the contribution from these clusters and combine it with the effects of a central AGN. It is however clear that effects of the feedback would be higher if mass and energy injection occurs even beyond the central region and from a large number of clusters.

The coupling between gas and dust is shown to be mediated via momentum coupling. However, one may question the survival of dust grains. For this we refer to the observational evidence for dust in the spectra of AGNs, which shows that the dust does survive and it may do so by residing in small clumps around AGN as discussed in Krolik & Begelman (1988).

We have considered momentum transfer from AGN radiation in optically thin limit. In actual practice the situation can be quite complicated and it may not be exactly accurate to use a constant Γ. We hope that the simulations of winds with full radiation transfer covering from small to large length scales will be able to verify the simple ideas presented here. We have used a relation between the black hole mass and the dark matter halo mass. We have projected this relation backward in time using scalings of NFW parameters with redshift. There are observational evidence that black hole masses at high redshifts are generally higher, however it is hard to predict the correct scaling of black hole mass with redshift as the formation and growth of black holes is a complicated problem in itself.

We have not considered the effects of radiative cooling in the present work. Radiative cooling is important for the thermodynamics of the outflow. The CC85 solution with implementation of cooling has been studied in the past (Silich et al., 2004; Tenorio-Tagle et al., 2007; Wünsch et al., 2011; Silich et al., 2011). These calculations conclude that cooling (if not catastrophic) does not affect the velocity and density but causes the temperature to decay more rapidly. Wind solutions with cooling can not be worked out analytically for general values of parameters and one has to use the numerical computation, for particular cases. We have discussed the hot phase of the outflows which is tractable using analytic hydrodynamics. However, in actual practice the physics of hot, cold and molecular phase of galactic outflows might be tangled to each other . The study of all these components demands state of the art numerical simulations.

To summarize, we have found analytical solutions for SNe and AGN driven winds from realistic dark matter halo. Our results show that the two feedback processes operate effectively at two ends of the galaxy luminosity function as expected. The wind velocities for escaping winds resulting from our calculations explains a variety of observations. We find that AGN can drive the gas to speeds $\gtrsim 1000\,\mathrm{km\ s^{-1}}$. We find an intermediate mass range in which the outflows can be highly suppressed and for these halo masses the gas can not escape into the IGM. However, the gas is still driven to large distances within the halo. This result explains the recent observations of gas reservoirs in our Galaxy and other galaxies. Using the results of our analytical models, we have derived a stellar mass to halo mass relation using simple recipes. We find the derived $M_\star$–M_h relation matches the results of observations and halo abundance matching.

Chapter 6

Signature of Outflows in Strong Mg II Absorbers in Quasar Sightlines

Based on :

Sharma, M., Nath, B. B. & Chand, H. 2013, MNRAS, 431, L93

Absorption systems in the spectra of quasars are generally termed as 'intervening' if the velocity offset relative to quasar is greater than 5000 km s^{-1}. *These absorbers are classified as strong systems if the equivalent width (*W_r*) is larger than 1.0 Å, otherwise they are called weak MgII systems. It is generally believed that the strong MgII systems arise when the quasar line of sight passes through a galaxy. This hypothesis, although commonly agreed upon, has been tested to be true only for roughly* ~ 10 *% cases, for which a quasar-galaxy pair has been located. Another argument which is generally given to support the intervening system hypothesis is the large velocity offsets of these systems from quasar redshifts. However, one may argue that even such high velocities are possible if the UV light from quasar drives strong dusty outflows, whose velocity can be as large as* $\sim 0.1\ c$. *In this situation the MgII systems may arise in these outflows. This interesting postulate may be tested by studying the correlation between the quasar luminosity and the velocity offset of MgII system. We attempt this problem in the present chapter.*

Main results

- We find that the velocity offset (β) of strong Mg II absorber systems in quasar spectrum is correlated with the bolometric luminosity ($L_{\rm bol}$) of the quasar and the median value of β for absorbers in a particular quasar luminosity bin, follows the scaling $\beta \propto L_{\rm bol}^{1/4}$.
- The existence of β–$L_{\rm bol}$ correlation indicate that a significant fraction of absorbers are associated with the quasar themselves.
- We find that the correlation $\beta \propto L_{\rm bol}^{1/4}$ is also expected for the radiation (dust) driven outflows from quasar, launched from the innermost dust survival radius, which implies that a significant fraction of Mg II absorbers may arise in quasar radiation driven outflows.
- We note that the traditional criteria to denote an absorber as 'associated' if $\beta < 0.0167$, may not be adequate in view of our result that even higher values of β, all the way upto 0.4 are possible, if the Mg II absorbers arise in radiation driven outflow associated with the quasar.

6.1 Introduction

The study of Mg II absorption line systems in the spectra of quasars (QSOs) has been useful in detecting distant normal field galaxies situated close to the lines of sight of QSOs (Bergeron & Boissé, 1991; Steidel et al., 1994). Conventionally, all such absorbers with velocity $< 5000 \text{ km s}^{-1}$ relative to the background QSO are believed to be associated to the QSO itself ('associated systems') while those at larger velocity offset are believed to be entirely independent of background QSO. This general belief was questioned recently by the puzzling results on the abundance of strong Mg II absorber having equivalent width (W_r) more than 1.0 Å : (i) by Prochter et al. (2006b) where they found 2–4 time excess of strong Mg II absorber towards the γ ray burst (GRB) sources relative to QSO sight lines (see also Sudilovsky et al. 2007; Vergani et al. 2009; Tejos et al. 2009), and (ii) by Bergeron et al. (2011), where they found similar excess by a factor of about 2 (3 σ confidence) towards 45 blazar sight lines.

These counter-intuitive results, have inspired many alternative explanations, such as dust extinction towards QSO sight lines which can lower the apparent incidence rate of absorbers, or gravitational lensing which can increase it toward GRBs/blazars, but none have been found to explain the above discrepancies (Porciani et al., 2007; Ménard et al., 2008; Lawther et al., 2012). However the blazars, as a class, are believed to have relativistic jet pointed close to our line of sight. Bergeron et al. (2011) speculated that such powerful jets in the blazars are capable of sweeping sufficiently large column densities of gas (up to 10^{18}–10^{20}cm^{-2}) and accelerating such clouds to velocities of order $\sim 0.1c$, thereby possibly accounting for the excess of Mg II absorption systems towards blazars in comparison with QSOs. However, such an excess in number of Mg II absorbers per unit redshift (dN/dz) was not confirmed in the analysis of flat-spectrum radio quasars (FSRQs) by Chand & Gopal-Krishna (2012), though FSRQs also possess powerful jets similar to blazars, which they reconciled with the above hypothesis of relativistically ejected absorbing clouds, by suggesting that perhaps due to larger angle from the line of sight (unlike blazars with smaller angle), these accelerated clouds might not intersect the line-of-sight in the case of FSRQs. Using a larger sample size of 95 GRB (including 12 GRB from Prochter et al. 2006b), Cucchiara et al. (2012) did not confirm the original enhancement found in the case of GRB by Prochter et al. (2006b), though a signature of mild excess of about 1.5 times was noticed for strong Mg II absorption systems, albeit with only a low confidence level of 90%.

The firm conclusion for jet based above excess still await the realistic numerical modelling of jet-ambient gas interaction especially for the excess seen towards blazars (about a factor of 2) and CDQs (about 10%) (Joshi et al., 2013) vis-a-vis normal QSOs. However an alternative scenario, which could be more plausible, is the dust or radiation driven outflows (e.g. Scoville & Norman, 1995). For instance, if there is some contribution to dN/dz of strong Mg II absorber from these outflows, then one will expect that AGN luminosity should have statistical correlation with the velocity offset of the strong Mg II absorber relative to the background AGN, which is usually defined by,

$$\beta = \frac{(1+z_{\rm qso})^2 - (1+z_{\rm abs})^2}{(1+z_{\rm qso})^2 + (1+z_{\rm abs})^2} \tag{6.1}$$

where $\beta = v/c$, $z_{\rm qso}$ is the emission redshift of the QSO and $z_{\rm abs}$ is the absorption redshift of the Mg II system.

In this chapter, we report a correlation between the β of strong Mg II absorbers and the bolometric luminosity ($L_{\rm bol}$) of QSOs, using the strong Mg II absorber catalogue by Lawther et al. (2012). We also propose an explanation for this correlation which draws upon radiation driven outflow models. In §6.2 we describe the sample of strong Mg II absorbers and our selection criteria. In §6.3 we present our results and a theoretical model of radiation driven outflows. In §6.4 we study the fractional number counts of absorbers, and discuss our results in §6.5.

6.2 Description of the sample

We consider a sample of 10367 strong Mg II absorbers with equivalent width $W_r(2796) >$ 1Å belonging to 9144 QSOs, from the recent compilation by Lawther et al. (2012) based on 105783 QSOs of SDSS DR7 (Abazajian et al., 2009; Schneider et al., 2010). However, the range of β varies with $z_{\rm qso}$, and the observed wavelength range of the spectrum. Therefore, in order to make the sample unbiased, firstly, we have considered a SDSS spectral range from 4000-9000 Å which is a little narrower (by about 100 Å) than the actual one. We then applied the following four selection filters.

1. We removed 773 broad absorption line (BAL) QSOs from our above sample to avoid any contamination in our analysis by BAL features which has resulted in the removal of corresponding 931 strong Mg II absorbers.

2. For all the quasars having $z_{\rm qso} > 2.21024$, the Mg II emission line will fall above 9000 Å, which is our conservative upper limit on wavelength of SDSS spectrum. As a result, SDSS spectra for such sources will not allow any detection of strong Mg II doublet falling in the redshift range between 2.21024 up to $z_{\rm qso}$. Therefore to avoid this observational bias, we excluded all sources having $z_{\rm qso} \geq 2.21024$ from our sample,

which resulted in the removal of 43 QSOs having 52 strong Mg II absorbers.

3. Another filter was applied to avoid the observational bias which might result from the lower wavelength limit, viz 4000 Å, in the SDSS spectra. In our analysis we aim to see any correlation of luminosity with velocity offset up to about 0.4c. However for 4000 Å considered as the conservative starting wavelength of our spectra, $z_{\rm qso} = 1.185$ will be the minimum redshift, which allows us to detect Mg II absorber (if any) at least up to a velocity offset of $0.4c$. Therefore, we have removed 1461 sightlines with $z_{\rm qso} < 1.185$ having 1544 strong Mg II absorbers in their spectra.

4. After applying the above mentioned redshift cuts, we are left with the systems with $2.21024 > z_{\rm qso} \geq 1.185$. In these intermediate redshift systems, the β value can be larger than 0.4, which in principle may give rise to a bias of higher β with increasing $z_{\rm qso}$. Hence we also remove all the absorbers with $\beta > 0.4$ from the remaining sample which amounts to exclusion of 1523 absorbers along 1439 sightlines. One should note that $\beta = 0.4$ is chosen because if we keep β value less or greater than this, then the sample is significantly reduced. Another motivation as will be clear in the coming sections, is that $\beta \sim 0.4$ is an upper limit for the radiation (dust) driven outflows.

Finally, we are left with 6317 strong Mg II systems along 5682 QSOs in the selected redshift range. Bolometric luminosities for the QSOs in SDSS DR7 are calculated in a recent study by Shen et al. (2011). We cross matched the QSOs in our sample, with the catalogue described in Shen's paper to obtain the bolometric luminosity. We then removed two more absorbers whose QSO luminosities were $< 10^{45}$ erg s^{-1}. Our final bias free sample consists of 6315 strong Mg II systems with luminosity range $10^{45.5} < L_{\rm bol} \leq 10^{47.8}$ erg s^{-1}, with redshift range $1.185 \leq z_{\rm qso} < 2.21024$, and with the velocity offset range of $0 < \beta c \leq 0.4c$. In Figure 6.1, the blue dashed line represents the distribution of strong Mg II absorbers in SDSS-DR7, compiled by Lawther et al. (2012), and the black solid line is the final sample selected for this study.

6.3 Correlation between β and $L_{\rm bol}$: signature of radiation driven outflow

In order to test the dependence of β on luminosity, we divide the sample in bins of bolometric luminosity. Most of the absorbers (5651 out of 6315) belong to QSO sightlines having a luminosity range 10^{46}–10^{47} erg s^{-1}. We divide these 5651 systems into four bins of bolometric luminosity. We also have two more bins, one for $L_{\rm bol} < 10^{46}$ erg s^{-1}, and another

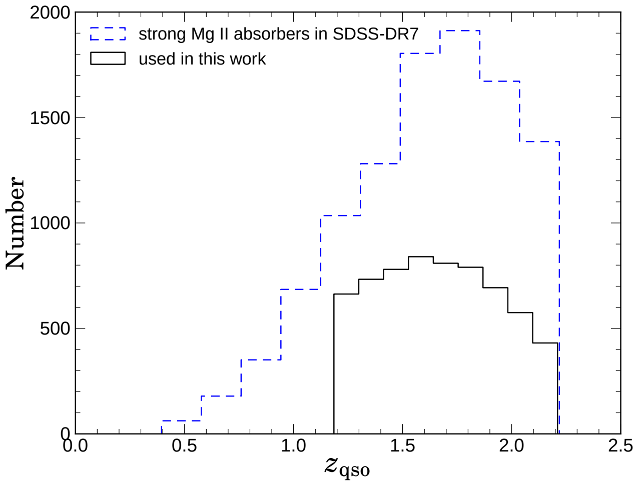

Figure 6.1: Histograms with $z_{\rm qso}$ of the samples of strong Mg II absorbers in SDSS-DR7. The blue dashed line is for 10367 strong absorbers compiled by Lawther et al. (2012). The black solid line represents the sample used in this work.

with $L_{\rm bol} > 10^{47}$ erg s^{-1}, the first having 27 systems and the second with 637 systems.

Consider the case of the absorbers being distributed uniformly in the allowed range of $z_{\rm abs}$ (which in turn is determined from the allowed range of β), then the median value of β should be independent of $z_{\rm qso}$. We can prove this statement as follows.

From equation (6.1), we know that β depends on the difference of $(1+z_{\rm qso})$ and $(1+z_{\rm abs})$. For the maximum allowed value of $\beta = 0.4$ in this study, the lower limit of $z_{\rm abs}$ can be obtained from equation (6.1), and can be written as, $z_{\rm abs}^{\rm min} = (C-1) + Cz_{\rm qso}$, where C is a constant whose value is 0.65 for $\beta = 0.4$. The median value of absorber redshift ($z_{\rm abs}^{\rm med}$) is the solution of following equation,

$$\int_{z_{\rm abs}^{\rm min}}^{z_{\rm abs}^{\rm med}} \frac{dN}{dz} dz = \frac{1}{2} \int_{z_{\rm abs}^{\rm min}}^{z_{\rm qso}} \frac{dN}{dz} dz \tag{6.2}$$

where dN/dz is the number of Mg II absorbers per unit redshift. If the absorbers are distributed uniformly and the quantity dN/dz is constant, then from equation (6.2) we get, $z_{\rm abs}^{\rm med} = ((C-1) + (C+1)z_{\rm qso})/2$. Using equation (6.1) we find the corresponding median value of β, which is $\beta_{\rm med} \approx 0.19$, independent of $z_{\rm qso}$. Hence, irrespective of the distribution of $z_{\rm qso}$ in a luminosity bin, the median value of beta should be same in all luminosity bins. Next we set out to test this hypothesis for our sample. We calculate the median, the lower 25 percentile and the upper 25 percentile of data in each of the above mentioned six luminosity bins. We plot the median with circles, and the upper and lower percentiles as the end points of vertical dotted bars in Figure 6.2.

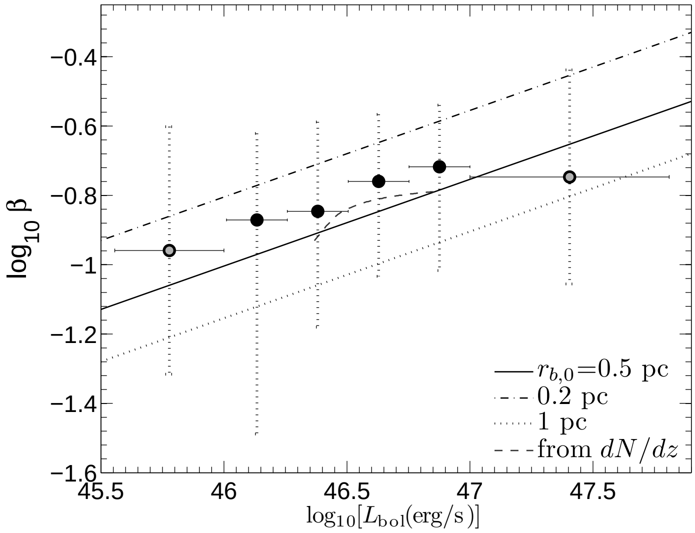

Figure 6.2: Correlation between the bolometric luminosity of the QSO and β of Mg II absorber. The circles represent the median of data in a particular luminosity bin. The upper and lower extreme of the dotted vertical lines give the location of upper and lower 25 percentile, respectively. Sizes of the luminosity bins are shown by the horizontal bars. The solid, dotted and dash-dotted line represent the theoretical model discussed in §3.1.

Interestingly, we find that the median is not constant. The data shows a correlation of β with the $L_{\rm bol}$. The 5651 absorbers systems with $10^{46} \leq L_{\rm bol} \leq 10^{47}$ erg s^{-1}, which form the mainstay of the sample show a power law increase of β with $L_{\rm bol}$, with a slope of $\sim 1/4$. Increase of median value of β with the bolometric luminosity, proves that the distribution in each bin is not uniform random. This fact is also hinted in the evolution of dN/dz with $z_{\rm abs}$ (Zhu & Ménard, 2013). Using the evolution in dN/dz for our sample, we evaluated the expected relation between the median value of β and $z_{\rm qso}$ from equation (6.2). We then converted it to the corresponding relation between β and luminosity by using the best fit relation between $z_{\rm qso}$ and luminosity, a characteristic of magnitude limited survey such as SDSS. We have shown this relation using a dashed curve in Figure 6.2. Although the dashed curve does show some evolution, but it is clear that it cannot fully explain the observed β–$L_{\rm bol}$ correlation.

Which physical processes can give rise to non-uniformity of absorber distribution? The evolution in dN/dz has been attributed to the evolution in global star formation rate (Zhu & Ménard, 2013), although without any concrete evidence. Also, observations of intervening galaxies show a small covering fraction (≤ 0.3) for strong Mg II absorbers ($W \geq 1$ Å) (Nielsen et al., 2012; Chen et al., 2010). Here we explore an alternate based on outflows associated with QSOs, which can give rise to non-uniformity of incidence of absorbers. As we explore in next section, the relation $\beta \propto L_{\rm bol}^{1/4}$, is a natural consequence of QSO radiation driven outflows.

6.3.1 Absorbers as radiation driven outflows

Radiation driven outflows have been invoked repeatedly in literature to explain the co-evolution of black hole and bulge, to explain the accretion disc winds (e.g. Proga et al., 2000) and galactic winds (e.g. Murray et al., 2005; Sharma et al., 2011). We consider here the radiation driven outflows, where the photons scatter the dust grains and impart their momentum to dust. The dust in turn is collisionally coupled to the gas, and the momentum is uniformly distributed to the dust and gas mixture. In this scenario, the motion of dust and gas mixture surrounding the QSO is governed by the following equation,

$$v\frac{dv}{dr} = \frac{\kappa L_{\rm uv}}{4\pi r^2 c} - \frac{GM_\bullet}{r^2} - \frac{d\Phi}{dr} \tag{6.3}$$

where $M_\bullet$ is the mass of the black bole and Φ is the dark matter halo potential. $L_{\rm uv}$ is the integrated UV luminosity and for QSOs where the main emission is in high frequency bands, luminosity over UV and EUV bands is roughly half of the bolometric luminosity ($L_{\rm uv} \sim 0.5 L_{\rm bol}$)(Risaliti & Elvis, 2004). κ is the frequency averaged opacity for the scattering and absorption of UV photons by dust grains. For wavelength of photon $< 0.3\ \mu$m, the κ for a dust and gas mixture ranges from 200 to as large as 1000 cm^{2}g^{-1} (Li & Draine, 2001). We take a value $\kappa = 500$ cm^{2}g^{-1}, which roughly serves as an average effective value of opacity. We can integrate equation (6.3) to obtain the following expression for velocity

$$v^2 = \frac{\kappa L_{\rm bol}}{4\pi c}\left(\frac{1}{r_b} - \frac{1}{r}\right) - 2(\Phi(r) - \Phi(r_b)) \tag{6.4}$$

where r_b is the launching radius of the outflow. In the case of radiation pressure on dust grains, the opacity is generally quite high and hence the radiation force is many times larger than the gravity, therefore the gravitational force can be neglected. At a large distance the velocity attains the following terminal value

$$v_\infty \simeq \left(\frac{\kappa L_{\rm bol}}{4\pi c\, r_b}\right)^{1/2} \tag{6.5}$$

The base radius (r_b) for launching these outflows is an important factor and it should be the minimum distance at which the dust grains can survive. Studies on dust survival yield following relation between the sublimation radius of the dust grains and the luminosity of the AGN (Mor & Netzer, 2012),

$$r_b = R_{\rm sub} \sim r_{b,0} \left(\frac{L_{\rm bol}}{10^{46}\ {\rm erg\ s^{-1}}}\right)^{0.5} . \tag{6.6}$$

The value of $r_{b,0}$ is 0.5 pc for graphite grains and 1.3 pc for the silicate grains. Substituting equation (6.6) into (6.5), we obtain the following expression for wind terminal speed,

$$v_{\infty} \sim 0.1c \left(\frac{\kappa}{500\ \mathrm{cm}^2\ \mathrm{g}^{-1}} \right)^{1/2} \left(\frac{L_{\mathrm{bol}}}{10^{46}\ \mathrm{erg\ s}^{-1}} \right)^{1/4} \left(\frac{r_{b,0}}{0.5\ \mathrm{pc}} \right)^{-1/2} \tag{6.7}$$

We note that this mechanism has previously been discussed in the context of AGN outflows by Scoville & Norman (1995). These authors also arrived at similar terminal speed for a radiation driven outflow.

We plot this scaling to compare with the observed correlation of β and L_{bol} in Figure 6.2. The dash-dotted, solid and dotted line in Figure 6.2 correspond to $r_{b,0} = 0.2, 0.5, 1.0$ pc respectively. We find that this simple theoretical model fits the observed correlation pretty well, which indicates that the absorber systems are likely to be radiation(dust) driven outflows.

One is then tempted to ask as to how these outflows fit in the unification schemes of AGN. We find that the launching radius of the outflows is the dust sublimation radius, which is also the inner radius of the dusty torus. Inside the torus, the UV photons are quickly reprocessed into IR. Although the IR photons can also drive outflows (Dorodnitsyn et al., 2011; Sharma & Nath, 2013), however the speeds would not be large, as the IR to dust scattering cross section is more than an order of magnitude smaller than in UV. One possible way to reconcile this is the following.

Let us suppose that the outflows do not plough through the main body of the torus, but consist of material lifted from the outer surface of the torus. In that case, as the torus material is dilute and highly porous at its periphery, the UV photons can in principle travel a large distance without being attenuated and impart their momentum to gas and dust mixture lifted from the outer surface of the torus. More specifically, in the picture presented in Elvis (2000), the region which we are considering should take place between the BAL envelope and the torus. We note that, this scenario not only gives rise to large velocity outflows, but it may also account for the small fraction ($\lesssim 0.1$) of the QSOs which show these absorbers owing to the fact that the region allowed for the outflows (periphery of the torus) occupies a very small fraction of the viewing angle.

6.4 Fractional number of absorbers

Next we study the dependence of fractional number counts of absorbers as a function of QSO luminosity. We define the fractional number count as below,

$$\mathrm{Fractional\ number\ count} = \frac{\mathrm{Number\ of\ absorbers\ found}}{\mathrm{Number\ of\ QSOs\ searched\ in\ a\ bin}}\,. \tag{6.8}$$

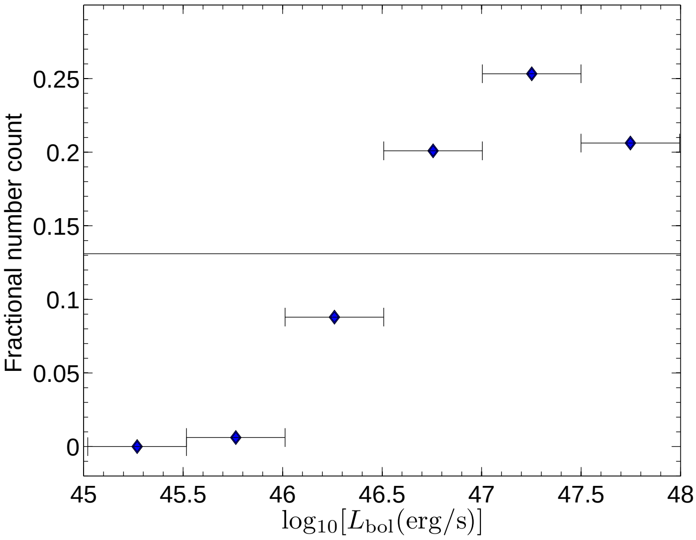

Figure 6.3: The fractional number count as a function of bolometric luminosity is shown using filled diamonds, and the size of the luminosity bin is shown by the horizontal bar. Thin horizontal line represents the average value of fractional number count over the entire sample.

Again, we limit our analysis to the spectral region with $\beta < 0.4$. From our sample, as described in §2, we can easily estimate the "Number of absorbers found" in a given luminosity bin, having $\beta < 0.4$. However to find the corresponding "Number of QSOs searched in a bin", we also need to count those QSOs in the parent sample of SDSS-DR7 from which the QSOs with Mg II absorbers are selected. We use the parent catalogue from Shen et al. (2011) of which the sample used in this work is a subset. Therefore, we estimate the "Number of QSOs searched in a bin" by using non-BAL QSOs from Shen et al (2012) catalogue, which satisfy the redshift criteria $1.185 \le z_{\rm qso} < 2.21$, to ensure the absence of any observational biases (see §2).

We plot the fractional number count as a function of luminosity ($L_{\rm bol}$) in Figure 6.3. The values are shown by filled diamonds whose x-coordinate is the centre of each luminosity bin. We also show the overall average of the sample using a horizontal line, whose value is ~ 0.1. We find that the fraction increases steeply with increasing QSO luminosity and reaches a maximum roughly for $L_{\rm bol} \sim 10^{47}$ erg s^{-1}. For $L_{\rm bol} > 10^{47.5}$ erg s^{-1} there is a mild decrease with luminosity, however this decrease is uncertain as in this bin, we have many apparently faint high redshift quasars, for which the signal to noise criterion removes large chunks of spectra and the corresponding absorbers (D. Lawther pvt. comm.). We note that the fractional number of absorbers has a contribution from outflowing and intervening systems, which we can not separate here.

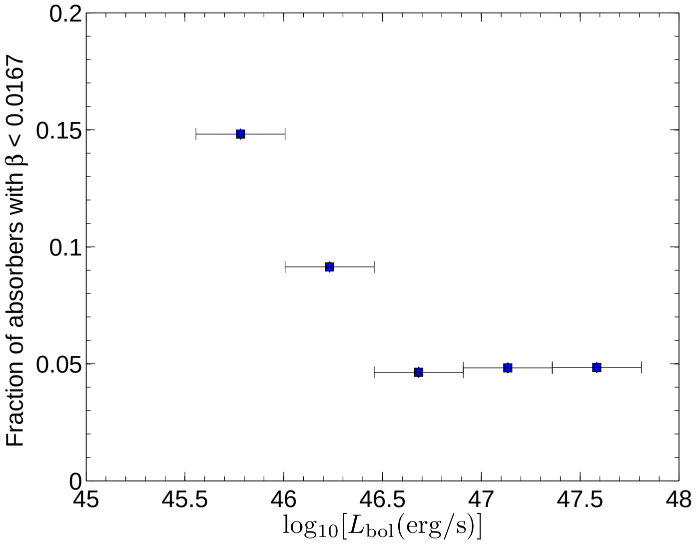

Figure 6.4: Ratio of absorbers with $\beta < 0.0167$ to the total number of quasars in a particular luminosity bin is plotted against the bolometric luminosity. The horizontal bar represents the size of the luminosity bin.

6.5 Discussion

We would like to emphasize an important point in connection with our result. There is a general consensus in the literature, which goes along the line that the absorbers which have $\beta < 0.0167$ ($v < 5000$ km s^{-1}), are associated with the QSO and with β higher than this represent the intervening media. We stress here that this criterion is not adequate to denote the associated systems, and the true associated systems can also have $\beta > 0.0167$, e.g. the QSO driven high velocity outflows considered here.

To illustrate this, we plot in Figure 6.4, the ratio of absorbers with $\beta < 0.0167$ to the total number of absorbers in a particular luminosity bin as a function of bolometric luminosity. One can clearly see that lower β are possible for only lower luminosity, and vice versa. Firstly, the figure once again confirms that the velocity offset β is correlated with luminosity, because low β absorbers appear along the sightlines of low luminosity QSOs. Secondly, this plot, in conjunction with the correlation of β with $L_{\rm bol}$, shows that the systems which are really '*associated* ' with the QSOs are spread all the way from $\beta = 0.0$ to 0.4.

Our results call for a study to separate out the truly associated (outflowing) systems and the intervening ones. Of course, one tedious way to do this is to locate the intervening galaxies in each quasar sightline, however yet another way can be through the detailed study of line shapes and features arising from outflows and intervening material. We look forward to such a study in the future.

There is another implication of the observed dependence of fractional number count of absorbers on QSO luminosity. If one considers a sample of a particular type of QSOs that covers a restricted luminosity range, then the relative number of absorbers may differ for different samples, and be different from the overall average. If we consider the right side of Figure 6.3, corresponding to $L_{\rm bol} > 10^{46.5}$ erg/s, there the fractional number counts are roughly double of the overall average value of 0.1. We note that recent observations of ~ 45 blazars (Bergeron et al., 2011) report an excess of Mg II absorbers relative to that in QSOs. We speculate here that this excess may also arise from the fact that the blazar sample is small, and it may be possible that it is biased towards higher luminosity, where the fractional number count is larger. It is possible that if the analysis is repeated with a larger sample of blazars then the excess may fade away. In fact, a similar conclusion has been reached for a sample of FSRQs and 7156 lobe and core dominated QSOs where in both cases one finds only a mild excess (Joshi et al., 2013). In this regard we bring a recent paper by Cucchiara et al. (2012) to the attention of the reader, regarding the excess seen towards GRBs, where with a large sample of GRBs the puzzle of Mg II incidence rate indeed disappears, and one does not find any excess.

In summary, we have found a correlation between the velocity offset of strong Mg II absorbers and the luminosity of QSOs. The velocity offset (βc) has been found to increase with the luminosity with a power law index $\sim 1/4$. We have found that radiation driven outflows from QSOs can give rise to such a dependence of β on $L_{\rm bol}$. These findings lead us to conclude that a significant fraction of strong Mg II absorbers (even with $v > 5000~{\rm km~s^{-1}}$) along QSO sightlines may be the AGN driven outflows.

Chapter 7

Conclusion

In this thesis, we have studied galactic outflows analytically and using simulations, and addressed the issues such as the terminal speed of outflows, their structure and rotation, relative importance of various driving mechanisms, effect of gravitational field of the dark matter halo and the effect of outflows on the stellar content of galaxies. We have explored various outflow driving mechanisms such as the radiation pressure on dust grains the ram pressure due to hot wind, SNe energy injection, momentum injection due to an AGN and the cosmic rays. We have obtained interesting results which explain a variety of observations such as (I) the correlation between the outflow speed and the galaxy circular speed, (II) the relative importance of ram and radiation pressure and the importance of cosmic rays (III) observed threshold of star formation surface density ($\Sigma_{\rm SFR} \sim 0.1$ M$_\odot$ yr^{-1} kpc^{-2}), for galaxies to show signatures of outflows, (IV) high velocity ($> 10^3$ km s^{-1}) outflows because of the presence of an AGN, (V) gas reservoirs in the halos of galaxies (VI) ratio of the stellar to halo masses in galaxies. We also carry out an observational study in which we search for a correlation between the quasar luminosity and the velocity offset of strong Mg II absorbers in quasar spectra, and explore the possibility that a significant fraction of strong Mg II absorbers may arise in outflows driven by quasar radiation. We summarize our work below and discuss our results with a future perspective.

Radiation Driven Outflows from a Disc Galaxy

In chapter 2, we have studied gaseous outflows along the pole of a galaxy, driven by radiation pressure on dust grains. We consider the gravitational and radiation forces due to a disc with surface brightness (I) and surface mass density (Σ). We have included the gravitational effect of bulge and dark matter halo and found that the existence of such an outflow implies a maximum value of $\sim 10^{-2}$ for disc mass-to-light ratio. We have shown that the terminal wind speed is proportional to the disc rotation speed in the limit of a cold gaseous outflow. Using the mean opacity of dust grains and the evolution of the luminosity of a simple stellar population for instantaneous star formation, we have shown that the ratio of the wind terminal speed (v_∞) to the galaxy rotation speed (v_c) is roughly $v_\infty/v_c \sim 3$. We note that the escape speed in NFW halo is $\approx 3v_c$, therefore, the radiation driven outflows can easily escape into the IGM and enrich it with metals. Also the correlation of wind speed with the galaxy circular speed explains recent observations (Martin, 2005; Rupke et al., 2005b). Interestingly, similar correlations, when used in simulations of galaxy formation as a feedback recipe, can explain the galaxy luminosity function as well as the enrichment of IGM (Oppenheimer & Davé, 2006).

Structure and Rotation of Radiation driven outflows

In chapter 3, we have carried out a 2-D hydrodynamic simulation of radiation driven galactic wind from a disc with exponentially varying surface brightness and mass density, and total mass of the galaxy similar to that of the Milky Way, using the TVD hydrodynamic code developed by Ryu et al. (1993); Kang et al. (1994). We have taken into account the total gravity of a galactic system that consists of a disc, a bulge and a dark matter halo. We have found that the combined effect of gravity and radiation pressure from a realistic disc drives the gas away to a distance of ~ 5 kpc in ~ 37 Myr for typical galactic parameters. The outflow speed increases rapidly with the disc Eddington parameter $\Gamma_0 (= \kappa I/(2cG\Sigma))$ for $\Gamma_0 \geq 1.5$, and the rotation speed of the outflowing gas is $\lesssim 100$ km s^{-1}. The wind is confined in a cone which mostly consists of low angular momentum gas lifted from the central region.

Our results presented show that the outflowing gas within the central region of a few kpc tends to stay close to the pole, and does not move outwards because of its low angular momentum. This makes the outflow somewhat collimated. Although outflows driven by SNe heated hot wind also produces a conical structure (e.g. Fragile et al., 2004) emanating from a breakout point of the SN remnants, there is a qualitative difference between this case and that of radiatively driven winds as presented in our simulations. While it is the pressure of the hot gas that expands gradually as it comes out of a stratified atmosphere, in the case of a radiation driven wind, it is the combination of mostly the lack of rotation and almost vertical radiation driving force in the central region that produce the collimation effect. We also note that the conical structure of rotation in the outflowing gas is similar to the case of outflow in M82 (Greve, 2004), where one observes a diverging and rotating periphery of conical outflow.

From our results of the exponential and rotating disc model, we find the wind comprising of low-angular momentum gas lifted from the disc. It is interesting to note that recent simulations of supernovae driven winds have also claimed a similar result (Governato et al., 2010). Such loss of low angular momentum gas from the disc may have important implication for the formation and evolution of the bulge, since the bulge population is deficient in stars with low specific angular momentum. Binney et al. (2001) have speculated that outflows from disc that preferentially removes low angular momentum material may resolve some discrepancies between observed properties of disc and results of numerical simulations.

Ram Pressure, Radiation Pressure and the Cosmic Ray Driving

To explore the relative importance of various driving mechanisms, in chapter 4 we have studied gaseous clumpy outflows from disc galaxies driven by the combined effects of ram pressure and radiation pressure. Taking into account the gravity due to disc, bulge and dark matter halo, and assuming continuous star formation in the disc, we have found that radiation or ram pressure alone is not sufficient to drive escaping outflows, and both processes contribute. In the parameter space of SFR and circular speed (v_c) of galaxies, the criteria for the outflows can be written as, $\mathrm{SFR}^{3/4}_{10\ \mathrm{M}_\odot/\mathrm{yr}}\, v^{-2}_{c,140\ \mathrm{km/s}} > 1$. We note that the above criteria implies that the winds should occur in galaxies with star formation surface density roughly $\Sigma_{\mathrm{SFR}} \gtrsim 10^{-1}$ M$_\odot$ yr^{-1} kpc^{-2}, and thus explain the observational threshold for winds. We further note that the wind speed in galaxies with rotation speed $v_c \leq 200$ km s^{-1} and SFR ≤ 100 M$_\odot$ yr^{-1}, has a larger contribution from ram pressure, and that in high mass galaxies with large SFR, radiation from the disc has a greater role in driving galactic winds. For galaxies satisfying our outflow criteria, the ratio of wind speed to circular speed can be approximated as, $\frac{v_w}{v_c} \sim 10^{0.7} \left[\frac{\mathrm{SFR}}{50\,\mathrm{M}_\odot/\mathrm{yr}}\right]^{0.4} \left[\frac{v_c}{120\,\mathrm{km/s}}\right]^{-1.25}$. This conclusion is borne out by observations of galactic winds at low and high redshift and also of the circumgalactic gas. We also estimate the mass loading factors under the combined effect of ram and radiation pressure, and show that the ratio of mass loss rate to SFR scales roughly as $v_c^{-1}\Sigma_g^{-1}$, where Σ_g is the gas column density in the disc. Interestingly, similar power law dependence has also been found in simulations (Hopkins et al., 2012).

Our theoretical results explain the outflows in galaxies with $v_c \gtrsim 100\ \mathrm{km\ s}^{-1}$, SFR$\gtrsim 1$ M$_\odot$/yr, which covers the winds in dwarf starbursts, outflows in LIRGs (Heckman et al., 2000) and the recent observations of winds in ULIRGs (Martin, 2005; Rupke et al., 2005b; Weiner et al., 2009). This implies that cold outflows from these galaxies may indeed be driven by the combined action of ram and radiation pressure. We note that the faint dwarf galaxies in which Martin (1998) and Schwartz & Martin (2004) have reported outflows, do not satisfy our outflow criteria. In other words, if we calculate the star formation surface density for these galaxies we find that only a few of them satisfy $\Sigma_{\mathrm{SFR}} > 0.1$ M$_\odot$ yr^{-1} kpc^{-2}, which is the observational criteria for winds. This points to some other process, responsible for powering winds in these galaxies. One such process may be the cosmic ray streaming and resulting outflows (e.g. Ipavich, 1975; Samui et al., 2008; Uhlig et al., 2012). Recently, using SPH simulations of cosmic ray streaming, Uhlig et al. (2012) have shown that this mechanism can power the outflows in low SFR and low mass galaxies (shown by two pink bars in Fig. 4.6). We refer the reader to Appendix G of this thesis, where we have explored the cosmic ray driven outflows.

Hydrodynamic Study of SNe and AGN Driven Outflows

In chapter 5, We have worked out the steady state analytical solutions for winds from galaxies with NFW dark matter halo. We have considered winds driven by energy and mass injection from multiple supernovae (SNe), as well as momentum injection due to radiation from a central black hole. We have found that the wind dynamics depends on three velocity scales: (a) $v_\star \sim (\dot{E}/2\dot{M})^{1/2}$ describes the effect of starburst activity, with $\dot{E}, \dot{M}$ as energy and mass injection rate in a central region of radius R; (b) $v_\bullet \sim (GM_\bullet/2R)^{1/2}$ for the effect of a central black hole of mass $M_\bullet$ on gas at distance R and (c) $v_s = (GM_h/2\mathcal{C}r_s)^{1/2}$ which is closely related to the circular speed (v_c) for NFW halo, with r_s as the halo scale radius and $\mathcal{C}$ is a function of halo concentration parameter. Our generalized formalism, in which we treat both energy and momentum injection from starbursts and radiation from AGN, allowed us to estimate the wind terminal speed as, $v_\infty = (4v_\star^2 + 6(\Gamma - 1)v_\bullet^2 - 4v_s^2)^{1/2}$, where Γ is the ratio of force due to radiation pressure to gravity of the central black hole. Our dynamical model also predicts the following: (a) winds from quiescent star forming galaxies cannot escape from $10^{11.5} \le M_h \le 10^{12.5}$ $\mathrm{M}_\odot$ galaxies, (b) circumgalactic gas at large distances from galaxies should be present for galaxies in this mass range, (c) for an escaping wind, the wind speed in low to intermediate mass galaxies is $\sim$ 400–1000 km/s, consistent with observed X-ray temperatures; (d) winds from massive galaxies with AGN at Eddington limit have speeds $\gtrsim 1000$ km/s. We also determine the stellar to halo mass ratio of galaxies, following the scheme suggested in Granato et al. (2004) (see also Shankar et al. 2006). In this scenario, the ratio $[2v_\star^2 - (1-\Gamma)v_\bullet^2]/v_c^2$ dictates the amount of gas lost through winds. Used in conjunction with an appropriate relation between $M_\bullet$ and M_h, and an appropriate opacity of dust grains in infrared (K band), this ratio has the attractive property of being minimum at a certain halo mass scale ($M_h \sim 10^{12-12.5}$ $\mathrm{M}_\odot$) that signifies the cross-over of AGN domination in outflow properties from starburst activity at lower masses.

We note that the gravitational field of the dark matter halo causes the outflows to be confined inside the virial radius, which can explain the observation of circumgalactic material in galaxies (e.g. Tumlinson et al., 2011). Also recently, there have been observational indications that outflows with speeds greater than 1000 km/s in many Ultra Luminous Infra Red Galaxies (ULIRGs), are driven by AGN (Tremonti et al., 2007; Sturm et al., 2011). Therefore, we provide here a theoretical footing for this observational result. We also note that although the UV radiation from AGN is attenuated, still the IR photons (which are available in plenty) can drive powerful outflows. Using our results we have calculated the stellar to halo mass ratio of galaxies and found that stellar mass for massive galaxies scales as $M_\star \propto M_h^{0.26}$, and for low mass galaxies, $M_\star \propto M_h^{5/3}$. These scalings comply well with the observations and the results of halo abundance matching (Moster et al., 2010; Behroozi et al., 2010; Leauthaud et al., 2012).

Signatures of Outflows in Strong Mg II Absorbers in Quasar Sightlines.

In chapter 6 we have carried out an observational study to explore the possibility that Mg II absorbers in quasar sightlines are associated with quasar radiation driven outflows. For this we consider the quasar spectra in SDSS Data Release-7. We divided the data in the bins of luminosity of quasars and studied the correlation between velocity offset ($\beta = v/c$) of strong absorption systems and the bolometric luminosity ($L_{\rm bol}$) of quasars in SDSS-DR7. We have found that β shows a power law increase with $L_{\rm bol}$, with a slope of 1/4, and such a scaling of β with $L_{\rm bol}$ is expected for outflows driven by scattering of black hole radiation off dust grains and launched from the innermost dust survival radius. Our results indicate that a significant fraction of the strong Mg II absorbers, in the range of $\beta = 0.0$–0.4 may be associated with the quasars themselves.

It is generally believed that the absorbers which have $\beta < 0.0167$ ($v < 5000$ km s^{-1}), are associated with the QSO and with β higher than this represent the intervening media (e.g. Bergeron et al., 2011). We note that this criterion is not adequate to denote the associated systems, and the true associated systems can also have $\beta > 0.0167$. The correlation of β with $L_{\rm bol}$ which we have found, shows that the systems which are really '*associated* ' with the QSOs are spread all the way from $\beta = 0.0$ to 0.4. Our results call for a study to separate out the truly associated (outflowing) systems and the intervening ones. A different way to do this by locating the intervening galaxies in each quasar sightline, however yet another way can be through detailed study of line shapes and features arising from outflows and intervening material.

Appendices

A : Detailed derivation of wind equation

The continuity and momentum equations can be written as,

$$\frac{2}{r}+\frac{1}{\rho}\frac{d\rho}{dr}+\frac{1}{v}\frac{dv}{dr}=\frac{\dot{m}}{\rho v} \tag{1}$$

$$v\frac{dv}{dr}=-\frac{c_s^2}{\gamma}\left(\frac{1}{\rho}\frac{d\rho}{dr}\right)-\frac{1}{\gamma}\frac{dc_s^2}{dr}+f(r)-\frac{d\Phi(r)}{dr}-\frac{\dot{m}v}{\rho} \tag{2}$$

where $c_s^2=\gamma p/\rho$. Elimination of $\frac{1}{\rho}\frac{d\rho}{dr}$ from above two equations yields,

$$v\frac{dv}{dr}-\frac{c_s^2}{\gamma v}\frac{dv}{dr}=-\frac{1}{\gamma}\frac{dc_s^2}{dr}+\frac{c_s^2}{\gamma}\left(\frac{2}{r}-\frac{\dot{m}}{\rho v}\right)-\frac{\dot{m}v}{\rho}+f(r)-\frac{d\Phi(r)}{dr} \tag{3}$$

from energy equation (equation 5.3 in chapter 5) we have,

$$v\frac{dv}{dr}+\frac{1}{\gamma-1}\frac{dc_s^2}{dr}=\frac{q}{\rho v}-\frac{\epsilon(r)\dot{m}}{\rho v}+f(r)-\frac{d\Phi(r)}{dr} \tag{4}$$

where $\epsilon(r)=\frac{v^2}{2}+\frac{c_s^2}{\gamma-1}$. Elimination of $\frac{dc_s^2}{dr}$ from equation (3) and (4) results in,

$$\frac{v^2-c_s^2}{v}\frac{dv}{dr}=c_s^2\left(\frac{2}{r}-\frac{\dot{m}}{\rho v}\right)-(\gamma-1)\left(\frac{q}{\rho v}-\frac{\dot{m}\epsilon(r)}{\rho v}\right)+f(r)-\frac{d\Phi(r)}{dr}-\frac{\dot{m}v\gamma}{\rho} \tag{5}$$

Next we introduce the Mach number $\mathcal{M}=v/c_s$. We can write the following relations,

$$\begin{aligned} v\frac{dv}{dr} &= \frac{c_s^2}{2}\frac{d\mathcal{M}^2}{dr}+\frac{\mathcal{M}^2}{2}\frac{dc_s^2}{dr} \quad ; \\ \frac{1}{v}\frac{dv}{dr} &= \frac{1}{2\mathcal{M}^2}\frac{d\mathcal{M}^2}{dr}+\frac{1}{2c_s^2}\frac{dc_s^2}{dr} \end{aligned} \tag{6}$$

Using these relations in equation (4) and (5) we obtain,

$$\frac{dc_s^2}{dr} = \frac{\frac{q}{\rho v} - \frac{\epsilon(r)\dot{m}}{\rho v} + f(r) - \frac{d\Phi(r)}{dr} - \frac{c_s^2}{2}\frac{d\mathcal{M}^2}{dr}}{\frac{\mathcal{M}^2}{2} + \frac{1}{\gamma - 1}} \tag{7}$$

and

$$c_s^2 \frac{\mathcal{M}^2 - 1}{2\mathcal{M}^2}\frac{d\mathcal{M}^2}{dr} + \frac{\mathcal{M}^2 - 1}{2}\frac{dc_s^2}{dr} = \frac{2c_s^2}{r} - \frac{\dot{m}c_s^2}{\rho v} - \frac{(\gamma - 1)[q - \dot{m}\epsilon(r)]}{\rho v} + f(r) - \frac{d\Phi(r)}{dr} - \frac{\dot{m}v\gamma}{\rho} \tag{8}$$

Substituting equation (7) in (8) we get the following wind equation,

$$\frac{\mathcal{M}^2 - 1}{\mathcal{M}^2(\mathcal{M}^2(\gamma - 1) + 2)}\frac{d\mathcal{M}^2}{dr} = \frac{2}{r} - (1 + \gamma\mathcal{M}^2)\frac{\dot{m}}{\rho v} - \frac{\dot{m}(1 + \gamma\mathcal{M}^2)}{2\rho v}\left(\frac{\dot{E}/\dot{M}}{\epsilon(r)} - 1\right) + \frac{(\gamma + 1)\left[f(r) - \frac{d\Phi(r)}{dr}\right]}{2(\gamma - 1)\epsilon(r)} \tag{9}$$

Where $\dot{M} = \dot{m}V$ and $\dot{E} = qV$ in which V is the volume of injection region. This is the general form of wind equation with contributions from energy and mass injection, gravity and external driving force.

B : Subsonic part of SNe and AGN driven wind

Here we show the subsonic part of the solution for SNe and AGN driven wind. Apart from the energy and mass injection we take $f(r) = \Gamma GM_\bullet/r$ and $\Phi(r) = \Phi_\bullet(r) = -GM_\bullet/r$. From continuity equation we obtain $\rho v r^2 = \dot{m}r^3/3$. If we substitute this in energy equation we get,

$$\frac{d}{dr}\left[\frac{\dot{m}r^3}{3}\left(\frac{v^2}{2} + \frac{c_s^2}{\gamma - 1}\right)\right] + \frac{\dot{m}r^3}{3}\left(\frac{(1 - \Gamma)GM_\bullet}{r^2}\right) + \left[\frac{\dot{m}r^3}{3}\frac{d\Phi_{\rm NFW}}{dr}\right] = \frac{\dot{E}\,r^2}{V} \tag{10}$$

In the subsonic regime $r << r_s$. Therefore in this case the third term on left hand side which is due to NFW gravity can be neglected as shown below,

$$\left.\frac{\dot{m}r^3}{3}\frac{d\Phi_{\rm NFW}}{dr}\right|_{r<<r_s} = \frac{-\dot{m}GM_h r}{3\left[\ln(1 + c) - c/(1 + c)\right]}\left.\left(\frac{r/r_s}{1 + r/r_s} - \ln(1 + r/r_s)\right)\right|_{r<<r_s} \approx 0 \tag{11}$$

Neglecting the third term, ($\frac{\dot{m}r^3}{3}\frac{d\Phi_{\rm NFW}}{dr} \approx 0$) and integrating from zero to r we get,

$$\left.\left[\frac{\dot{m}r^3}{3}\left(\frac{v^2}{2} + \frac{c_s^2}{\gamma - 1}\right)\right]\right|_0^r + \left.\left(\frac{\dot{m}(1 - \Gamma)GM_\bullet r^2}{6}\right)\right|_0^r = \left.\frac{\dot{E}}{V}\frac{r^3}{3}\right|_0^r$$

$$\Rightarrow \qquad \epsilon(r) = \frac{\dot{E}}{\dot{M}} - (1-\Gamma)v_\bullet^2\frac{R}{r} = 2v_\star^2 - (1-\Gamma)v_\bullet^2\frac{R}{r} \tag{12}$$

where we have defined $v_\bullet = \sqrt{GM_\bullet/2R}$, a velocity characteristic of the black hole. At $r = R$ we obtain,

$$\epsilon(R) = \frac{\dot{E}}{\dot{M}} - (1-\Gamma)v_\bullet^2 = 2v_\star^2 - (1-\Gamma)v_\bullet^2 = 2v_{\rm crit}^2 \tag{13}$$

where $v_{\rm crit}$ is the velocity at the critical point. Substituting the expression for $\epsilon(r)$ and also $f(r) = \Gamma GM_\bullet/r^2$, $\Phi = \Phi_\bullet + \Phi_{\rm NFW}$, $\gamma = 5/3$ in wind equation (5.4) in chapter 5, we get,

$$\begin{aligned}\frac{\mathcal{M}^2-1}{\mathcal{M}^2(\mathcal{M}^2(2/3)+2)}\frac{d\mathcal{M}^2}{dr} &= \frac{2}{r} - \frac{3+5\mathcal{M}^2}{r} - \frac{(3+5\mathcal{M}^2)}{2\,r}\left(\frac{\frac{(1-\Gamma)R\;v_\bullet^2}{2\;r\;v_\star^2}}{1-\frac{(1-\Gamma)R\;v_\bullet^2}{2\;r\;v_\star^2}}\right) \\ &\quad -2\left(\frac{(1-\Gamma)R\;v_\bullet^2}{r^2\;v_\star^2}\right)\left(1-\frac{(1-\Gamma)R\;v_\bullet^2}{2\;r\;v_\star^2}\right)^{-1}\end{aligned} \tag{14}$$

Solution of this equation gives the mach number and velocity in the subsonic part of the wind. We can clearly see from the above equation that for $v_\bullet = 0$, which will mean the AGN is not present, the subsonic part of the CC85 solution is recovered. Also, it is recovered when $\Gamma = 1$ because in that case, although the AGN is present but the outward radiation force cancels the inward gravitational force everywhere.

C : Mach number versus distance diagrams

Integral of the wind equation (5.26) for the winds with NFW gravity and AGN is,

$$\begin{aligned}\ln[\delta_>(\mathcal{M})] = 2\ln[r] \;&+\; 2\ln\Big[2v_{\rm crit}^2 - 2(1-\Gamma)v_\bullet^2 + \Phi_{\rm NFW}(R) \\ &+\; 2(1-\Gamma)v_\bullet^2\frac{R}{r} - \Phi_{\rm NFW}(r)\Big] + const.\end{aligned} \tag{15}$$

where $2v_{\rm crit}^2 = 2v_\star^2 - (1-\Gamma)v_\bullet^2$. The above equation can equivalently be written as,

$$\delta_>(\mathcal{M}) \simeq A\,r^2\left[2v_{\rm crit}^2 - 2(1-\Gamma)v_\bullet^2\left(1-\frac{R}{r}\right) - 2v_s^2\left(1-\frac{\ln(1+r/r_s)}{r/r_s}\right)\right]^2 \tag{16}$$

where the function $\delta_>(\mathcal{M})$ is defined in §5.2.1 of chapter 5. In this equation, A is an arbitrary constant. If we set $A = 1/(2Rv_{\rm crit})^2$, then for $r = R$ and $\mathcal{M} = 1$, both LHS and RHS of the above equation become equal to unity. In Figure C.1 we plot the contours of Mach number versus the radius for three galaxies with a different halo masses. The upper three panels represent the winds without AGN ($v_\bullet = 0$) and the lower three show the effect of the AGN momentum injection. Different contours in each panel correspond to a different value of the constant A. The thick blue contour in each panel represent the case with a critical point at $r = R = 200$ pc and this one is used in the main text to calculate wind properties.

With the inclusion of NFW gravity one encounters a wall type of behaviour at a particular r. Beyond the wall the real and physical solutions are not possible. We would like to mention here that similar situation arises in adiabatic solar wind problem as shown in Panel (c), Figure 2 of Holzer & Axford (1970). The difference is that in the case of galaxy, the energy injection causes a critical point at R=200 pc. From Figure C.1 one can infer the interesting fact that the AGN is not able to drive the gas out of galaxy for intermediate halo masses but it can do so in high mass galaxies.

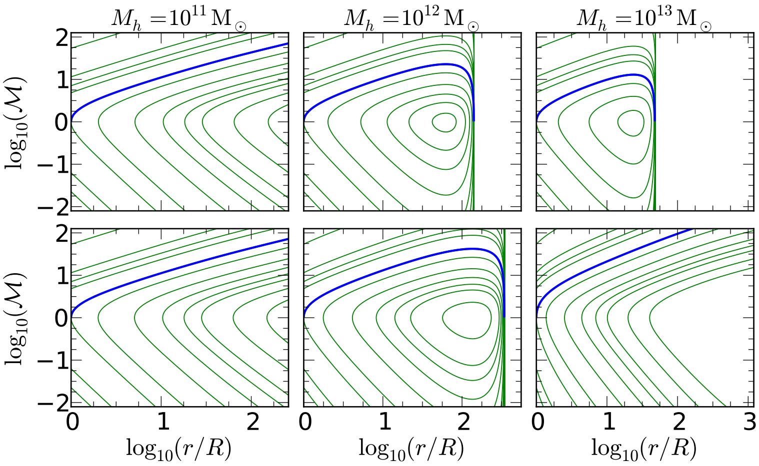

Figure C.1: Mach number versus the radial distance for the winds from a Navarro-Frenk-White dark matter halo. Upper row of plots shows the effect of gravity of dark matter halo only and the lower row takes into account both the gravity due to halo and the effect of AGN. The three plots in each row are for three different halo masses. X-axis in each plot extends upto virial radius corresponding to the halo mass used. The thick blue line represents the solution with a critical point at $R = 200$ pc, which is used in this work. We have taken $v_\star = 180\ \mathrm{km\ s}^{-1}$.

D : Effects of radiative cooling on steady winds

In this section we discuss the effect of radiation loss on the wind properties. In chapter 5, we have neglected the effect of radiative cooling, since it is known that the energy loss due to radiation is too small to affect the dynamics of winds (Grimes et al., 2009). However, the cooling does effect the thermodynamics of the wind and can cause steeper fall in temperature as compared to the case with pure adiabatic expansion. We show this here with a simple case of supersonic escaping wind without gravity for which the wind equation with radiative cooling can be written as,

$$\frac{\mathcal{M}^2-1}{\mathcal{M}^2(\mathcal{M}^2(2/3)+2)}\frac{d\mathcal{M}^2}{dr} = \frac{2}{r}+\frac{(\rho^2/m_p^2)\Lambda(T)}{2\rho v\,\epsilon(r)}(1+\gamma\mathcal{M}^2) \tag{17}$$

where we have used $\rho = \dot{M}/(4\pi v r^2)$, $\gamma = 5/3$ and $c_s^2 = 2\epsilon(r)/(\mathcal{M}^2+3)$. Here $\Lambda(T)$ is the cooling rate in erg cm^3 s^{-1}. We use $\Lambda \propto T^{0.8}$ for the temperature range $10^4 < T < 10^7$ and $\Lambda \propto T^2$ in the temperature range $10^4 < T < 10^5$ (Sutherland & Dopita, 1993). To solve this equation we have to supply $\epsilon(r)$ and $\dot{M}$. The specific enthalpy, $\epsilon(r)$ can be obtained from the integral of energy equation which is given below,

$$\epsilon(r) = \frac{v^2}{2}+\frac{c_s^2}{\gamma-1} = \frac{\dot{E}}{\dot{M}} - \frac{1}{\dot{M}}\int_R^r \frac{\rho^2\Lambda_{\rm cool}}{m_p}(4\pi r^2)dr = \frac{\dot{E}}{\dot{M}} - \frac{\dot{E}_{cool}(r)}{\dot{M}} \tag{18}$$

Considering the fact that total energy extracted by cooling over the entire path is $\sim 10\%$ of the adiabatic losses (Wang, 1995; Grimes et al., 2009) we can neglect $\dot{E}_{cool}$ as compared to $\dot{E}$. Thus we get $\epsilon(r) = \dot{E}/\dot{M} = 2v_\star^2$. Using the $\epsilon(r)$ and a value for $\dot{M}$ in equation (17), we can solve it to obtain Mach number as a function of distance.

In Figure D.1 we plot the sound speed $c_s = [2\epsilon(r)/(\mathcal{M}^2+3)]^{1/2}$ against r, where $\mathcal{M}$ is obtained by solving equation (17). We have solved equation (17) for the quiescent mode ($v_\star = 180$ km s^{-1}) and the starburst mode ($v_\star = 500$ km s^{-1}). We have used $\dot{M} \sim 1$ M$_\odot$/yr and 10 M$_\odot$/yr as two fiducial value of mass loss rate for the quiescent mode and the starburst mode respectively. The sound speed corresponding to quiescent mode is shown by dotted line and that of the starburst mode by a dashed line. We have also shown the corresponding cases without cooling using a dash-dotted and a solid line. By comparing the sound speeds with and without cooling, we find that the cooling causes the temperature to decay more rapidly. Also cooling is effective at smaller distances ($r < 10$ kpc) as the density and temperature are larger there. Wind speed is given by the relation $\epsilon(r) = v^2/2 + c_s^2/(\gamma-1) \sim 2v_\star^2$. The terminal wind speed is obtained by neglecting the sound speed which is known to decrease with distance. As the sound speed go down even more rapidly in case of cooling, therefore the wind speed beyond a distance of 10 kpc does not differ from the case without cooling and is given by, $v_{\rm wind} \approx 2v_\star$. We would like to mention here that qualitatively similar and quantitatively more accurate result has also been obtained by numerically solving the basic fluid equations with cooling for winds from individual star clusters in Silich et al. (2004) and Tenorio-Tagle et al. (2007). Whether the flow undergoing radiative energy losses can achieve a steady state, is also an interesting problem. We refer the reader to Silich et al. (2003) where the time dependent problem on a 2-D grid has been attempted and the result show that the flow can become steady after sufficient amount of time.

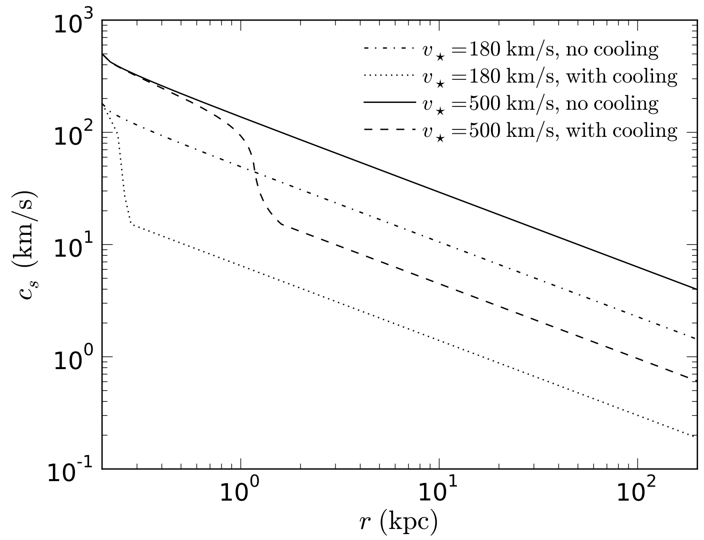

Figure D.1: Sound speed for the wind with cooling is compared with the corresponding case without cooling. The Solid and dash dotted lines represent the case without cooling for quiescent mode and starburst mode respectively. Their counterparts with cooling are shown by dashed and dotted lines.

E : Coupling between dust and gas

The equation for motion of dust grains acted upon by the radiation from AGN can be written as,

$$v_{\rm dr}\frac{dv_{\rm dr}}{dr} = \frac{\pi a^2 Q_{\rm rp} L}{4\pi r^2 c\, m_d} - f_{\rm drag} - f_{\rm grav} \tag{19}$$

The first term on right hand side is the force of radiation per unit mass in which $Q_{\rm rp}$ is the radiation pressure mean efficiency, a is the size and m_d is the mass of the dust grain. $f_{\rm grav}$ is the gravitational force per unit mass and $f_{\rm drag}$ is the drag force per unit mass due to the gas through which the dust grains drift with a velocity $v_{\rm dr}$. This drag force is given by,

$$f_{\rm drag} = \frac{\rho \pi a^2 v^2}{m_d} \tag{20}$$

where ρ and v is the density and velocity of the gas, and a and m_d is the size and mass of dust grain respectively. The drag force is a resistive force for the dust but the same drag is a driving force for the gas. One has to simultaneously solve this equation along with the gas momentum equation to work out the general two phase structure of dusty winds. However many essential features can be captured in a so called ‘single fluid approximation’ where the dust grains attain a terminal drift speed and then the above written dust momentum equation need not be solved (Simis & Woitke, 2004). In that case one can substitute the entire radiation force into the gas momentum equation (Equation 5.2 in chapter 5) because of the exact momentum coupling between dust and gas. The dust grains receive momentum from photons and then pass it on to gas particles via collisions which further distribute it to other gas particles (Gilman, 1972).

The momentum coupling and single fluid approximation can be applied if the dust grains attain a terminal drift speed quickly within a short distance once they start moving. We can now verify the validity of momentum coupling in the present case of a galactic outflow. Assuming a typical density profile $\rho = \rho_o(r_o/r)^2$ and neglecting the gravity in comparison to strong forces of radiation and drag, we can integrate equation (19) to obtain the following solution (see also Gilman 1972),

$$v_{\rm dr}^2(r) = v_{\rm T}^2 \left[1 - \exp\left(-\frac{2\ell}{r_o}(1 - r_o/r)\right)\right] \tag{21}$$

where the terminal drift speed of dust grains is, $v_{\rm T} = [Q_{\rm rp}L/4\pi c\rho_o r_o^2]^{1/2}$ with $l = \rho_o r_o^2 \pi a^2/m_d$ and r_o is the launching radius. How quickly the terminal drift speed is achieved, is decided by the value of the multiplicative factor $2\ell/r_o$ in the exponential. We can estimate ℓ for a typical grain size of 0.1 μm, and a grain mass density of 3 g cm^{-3}. The quantity $\rho_o r_o^2 = \rho_R R^2$, where $R = 200$ pc is the critical point, $\rho_R = 1$ m$_{\rm p}$ cm^{-3} which is a typical value at the critical point in our wind models. Using these values we get $\ell \approx 5$ kpc. If the dust grains are launched at $r_o \sim 10$ pc, we have $2\ell/r_o \sim 10^3$ and even for $r_o = 100$ pc we obtain $2\ell/r_o \sim 10^2$. These large values of $2\ell/r_o$ imply that the grains attain drift speed within a short distance. Once the grains are moving with the constant terminal drift speed ($v_{\rm T}$) the entire radiation force is transferred to the gas via the drag force. Therefore the exact coupling between the dust and the gas is justified. Thus the momentum injection force per unit mass of the gas is simply given by $f(r) = n_d m_d f_{\rm drag}/\rho$. As the dust is moving with a terminal speed, it implies that the drag force is equal to the radiation force. Therefore we can substitute the radiation force in place of $f_{\rm drag}$ to obtain the following expression for force on gas ($f(r)$),

$$f(r) = \frac{n_d Q_{\rm rp}\pi a^2}{\rho}\frac{L}{4\pi r^2 c} = \kappa\frac{L}{4\pi r^2 c} \tag{22}$$

where κ is the opacity for a mixture of dust and gas.

F : Forces due to thin disc

Consider a razor thin disc in r–ϕ plane as illustrated in the Fig. F.1. Now our task is to calculate the force components at any arbitrary point above the disc. Let us consider an annulus of the disc between R' and $R' + dR'$. Area of the element at point P($R', \phi', 0$) is

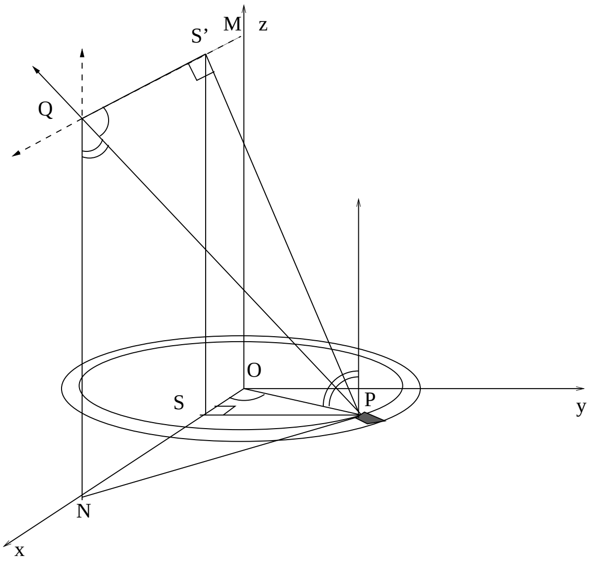

Figure F.1: Schematic diagram for the calculation of gravitational force due to disc in the xy-plane. We consider an annulus in the disc and an element of area around the point P $(R', \phi, 0)$ in this annulus is considered here in order to compute the force at a point Q $(R, 0, z)$ whose azimuthal coordinate $\phi = 0$. The point S $(R' \cos\phi, 0, 0)$ is the foot of the perpendicular drawn from P on the x-axis. The point S' $(R', 0, z)$ is at the intersection of the vertical from S (along z-axis) and the line parallel to x-axis at height z. The angle $\angle SQS' = \cos^{-1}\left[\frac{\mathrm{S'Q}}{\mathrm{PQ}}\right]$, and $\angle PQN = \cos^{-1}\left[\frac{\mathrm{QN}}{\mathrm{PQ}}\right]$.

$R'dR'd\phi'$. Also take a field point Q$(R, 0, z)$ above the disc plane. Azimuthal coordinate of Q is taken to be zero for simplicity as we know that azimuthal force components are zero due to symmetry. Let QN and QM be perpendiculars from Q on the x and the z-axis, respectively. So we can write,

$$\begin{aligned} \mathrm{PN}^2 &= (R - R'\cos\phi')^2 + (R'\sin\phi')^2 \\ \mathrm{PQ}^2 &= \mathrm{PN}^2 + z^2 = R^2 + z^2 + R'^2 - 2RR'\cos\phi' \\ \sin\angle\mathrm{PQN} &= \frac{\mathrm{PN}}{\mathrm{PQ}} \end{aligned} \tag{23}$$

The gravitational force due to the small area element at P is given by

$$d\mathbf{F_g} = \frac{G\,dm\,\mathrm{PQ}}{(\mathrm{PQ})^3}\hat{n}\ ;\ dm = R'dR'd\phi'\Sigma(R') \tag{24}$$

Here $\Sigma(R')$ is the surface density of the disc. Now the z component of this force is

$$dF_{g,z} = |d\mathbf{F_g}|\frac{z}{\mathrm{PQ}} = \frac{zG\Sigma(R')\ R'dR'd\phi'}{[R^2 + z^2 + R'^2 - 2RR'\cos\phi']^{3/2}} \tag{25}$$

To calculate the radial component, let PS be the perpendicular from P on the x-axis. Then, we have sin∠SPN = $\frac{\mathrm{SN}}{\mathrm{PN}} = \frac{R-R'\cos\phi'}{\mathrm{PN}}$. Component of the force along the direction of PN is

$$dF_{g,\mathrm{PN}} = |d\mathbf{F_g}| \sin\angle\mathrm{PQN} = |d\mathbf{F_g}| \frac{\mathrm{SN}}{\mathrm{PN}} \tag{26}$$

So the radial component is

$$dF_{g,R} = dF_{g,\mathrm{PN}} \sin\angle\mathrm{SPN} = |d\mathbf{F_g}| \frac{\mathrm{SN}}{\mathrm{PN}}\frac{\mathrm{PN}}{\mathrm{PQ}} = \frac{(R-R'\cos\phi')\; G\Sigma(R')\; R'dR'd\phi'}{[R^2+z^2+R'^2-2RR'\cos\phi']^{3/2}} \tag{27}$$

G : Cosmic ray driven outflows

Cosmic Rays (CRs) can drive large-scale outflows if the coupling between high energy particles and thermal gas is strong enough (Ipavich, 1975; Breitschwerdt et al., 1991; Zirakashvili et al., 1996). CRs streaming along the magnetic field lines excite Alfvén waves through the 'streaming instability' (Kulsrud & Pearce, 1969). Scattering off this wave field limits the CRs' bulk speed. These waves are then damped, effectively transferring CR energy and momentum to the thermal gas; hence CRs exert a pressure on the thermal gas by means of scattering off Alfvén waves.

Ipavich (1975) studied this process assuming a spherical geometry and assuming that the waves were completely damped away. Later, Breitschwerdt et al. (1991) considered a disc geometry, and calculated the effect of both small and large damping. They found solutions of the outflow equations with realistic ($\sim$ 1 M$_\odot$ yr^{-1}) mass loss rates from Milky Way-type galaxies. Such winds can explain the small gradient in γ-ray emission as a function of galacto-centric radius (Breitschwerdt et al., 2002). Similarly, an outflow from the Milky Way driven by CRs explains the observed synchrotron emission as well as the diffuse soft X-ray emission towards the Galactic bulge region much better than a static atmosphere model (Everett et al., 2010). CR-driven outflows, in which the CR fluid provides an additional source of pressure on thermal gas, may eject substantial amounts of gas from spherically symmetric galaxies with a mass outflow rate per unit SFR of order $0.2-0.5$ for massive galaxies (Samui et al., 2010). Hence, CR pressure in starburst galaxies would provide a negative feedback to star formation and eventually limit the luminosity (Socrates et al., 2008). These general ideas and analytical arguments have been supported by detailed numerical simulations employing an implementation of CR physics in the GADGET code (Jubelgas et al., 2008). In this appendix we work out the dynamics of CR driven winds from galaxies. In the next section we explain the CR streaming and then we present the calculation and our results.

Cosmic ray streaming

CR proton populations have several properties which could help galaxies to launch strong winds. SNe are one of the main energy sources of the ISM and they are believed to convert a significant fraction ($10\% - 60\%$) of their energy into CRs via diffusive shock acceleration in SN remnants (Kang & Jones, 2005; Helder et al., 2009). Also the energy loss times of CRs are longer than the cooling time of thermal gas in ISM, and nearly all the energy lost by the CR population through various mechanisms like particle-particle interactions, expansion, or collective plasma effects (as discussed below) is delivered to the thermal plasma. Therefore, all energy dissipated by the CRs is gained by the thermal plasma, and hence, the CRs act as the perfect mediators to transfer SN energy into the wind regions. Compared to the thermal wind driving process in which a significant fraction of energy is lost via cooling, CRs can energize the wind with a higher efficiency. The mobility of CRs to travel rapidly along already opened magnetic field lines and their ability to open ISM magnetic field lines via the Parker instability make them perfect candidates for driving galactic winds.

Mechanism for transport of CRs along the field lines is called CR streaming, as we explain below. The relativistic speed of the CRs is reduced as they move along the magnetic field lines due to ‘pitch angle scattering’. The scattering isotropizes the CRs pitch angles, and thereby reduces the CR bulk speed. A resonant loop operates in which the scattering CRs excite the Alfvén waves and the Alfvén waves act as mediators which take the energy from CRs and transfer it to the plasma through their damping. As the background field lines are the constituents of the Alfvén waves in the plasma, therefore the scattered CRs should be riding these Alfven waves, hence their effective streaming speed should be of the order of the Alfvén velocity (e.g. Wentzel, 1968; Kulsrud & Pearce, 1969; Kulsrud & Cesarsky, 1971; Kulsrud, 2005). However, if the plasma beta is large or in other words, if the Alfvén velocity is strongly subsonic, then the Alfvén velocity can not be the limiting velocity for CRs. One can understand it as follows. If magnetic fields become weaker and weaker in an otherwise unaltered plasma, the Alfvén velocity would approach zero and any CR streaming, which would be limited to this speed, would vanish. However, weaker magnetic fields imply weaker coupling of the CRs to the thermal plasma and therefore intuitively one would expect a larger, or at least constant transport velocity that is independent of the magnetic field strength in this limit.

Consequently, a number of authors have worked on the problem of CR streaming in high-beta plasmas (e.g. Holman et al., 1979; Achterberg, 1981; Felice & Kulsrud, 2001), and a summary of these works can be found in Enßlin et al. (2011). The consensus among most of these authors seems to be that the limiting velocity is of the order of the sound speed in this situation. It can be several times this speed, or less, depending on details of the pre-existing wave level, thermal and CR energy density, magnetic topology and so forth. Here, we adopt the pragmatic approach of Enßlin et al. (2011) to parametrize our lack of knowledge on the precise dependence of the magnitude of the CR streaming speed $\upsilon_{\rm st}$ on the plasma parameters and assume that it is proportional to the local sound speed $c_{\rm s}$, ($\upsilon_{\rm st} = \lambda\, c_{\rm s}$), with a proportionality constant $\lambda \geq 1$. Here we work with $\lambda = 1$.

Outflow dynamics and mass loading

We consider a steady state situation and assume that CRs first diffuse out to a height above the disc, comparable to the scale height. In spherical symmetry, we can write the constant gas mass flux per unit solid angle, $q = \rho \upsilon r^2$, where ρ is the gas mass density, υ is the gas velocity, and r is the radial distance. The mass density of CRs, $\rho_{\rm cr}$, is fixed by the constant CR flux per unit solid angle in the steady state: $q_{\rm cr} = \rho_{\rm cr} \upsilon_{\rm cr} r^2$, where $\upsilon_{\rm cr} = \upsilon + c_s$ is the CR speed.

We will first calculate the terminal wind speed using the Bernoulli theorem, assuming that there are streamlines along which gas can travel from the disc to a large distance. In the steady state and for spherical symmetry, the energy equation for a compressible fluid is given by

$$\frac{1}{r^2}\frac{\partial}{\partial r}\left[\rho \upsilon r^2 \left(\epsilon + \frac{\upsilon^2}{2} + \frac{P}{\rho}\right)\right] = \upsilon \cdot \mathbf{F} + \nabla . \mathbf{Q}\,, \tag{28}$$

where $\mathbf{F}$ and $\mathbf{Q}$ represent the external force and energy flux respectively, ϵ is the specific internal energy (thermodynamic energy per unit mass), and P is the pressure. Here we have a two-component fluid composed of gas and CRs. Using an adiabatic index of $\gamma = 5/3$ for the gas, and writing $c_{\rm s}^2 = \gamma P/\rho$, we have the following gas energy equation,

$$\frac{q}{r^2}\frac{\partial}{\partial r}\left(\frac{\upsilon^2}{2} + 3\frac{c_{\rm s}^2}{2} + \Phi\right) = \Lambda_{\rm cr-heating}, \tag{29}$$

where Φ is the gravitational potential and $\Lambda_{\rm cr-heating}$ is the heating term due to damping of CR-excited Alfvén waves. We neglect radiative cooling for the tenuous gas in the wind in this analytical treatment. Since $\rho_{\rm cr} \ll \rho$, we can safely neglect the bulk kinetic energy of CRs as well as their gravitational attraction. Thus, we have (using $\epsilon = P_{\rm cr}/3$ as an approximation for ultra-high-energy particles),

$$\frac{q_{\rm cr}}{r^2}\frac{\partial}{\partial r}\left(4\frac{P_{\rm cr}}{\rho_{\rm cr}}\right) = -\Lambda_{\rm cr-heating}. \tag{30}$$

Here, the negative sign of $\Lambda_{\rm cr-heating}$ indicates the loss of CR energy due to wave excitation.

Adding these two equations and integrating, we get the following equation for total energy,

$$q\left(\frac{v^2}{2}+3\frac{c_{\rm s}^2}{2}+\Phi\right)+4q_{\rm cr}\frac{P_{\rm cr}}{\rho_{\rm cr}}=C, \tag{31}$$

where C is a constant. Equating the values at the base and the end of a streamline, we have

$$\frac{v_\infty^2}{2}+\left(3\frac{c_{\rm s,\infty}^2}{2}+\frac{4q_{\rm cr}P_{\rm cr,\infty}}{q\rho_{\rm cr,\infty}}\right)+\Phi_\infty=\frac{v_{\rm b}^2}{2}+3\frac{c_{\rm s,b}^2}{2}+\frac{4q_{\rm cr}P_{\rm cr,b}}{q\rho_{\rm cr,b}}+\Phi_{\rm b}\,. \tag{32}$$

The sum of the terms inside the parenthesis is $3/2$ times the square of the effective combined sound speed of gas and CRs at infinity, and is negligible for an adiabatic flow. We are therefore left with the following expression,

$$v_\infty^2=v_{\rm b}^2+3c_{\rm s,b}^2+\frac{8q_{\rm cr}P_{\rm cr,b}}{q\rho_{\rm cr,b}}-2\,\Delta\Phi\,, \tag{33}$$

where $\Delta\Phi=\Phi_\infty-\Phi_{\rm b}$. We will use the gravitational potential due to a baryonic component and the dark matter halo, given by the Navarro-Frenk-White (NFW) profile (1996). Since $\Phi_\infty=0$, we obtain

$$\Delta\Phi=\frac{GM_{\rm bar}}{r_{\rm b}}+\frac{GM_h}{\ln(1+c)-c/(1+c)}\frac{\ln(1+r_{\rm b}/r_{\rm s})}{r_{\rm b}}. \tag{34}$$

Here, $M_{\rm bar}$ is the total baryonic mass and M_h is the halo mass of a sphere enclosing a mean density that is 200 times the critical density of the universe, $r_{\rm s}$ is the characteristic radius of the NFW profile, in which the density profile is given by $\rho\propto(r/r_{\rm s})^{-1}(1+r/r_{\rm s})^{-2}$. Assuming the initial gas speed $v_{\rm b}\sim c_{\rm s,b}$, the gas sound speed at the base, we have an expression for the wind speed at large distance which depends on the CR parameters and the gas sound speed at the base. The condition for an unbound flow or the existence of the wind is given by,

$$4c_{\rm s,b}^2+\frac{8q_{\rm cr}P_{\rm cr,b}}{q\rho_{\rm cr,b}}>2\Delta\Phi\,. \tag{35}$$

Multiplying equation 33 with the mass density, we arrive at the energy budget of the problem,

$$\varepsilon_{\rm wind}\equiv\frac{\rho v_\infty^2}{2}=\varepsilon_{\rm gain}-\varepsilon_{\rm loss}=2\rho c_{\rm s,b}^2+\frac{4\rho q_{\rm cr}P_{\rm cr,b}}{\rho_{\rm cr,b}q}-\rho\Delta\Phi\,, \tag{36}$$

which essentially states that the kinetic energy of the wind is the difference between the total energy gain and the loss of energy against gravity. In other words, we have,

$$\frac{\varepsilon_{\rm wind}}{\varepsilon_{\rm gain}}=1-\frac{q\Delta\Phi}{2qc_{\rm s,b}^2+\frac{4q_{\rm cr}P_{\rm cr,b}}{\rho_{\rm cr,b}}}\,. \tag{37}$$

Now, using the value of CR mass flux at the base $q_{\mathrm{cr}} = \rho_{\mathrm{cr}} r_{\mathrm{b}}^2 (\upsilon_{\mathrm{b}} + c_{\mathrm{s,b}}) \sim 2\rho_{\mathrm{cr}} c_{\mathrm{s,b}} r_{\mathrm{b}}^2$, we have

$$\upsilon_\infty^2 = 4c_{\mathrm{s,b}}^2 + \frac{16 c_{\mathrm{s,b}} r_{\mathrm{b}}^2 P_{\mathrm{cr,b}}}{q} - 2\Delta\Phi\,, \tag{38}$$

$$\frac{\varepsilon_{\mathrm{wind}}}{\varepsilon_{\mathrm{gain}}} = 1 - \frac{q\Delta\Phi}{2qc_{\mathrm{s,b}}^2 + 8c_{\mathrm{s,b}} r_{\mathrm{b}}^2 P_{\mathrm{cr,b}}}\,. \tag{39}$$

In the next step, we want to assess how the wind speed and mass-loading factor scale with the halo mass. To this end, we have to specify the wind parameters which should reflect realistic ISM values. We use $c_{\mathrm{s,b}} = 10\,\mathrm{km\,s^{-1}}$, corresponding to an ISM temperature of 10^4 K and assume $P_{\mathrm{cr,b}} = 10^{-12}$ erg cm^{-3}. We adopt a mass flux (per unit solid angle) of $q = 0.01/(4\pi)$ M$_\odot$ yr^{-1}.

Observationally the scaling of the base height r_{b} with υ_c, exhibits two regimes separated by a characteristic circular velocity of $\upsilon_{\mathrm{c,\,crit}} \simeq 120\,\mathrm{km\,s^{-1}}$. At $\upsilon_{\mathrm{c}} \lesssim \upsilon_{\mathrm{c,\,crit}}$, the vertical scale height increases roughly as $r_{\mathrm{b}} \propto \upsilon_{\mathrm{c}}$ according to two-dimensional fits of edge-on exponential discs in the K_{s}-band (Dalcanton et al., 2004).* At $\upsilon_{\mathrm{c}} \gtrsim \upsilon_{\mathrm{c,\,crit}}$, the vertical scale height appears to be independent of υ_{c}. This behaviour can be understood theoretically by the following line of arguments. In shallow gravitational potentials, as found in dwarfs, the vertical scale height should scale with the system size. Hence, we assume the base height r_{b} to scale linearly with the disc size R_{d} (which is in turn a function of halo mass, according to the model by Mo et al. 1998). When the gravitational potential of the halo is deep enough, the vertical scale height is set by the effective equation of state of the ISM. For an effective equation of state of $P_{\mathrm{eff}} \propto \rho^2$, the solution to the hydrostatic equation yields a vertical scale height that is independent of surface mass density (see, e.g., Springel, 2000). Hence, the vertical scale height should be set by radiative cooling (which breaks the scale-invariance of gravity seen in smaller systems) in halos heavy enough to support a thin disc, i.e., for $M \gtrsim 10^{11} M_\odot$ corresponding to $\upsilon_{\mathrm{c}} \gtrsim \upsilon_{\mathrm{c,\,crit}}$. This justifies a constant vertical scale height for these large halos. For our main models, we adopt the following simple prescription for the base height, $r_{\mathrm{b}} = 0.5\,R_{\mathrm{d}}$ for $r_{\mathrm{b}} < r_{\mathrm{b,\,max}}$. We note that these considerations are also reflected in simulations by Uhlig et al. (2012), where identical trends are obtained for the dependence of r_{b} on halo mass or υ_c.

In Fig. G.1, we show the wind speed at a large distance as a function of halo mass. This is compared with the rotation speed of the disc implied by the halo mass, adopting the model of Mo et al. (1998). We note that in this model, the disc mass (which we equate with M_{bar}) is a factor ~ 0.05 of the halo mass. In the low-mass regime, the wind speed is approximately proportional to the circular speed (υ_c). The wind speed increases with halo mass up to values,

---

[*] Here we assume that the base height of the wind scales with the vertical scale height of the disc.

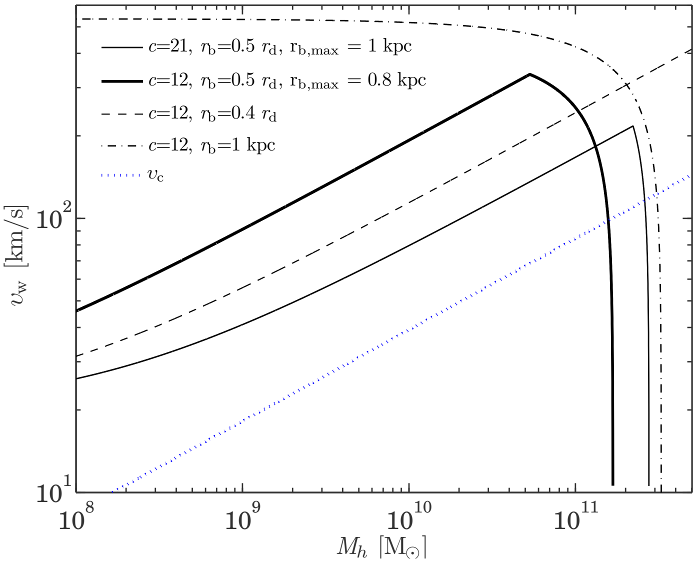

Figure G.1: Wind speed as a function of halo mass (equation (38)) for four models where we vary the input parameters, namely the halo concentration c, the constant of proportionality connecting the base height $r_{\rm b}$ and disc scale height $R_{\rm d}$, and the maximum base height $r_{\rm b,max}$. The blue dotted curve shows the rotation speed as a function of halo mass.

$v_{\rm wind} \equiv v_\infty \sim (200 - 350)$ km s^{-1} , depending on the adopted parameters. At halo masses around $M_h \sim 10^{11}$ M$_\odot$, the CR-driven wind is not any more powerful enough to overcome the increasing potential difference of the halo and ceases. In Fig. G.1, we have also shown two limiting cases. In the first case, shown by dash-dotted line, we adopt a constant $r_{\rm b}$ and find that the wind speed remains approximately constant (500 km s^{-1}) before going to zero at a halo mass of $\sim 10^{11}$ M$_\odot$. In the second case (dashed line) we use the $r_{\rm b}$–$R_{\rm d}$ scaling without the cutoff value $r_{\rm b,\,max}$, which causes the wind speed to be non-zero even for halo masses, $M_h > 10^{11}$ M$_\odot$. We note that, in the model with the high concentration $c = 21$ in Fig. G.1, the wind speed starts to flatten towards lower halo masses. This is because for these small halos the (constant) sound speed starts to dominate over the terms accounting for the loss of energy against gravity and the energy gain due to CR pressure in equation (38).

To estimate the mass loading of the wind, we first estimate the disc surface density $\Sigma_{\rm d} = M_{\rm d}/(\pi R_{\rm d}^2)$, where the disc mass is $M_{\rm d} = M_h/20$. The gas surface density can be written as $\Sigma_{\rm gas} = f_{\rm gas}\Sigma_{\rm d}$, where $f_{\rm gas}$ is the gas mass fraction. To determine the SFR per unit area, $\Sigma_{\rm SFR}$, we use the Schmidt-Kennicutt relation (Kennicutt, 1998),

$$\frac{\Sigma_{\rm SFR}}{\rm M_\odot\ yr^{-1}\ kpc^{-2}} = 2.5 \times 10^{-4} \left(\frac{\Sigma_{\rm gas}}{\rm M_\odot\ yr^{-1}\ pc^{-2}}\right)^{1.4} \tag{40}$$

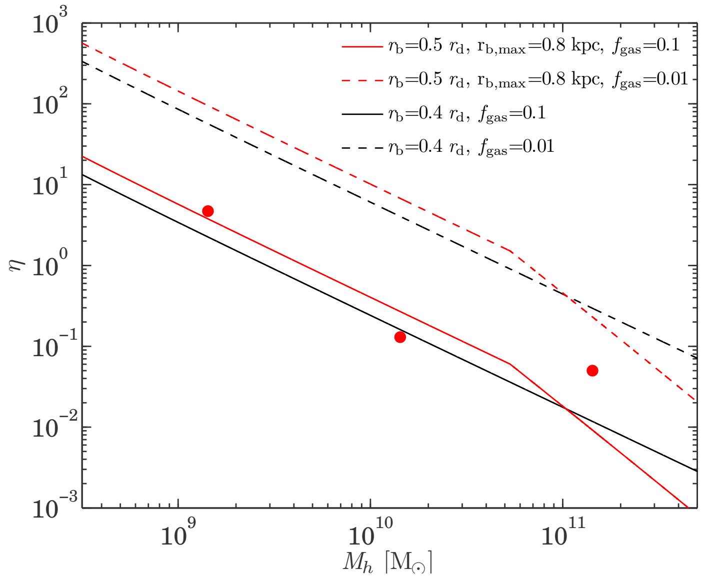

Figure G.2: Mass loading factor $\eta = \dot{M}/\mathrm{SFR}$ (equations (41) and (42)) as a function of halo mass for two values of the gas fractions, $f_{\mathrm{gas}} = 0.1$ and 0.01 (solid and dashed). The two different models both have a halo concentration $c = 12$, as in Fig. G.1. The analytic models compare well with the values of the 'peak mass loading' obtained from the simulations (Uhlig et al., 2012) shown by filled circles.

Hence the SFR of the disc is obtained as

$$\mathrm{SFR} = \pi r_d^2\, \Sigma_{\mathrm{SFR}} = \pi r_d^2 \left[2.5 \times 10^{-4} \left(\frac{f_{\mathrm{gas}} \Sigma_{\mathrm{d}}}{\mathrm{M}_\odot\ \mathrm{yr}^{-1}\ \mathrm{pc}^{-2}} \right)^{1.4} \right] \tag{41}$$

We can estimate the value of the mass flux per unit solid angle, q, for escaping winds, by requiring that $\upsilon_{\mathrm{wind}} = \upsilon_{\mathrm{esc}} = 3\upsilon_c$ in the wind equation (equation (38)) and by inverting it to get $\dot{M} = 4\pi q$ (for a spherical outflow):

$$\dot{M} = \frac{64\pi c_{\mathrm{s,b}} r_{\mathrm{b}}^2 P_{\mathrm{cr,b}}}{9\upsilon_c^2 + 2\Delta\Phi - 4c_{\mathrm{s,b}}^2} \tag{42}$$

We can divide this by the corresponding SFR of equation (41) to obtain the mass loading factor $\eta = \dot{M}/\mathrm{SFR}$. In Fig. G.2, we compare the estimated mass loading factor with the corresponding values obtained in the GADGET simulation (Uhlig et al., 2012). We find that our simple theoretical estimate describes the mass loading observed in simulations reasonably well, which scales as $\eta \propto M_h^{-2/3} \propto \upsilon_c^{-2}$. Hence we conclude that the mass loading in CR-driven winds scales with the halo mass in exactly the way that is needed to explain the low-mass end of luminosity function according to semi-analytical models of galaxy formation (Bower et al., 2012) and phenomenological simulation models (Puchwein & Springel, 2013).

Bibliography

Abazajian, K. N., Adelman-McCarthy, J. K., Agüeros, M. A., et al. 2009, ApJS, 182, 543

Achterberg, A. 1981, A&A, 98, 161

Adelberger, K. L., Steidel, C. C., Shapley, A. E., & Pettini, M. 2003, ApJ, 584, 45

Aguirre, A., Hernquist, L., Schaye, J., et al. 2001, ApJ, 561, 521

Alexander, D. M., Swinbank, A. M., Smail, I., McDermid, R., & Nesvadba, N. P. H. 2010, MNRAS, 402, 2211

Arimoto, N., & Yoshii, Y. 1987, A&A, 173, 23

Baes, M., Buyle, P., Hau, G. K. T., & Dejonghe, H. 2003, MNRAS, 341, L44

Bardeen, J. M., & Berger, B. K. 1978, ApJ, 221, 105

Baugh, C. M. 2006, Reports on Progress in Physics, 69, 3101

Behroozi, P. S., Conroy, C., & Wechsler, R. H. 2010, ApJ, 717, 379

Bergeron, J., & Boissé, P. 1991, A&A, 243, 344

Bergeron, J., Boissé, P., & Ménard, B. 2011, A&A, 525, A51

Bernloehr, K. 1993a, A&A, 268, 25

—. 1993b, A&A, 270, 20

Bertone, S., Stoehr, F., & White, S. D. M. 2005, MNRAS, 359, 1201

Bianchi, S., & Ferrara, A. 2005, MNRAS, 358, 379

Binney, J. 2004, MNRAS, 347, 1093

Binney, J., Gerhard, O., & Silk, J. 2001, MNRAS, 321, 471

Binney, J., & Merrifield, M. 1998, Galactic Astronomy

Binney, J., & Tremaine, S. 2008, Galactic Dynamics: Second Edition (Princeton University Press)

Blanton, M. R., Geha, M., & West, A. A. 2008, ApJ, 682, 861

Bouché, N., Hohensee, W., Vargas, R., et al. 2012, MNRAS, 3207

Bower, R. G., Benson, A. J., & Crain, R. A. 2012, MNRAS, 422, 2816

Bower, R. G., Benson, A. J., Malbon, R., et al. 2006, MNRAS, 370, 645

Breitschwerdt, D., Dogiel, V. A., & Völk, H. J. 2002, A&A, 385, 216

Breitschwerdt, D., McKenzie, J. F., & Völk, H. J. 1991, A&A, 245, 79

Bruzual, G., & Charlot, S. 2003, MNRAS, 344, 1000

Bryan, G. L., & Norman, M. L. 1998, ApJ, 495, 80

Bullock, J. S., Kolatt, T. S., Sigad, Y., et al. 2001, MNRAS, 321, 559

Burbidge, E. M., Burbidge, G. R., & Rubin, V. C. 1964, ApJ, 140, 942

Burke, J. A. 1968, MNRAS, 140, 241

Cattaneo, A., Dekel, A., Devriendt, J., Guiderdoni, B., & Blaizot, J. 2006, MNRAS, 370, 1651

Cen, R., & Bryan, G. L. 2001, ApJ, 546, L81

Cen, R., Nagamine, K., & Ostriker, J. P. 2005, ApJ, 635, 86

Cen, R., & Ostriker, J. P. 1999, ApJ, 519, L109

Chand, H., & Gopal-Krishna. 2012, ApJ, 754, 38

Chattopadhyay, I. 2005, MNRAS, 356, 145

Chattopadhyay, I., Sharma, M., Nath, B. B., & Ryu, D. 2012, MNRAS, 423, 2153

Chen, H.-W., Helsby, J. E., Gauthier, J.-R., et al. 2010, ApJ, 714, 1521

Chevalier, R. A. 1974, ApJ, 188, 501

Chevalier, R. A., & Clegg, A. W. 1985, Nature, 317, 44

Conroy, C., Prada, F., Newman, J. A., et al. 2007, ApJ, 654, 153

Cooper, J. L., Bicknell, G. V., Sutherland, R. S., & Bland-Hawthorn, J. 2008, ApJ, 674, 157

—. 2009, ApJ, 703, 330

Cowie, L. L., & Songaila, A. 1998, Nature, 394, 44

Croton, D. J., Springel, V., White, S. D. M., et al. 2006, MNRAS, 365, 11

Cucchiara, A., Prochaska, J. X., Zhu, G., et al. 2012, arXiv : 1211.6528, arXiv:1211.6528

Dalcanton, J. J., Yoachim, P., & Bernstein, R. A. 2004, ApJ, 608, 189

Dayal, P., Ferrara, A., & Dunlop, J. S. 2013, MNRAS, 430, 2891

Debuhr, J., Quataert, E., & Ma, C.-P. 2012, MNRAS, 420, 2221

Dekel, A., & Silk, J. 1986, ApJ, 303, 39

Dekel, A., & Woo, J. 2003, MNRAS, 344, 1131

Demoulin, M. H., & Burbidge, E. M. 1970, ApJ, 159, 799

Di Matteo, T., Springel, V., & Hernquist, L. 2005, Nature, 433, 604

Diamond-Stanic, A. M., Moustakas, J., Tremonti, C. A., et al. 2012, ApJ, 755, L26

Dickey, J. M., & Lockman, F. J. 1990, ARA&A, 28, 215

Dorodnitsyn, A., Bisnovatyi-Kogan, G. S., & Kallman, T. 2011, ApJ, 741, 29

Draine, B. T. 2003, ARA&A, 41, 241

—. 2011, ApJ, 732, 100

Dubois, Y., & Teyssier, R. 2008, A&A, 477, 79

Dunn, J. P., Bautista, M., Arav, N., et al. 2010, ApJ, 709, 611

Efstathiou, G. 2000, MNRAS, 317, 697

Elvis, M. 2000, ApJ, 545, 63

Enßlin, T., Pfrommer, C., Miniati, F., & Subramanian, K. 2011, A&A, 527, A99

Everett, J. E., & Murray, N. 2007, ApJ, 656, 93

Everett, J. E., Schiller, Q. G., & Zweibel, E. G. 2010, ApJ, 711, 13

Faucher-Giguère, C.-A., & Quataert, E. 2012, MNRAS, 3450

Felice, G. M., & Kulsrud, R. M. 2001, ApJ, 553, 198

Ferrara, A., & Einaudi, G. 1992, ApJ, 395, 475

Ferrara, A., Pettini, M., & Shchekinov, Y. 2000, MNRAS, 319, 539

Ferrarese, L. 2002, ApJ, 578, 90

Feruglio, C., Maiolino, R., Piconcelli, E., et al. 2010, A&A, 518, L155

Flynn, C., Holmberg, J., Portinari, L., Fuchs, B., & Jahreiß, H. 2006, MNRAS, 372, 1149

Fontanot, F., De Lucia, G., Monaco, P., Somerville, R. S., & Santini, P. 2009, MNRAS, 397, 1776

Fragile, P. C., Murray, S. D., & Lin, D. N. C. 2004, ApJ, 617, 1077

Fu, H., & Stockton, A. 2009, ApJ, 690, 953

Fujita, A., Mac Low, M.-M., Ferrara, A., & Meiksin, A. 2004, ApJ, 613, 159

Fujita, A., Martin, C. L., Mac Low, M.-M., New, K. C. B., & Weaver, R. 2009, ApJ, 698, 693

Fukugita, M., Hogan, C. J., & Peebles, P. J. E. 1998, ApJ, 503, 518

Garnett, D. R. 2002, ApJ, 581, 1019

Gebhardt, K., Bender, R., Bower, G., et al. 2000, ApJ, 539, L13

Geha, M., Blanton, M. R., Masjedi, M., & West, A. A. 2006, ApJ, 653, 240

Genzel, R., Tacconi, L. J., Rigopoulou, D., Lutz, D., & Tecza, M. 2001, ApJ, 563, 527

Gilman, R. C. 1972, ApJ, 178, 423

Gilmore, G., Wyse, R. F. G., & Norris, J. E. 2002, ApJ, 574, L39

Governato, F., Brook, C., Mayer, L., et al. 2010, Nature, 463, 203

Granato, G. L., De Zotti, G., Silva, L., Bressan, A., & Danese, L. 2004, ApJ, 600, 580

Greve, A. 2004, A&A, 416, 67

Grimes, J. P., Heckman, T., Aloisi, A., et al. 2009, ApJS, 181, 272

Gültekin, K., Richstone, D. O., Gebhardt, K., et al. 2009, ApJ, 698, 198

Harten, A. 1983, Journal of Computational Physics, 49, 357

Heckman, T. M. 2002, in Astronomical Society of the Pacific Conference Series, Vol. 254, Extragalactic Gas at Low Redshift, ed. J. S. Mulchaey & J. T. Stocke, 292

Heckman, T. M., Armus, L., & Miley, G. K. 1990, ApJS, 74, 833

Heckman, T. M., Lehnert, M. D., & Armus, L. 1993, in Astrophysics and Space Science Library, Vol. 188, The Environment and Evolution of Galaxies, ed. J. M. Shull & H. A. Thronson, 455

Heckman, T. M., Lehnert, M. D., Strickland, D. K., & Armus, L. 2000, ApJS, 129, 493

Helder, E. A., Vink, J., Bassa, C. G., et al. 2009, Science, 325, 719

Holman, G. D., Ionson, J. A., & Scott, J. S. 1979, ApJ, 228, 576

Holzer, T. E., & Axford, W. I. 1970, ARA&A, 8, 31

Hopkins, P. F., Quataert, E., & Murray, N. 2012, MNRAS, 421, 3522

Ipavich, F. M. 1975, ApJ, 196, 107

Johnson, H. E., & Axford, W. I. 1971, ApJ, 165, 381

Joshi, R., Chand, H., & Gopal-Krishna, H. 2013, MNRAS, arXiv:1307.3904

Jubelgas, M., Springel, V., Enßlin, T., & Pfrommer, C. 2008, A&A, 481, 33

Kang, H., & Jones, T. W. 2005, ApJ, 620, 44

Kang, H., Ostriker, J. P., Cen, R., et al. 1994, ApJ, 430, 83

Keeney, B. A., Danforth, C. W., Stocke, J. T., et al. 2006, ApJ, 646, 951

Kennicutt, Jr., R. C. 1998, ARA&A, 36, 189

King, A. 2003, ApJ, 596, L27

—. 2005, ApJ, 635, L121

King, A. R., Zubovas, K., & Power, C. 2011, MNRAS, 415, L6

Komatsu, E., Dunkley, J., Nolta, M. R., et al. 2009, ApJS, 180, 330

Kormendy, J., & Bender, R. 2011, Nature, 469, 377

Kornei, K. A., Shapley, A. E., Martin, C. L., et al. 2012, ArXiv e-prints, arXiv:1205.0812

Kotilainen, J. K., Reunanen, J., Laine, S., & Ryder, S. D. 2001, A&A, 366, 439

Krolik, J. H., & Begelman, M. C. 1988, ApJ, 329, 702

Kulsrud, R., & Pearce, W. P. 1969, ApJ, 156, 445

Kulsrud, R. M. 2005, Plasma physics for astrophysics, ed. Kulsrud, R. M.

Kulsrud, R. M., & Cesarsky, C. J. 1971, Astrophys. Lett., 8, 189

Kurosawa, R., & Proga, D. 2009, ApJ, 693, 1929

Larson, R. B. 1974, MNRAS, 169, 229

Lawther, D., Paarup, T., Schmidt, M., et al. 2012, A&A, 546, A67

Leauthaud, A., Tinker, J., Bundy, K., et al. 2012, ApJ, 744, 159

Lee, H., Skillman, E. D., Cannon, J. M., et al. 2006, ApJ, 647, 970

Lehnert, M. D., & Heckman, T. M. 1996, ApJ, 462, 651

Lehnert, M. D., Heckman, T. M., & Weaver, K. A. 1999, ApJ, 523, 575

Leitherer, C., Schaerer, D., Goldader, J. D., et al. 1999, ApJS, 123, 3

Lequeux, J., Peimbert, M., Rayo, J. F., Serrano, A., & Torres-Peimbert, S. 1979, A&A, 80, 155

Li, A., & Draine, B. T. 2001, ApJ, 554, 778

Lynds, C. R., & Sandage, A. R. 1963, ApJ, 137, 1005

Mac Low, M.-M., & Ferrara, A. 1999, ApJ, 513, 142

Macciò, A. V., Dutton, A. A., van den Bosch, F. C., et al. 2007, MNRAS, 378, 55

Madau, P., Ferrara, A., & Rees, M. J. 2001, ApJ, 555, 92

Mandelbaum, R., Seljak, U., Kauffmann, G., Hirata, C. M., & Brinkmann, J. 2006, MNRAS, 368, 715

Mannucci, F., Cresci, G., Maiolino, R., Marconi, A., & Gnerucci, A. 2010, MNRAS, 408, 2115

Marcolini, A., Strickland, D. K., D’Ercole, A., Heckman, T. M., & Hoopes, C. G. 2005, MNRAS, 362, 626

Martin, C. L. 1998, ApJ, 506, 222

—. 1999, ApJ, 513, 156

—. 2005, ApJ, 621, 227

Mathews, W. G., & Baker, J. C. 1971, ApJ, 170, 241

McClure, R. D., & van den Bergh, S. 1968, AJ, 73, 1008

McKee, C. F., & Ostriker, J. P. 1977, ApJ, 218, 148

McQuillin, R. C., & McLaughlin, D. E. 2012, MNRAS, 423, 2162

Ménard, B., Nestor, D., Turnshek, D., et al. 2008, MNRAS, 385, 1053

Mo, H. J., Mao, S., & White, S. D. M. 1998, MNRAS, 295, 319

Molteni, D., Ryu, D., & Chakrabarti, S. K. 1996, ApJ, 470, 460

Mor, R., & Netzer, H. 2012, MNRAS, 420, 526

More, S., van den Bosch, F. C., Cacciato, M., et al. 2011, MNRAS, 410, 210

Morganti, R., Holt, J., Saripalli, L., Oosterloo, T. A., & Tadhunter, C. N. 2007, A&A, 476, 735

Moster, B. P., Somerville, R. S., Maulbetsch, C., et al. 2010, ApJ, 710, 903

Muñoz-Cuartas, J. C., Macciò, A. V., Gottlöber, S., & Dutton, A. A. 2011, MNRAS, 411, 584

Murray, N., Chiang, J., Grossman, S. A., & Voit, G. M. 1995, ApJ, 451, 498

Murray, N., Ménard, B., & Thompson, T. A. 2011, ApJ, 735, 66

Murray, N., Quataert, E., & Thompson, T. A. 2005, ApJ, 618, 569

Nath, B. B., & Silk, J. 2009, MNRAS, 396, L90

Nath, B. B., & Trentham, N. 1997, MNRAS, 291, 505

Navarro, J. F., Frenk, C. S., & White, S. D. M. 1996, ApJ, 462, 563

Nielsen, N. M., Churchill, C. W., & Kacprzak, G. G. 2012, submitted to ApJ, arXiv:1211.1380

Novak, G. S., Ostriker, J. P., & Ciotti, L. 2012, MNRAS, 427, 2734

Oppenheimer, B. D., & Davé, R. 2006, MNRAS, 373, 1265

Oppenheimer, B. D., & Davé, R. 2008, MNRAS, 387, 577

Parker, E. N. 1965, Space Sci. Rev., 4, 666

Pizagno, J., Prada, F., Weinberg, D. H., et al. 2007, AJ, 134, 945

Pizzella, A., Corsini, E. M., Dalla Bontà, E., et al. 2005, ApJ, 631, 785

Porciani, C., Viel, M., & Lilly, S. J. 2007, ApJ, 659, 218

Press, W. H., & Schechter, P. 1974, ApJ, 187, 425

Prochter, G. E., Prochaska, J. X., & Burles, S. M. 2006a, ApJ, 639, 766

Prochter, G. E., Prochaska, J. X., Chen, H.-W., et al. 2006b, ApJ, 648, L93

Proga, D., Stone, J. M., & Kallman, T. R. 2000, ApJ, 543, 686

Puchwein, E., & Springel, V. 2013, MNRAS, 428, 2966

Risaliti, G., & Elvis, M. 2004, in Astrophysics and Space Science Library, Vol. 308, Supermassive Black Holes in the Distant Universe, ed. A. J. Barger, 187

Risaliti, G., & Elvis, M. 2010, A&A, 516, A89

Rowan-Robinson, M. 2000, MNRAS, 316, 885

Rupke, D. S., Veilleux, S., & Sanders, D. B. 2005a, ApJ, 632, 751

—. 2005b, ApJS, 160, 115

Rupke, D. S. N., & Veilleux, S. 2011, ApJ, 729, L27

Ryu, D., Brown, G. L., Ostriker, J. P., & Loeb, A. 1995, ApJ, 452, 364

Ryu, D., Ostriker, J. P., Kang, H., & Cen, R. 1993, ApJ, 414, 1

Samui, S., Subramanian, K., & Srianand, R. 2008, MNRAS, 385, 783

—. 2010, MNRAS, 402, 2778

Savage, B. D., Sembach, K. R., & Lu, L. 1997, AJ, 113, 2158

Schaye, J., Aguirre, A., Kim, T.-S., et al. 2003, ApJ, 596, 768

Schneider, D. P., Richards, G. T., Hall, P. B., et al. 2010, VizieR Online Data Catalog, 7260, 0

Schneider, R., & Omukai, K. 2010, MNRAS, 402, 429

Schwartz, C. M., & Martin, C. L. 2004, ApJ, 610, 201

Schwartz, C. M., Martin, C. L., Chandar, R., et al. 2006, ApJ, 646, 858

Scoville, N. 2003, Journal of Korean Astronomical Society, 36, 167

Scoville, N., & Norman, C. 1995, ApJ, 451, 510

Seaquist, E. R., & Clark, J. 2001, ApJ, 552, 133

Shankar, F., Lapi, A., Salucci, P., De Zotti, G., & Danese, L. 2006, ApJ, 643, 14

Shapley, A. E., Steidel, C. C., Pettini, M., & Adelberger, K. L. 2003, ApJ, 588, 65

Sharma, M., & Nath, B. B. 2012, ApJ, 750, 55

—. 2013, ApJ, 763, 17

Sharma, M., Nath, B. B., & Shchekinov, Y. 2011, ApJ, 736, L27

Shen, Y., Richards, G. T., Strauss, M. A., et al. 2011, ApJS, 194, 45

Sheth, R. K., & Tormen, G. 2002, MNRAS, 329, 61

Silich, S., Bisnovatyi-Kogan, G., Tenorio-Tagle, G., & Martínez-González, S. 2011, ApJ, 743, 120

Silich, S., Tenorio-Tagle, G., & Muñoz-Tuñón, C. 2003, ApJ, 590, 791

Silich, S., Tenorio-Tagle, G., & Rodríguez-González, A. 2004, ApJ, 610, 226

Silk, J., & Nusser, A. 2010, ApJ, 725, 556

Silk, J., & Rees, M. J. 1998, A&A, 331, L1

Silk, J., Wyse, R. F. G., & Shields, G. A. 1987, ApJ, 322, L59

Simis, Y., & Woitke, P. 2004, in Asymptotic giant branch stars, ed. H. J. Habing & H. Olofsson, Astronomy and Astrophysics Library, Springer, 291

Skilling, J. 1975, MNRAS, 172, 557

Smith, L. J., & Gallagher, J. S. 2001, MNRAS, 326, 1027

Socrates, A., Davis, S. W., & Ramirez-Ruiz, E. 2008, ApJ, 687, 202

Socrates, A., & Sironi, L. 2013, ApJ, 772, L21

Sofue, Y., Reuter, H.-P., Krause, M., Wielebinski, R., & Nakai, N. 1992, ApJ, 395, 126

Somerville, R. S., Hopkins, P. F., Cox, T. J., Robertson, B. E., & Hernquist, L. 2008, MNRAS, 391, 481

Somerville, R. S., & Primack, J. R. 1999, MNRAS, 310, 1087

Somerville, R. S., Moustakas, L. A., Mobasher, B., et al. 2004, ApJ, 600, L135

Songaila, A. 2001, ApJ, 561, L153

Songaila, A., & Cowie, L. L. 1996, AJ, 112, 335

Spitzer, L. 1962, Physics of Fully Ionized Gases

Springel, V. 2000, MNRAS, 312, 859

Springel, V., Di Matteo, T., & Hernquist, L. 2005, ApJ, 620, L79

Springob, C. M., Haynes, M. P., Giovanelli, R., & Kent, B. R. 2005, ApJS, 160, 149

Steidel, C. C., Dickinson, M., & Persson, S. E. 1994, ApJ, 437, L75

Stinson, G. S., Brook, C., Prochaska, J. X., et al. 2012, MNRAS, 3506

Strel'Nitskii, V. S., & Sunyaev, R. A. 1973, Soviet Ast., 16, 579

Strickland, D. K., & Heckman, T. M. 2009, ApJ, 697, 2030

Strickland, D. K., Heckman, T. M., Colbert, E. J. M., Hoopes, C. G., & Weaver, K. A. 2004, ApJ, 606, 829

Strickland, D. K., & Stevens, I. R. 2000, MNRAS, 314, 511

Sturm, E., González-Alfonso, E., Veilleux, S., et al. 2011, ApJ, 733, L16

Suchkov, A. A., Balsara, D. S., Heckman, T. M., & Leitherer, C. 1994, ApJ, 430, 511

Sudilovsky, V., Savaglio, S., Vreeswijk, P., et al. 2007, ApJ, 669, 741

Sutherland, R. S., & Dopita, M. A. 1993, ApJS, 88, 253

Taylor, C. L., Walter, F., & Yun, M. S. 2001, ApJ, 562, L43

Tejos, N., Lopez, S., Prochaska, J. X., et al. 2009, ApJ, 706, 1309

Tenorio-Tagle, G., Wünsch, R., Silich, S., & Palouš, J. 2007, ApJ, 658, 1196

Tielens, A. G. G. M., McKee, C. F., Seab, C. G., & Hollenbach, D. J. 1994, ApJ, 431, 321

Tomisaka, K., & Bregman, J. N. 1993, PASJ, 45, 513

Tomisaka, K., & Ikeuchi, S. 1988, ApJ, 330, 695

Tremaine, S., Gebhardt, K., Bender, R., et al. 2002, ApJ, 574, 740

Tremonti, C. A., Moustakas, J., & Diamond-Stanic, A. M. 2007, ApJ, 663, L77

Tremonti, C. A., Heckman, T. M., Kauffmann, G., et al. 2004, ApJ, 613, 898

Trump, J. R., Hall, P. B., Reichard, T. A., et al. 2006, ApJS, 165, 1

Tumlinson, J., Thom, C., Werk, J. K., et al. 2011, Science, 334, 948

Uhlig, M., Pfrommer, C., Sharma, M., et al. 2012, MNRAS, 423, 2374

van de Voort, F., & Schaye, J. 2012, MNRAS, 423, 2991

Vázquez, G. A., & Leitherer, C. 2005, ApJ, 621, 695

Veilleux, S., Cecil, G., & Bland-Hawthorn, J. 2005, ARA&A, 43, 769

Veilleux, S., Rupke, D. S. N., & Swaters, R. 2009, ApJ, 700, L149

Vergani, S. D., Petitjean, P., Ledoux, C., et al. 2009, A&A, 503, 771

Villar-Martín, M., Humphrey, A., Delgado, R. G., Colina, L., & Arribas, S. 2011, MNRAS, 418, 2032

Volonteri, M., & Stark, D. P. 2011, MNRAS, 417, 2085

Walter, F., Taylor, C. L., Hüttemeister, S., Scoville, N., & McIntyre, V. 2001, AJ, 121, 727

Wang, B. 1995, ApJ, 444, 590

Weiner, B. J., Coil, A. L., Prochaska, J. X., et al. 2009, ApJ, 692, 187

Wentzel, D. G. 1968, ApJ, 152, 987

Westmoquette, M. S., Clements, D. L., Bendo, G. J., & Khan, S. A. 2012, MNRAS, 424, 416

Westmoquette, M. S., Smith, L. J., Gallagher, III, J. S., et al. 2009, ApJ, 696, 192

Wünsch, R., Silich, S., Palouš, J., Tenorio-Tagle, G., & Muñoz-Tuñón, C. 2011, ApJ, 740, 75

Wyithe, J. S. B., & Loeb, A. 2003, ApJ, 595, 614

Zhang, D., & Thompson, T. A. 2012, MNRAS, 424, 1170

Zhu, G., & Ménard, B. 2013, ApJ, 770, 130

Zirakashvili, V. N., Breitschwerdt, D., Ptuskin, V. S., & Voelk, H. J. 1996, A&A, 311, 113

List of Publications

“Dust-driven Wind from Disc Galaxies”
Sharma, M., Nath, B. B. & Shchekinov, Y. 2011, ApJ[†], 736, L27

“The Roles of Radiation and Ram Pressure in Driving Galactic Winds”
Sharma, M. & Nath, B. B. 2012, ApJ, 750, 55

“Supernovae and AGN Driven Galactic Outflows”
Sharma, M. & Nath, B. B. 2013, ApJ, 763, 17

“Signature of Outflows in Strong Mg II Absorbers in Quasar Sightlines”
Sharma, M., Nath, B. B. & Chand, H. 2013, MNRAS[‡], 431, L93

“Simulation of Radiation-driven Winds from Disc Galaxies”
Chattopadhyay, I., **Sharma, M.**, Nath, B. B. & Ryu, D. 2012, MNRAS, 423, 2153

“Galactic winds Driven by Cosmic Ray Streaming”
Uhlig, M., Pfrommer, C., **Sharma, M.**, Nath, B. B., Enßlin, T. A. & Springel, V. 2012, MNRAS, 423, 2374

[†] ApJ : Astrophysical Journal

[‡] MNRAS : Monthly Notices of Royal Astronomical Society